Nonlinear optical properties of metal-dielectric stacks in their epsilon-near-zero regime

Sisira Suresh

A thesis submitted to the Faculty of Graduate and Postdoctoral Studies
in partial fulfilment of the requirements for the MSc degree in Physics

Under the supervision of
Robert W. Boyd

Department of Physics
Faculty of Science
University of Ottawa
Canada

©Sisira Suresh, Ottawa, Canada, 2020

Abstract

In recent years, significant attention has been given to a class of materials referred to as epsilon-near-zero (ENZ) materials which possess a vanishing dielectric permittivity. This ENZ condition occurs naturally in metals, polar dielectrics, doped semiconductors, etc. However, the wavelength range of the ENZ behaviour is dictated by intrinsic material properties and is not necessarily convenient for all applications. The ENZ condition may also be artificially achieved using metamaterials composed of sub-wavelength-scale constituent materials. In this work, we designed and fabricated a sub-wavelength periodic stack using silver (Ag) and silica (SiO_2) capable of placing the ENZ wavelength anywhere within the entire visible spectrum by adjusting the respective dimensions of the constituent metal and dielectric. We characterize the nonlinearity of this sample using the Z-scan technique and observed a pronounced enhancement of nonlinear response at the ENZ region. The observed value of the nonlinear refractive index n_2 of our metal-dielectric multilayer sample is 1.74 cm^2/GW, which is 10^7 times larger than that of the n_2 of fused silica and 20 times larger than that of the n_2 of bulk silver. We also find that the nonlinear absorption coefficient β is given by -2.43 $\times 10^5$ cm/GW. The ability to obtain strong nonlinearities at designated optical frequencies makes these metamaterials a flexible platform for the nonlinear applications in the visible spectral range. The results of this work confirm that the enhancement of nonlinear optical properties in the ENZ regime can be generalized to a broader class of materials.

Contents

1 Introduction **1**
- 1.1 Background . . . 1
  - 1.1.1 Epsilon-near-zero condition . . . 1
  - 1.1.2 The ENZ medium . . . 3
  - 1.1.3 Metamaterials as ENZ media and their applications . . . 4
- 1.2 Structure of the thesis . . . 6

2 Theory **7**
- 2.1 Linear optical properties of metal-dielectric stacks . . . 7
  - 2.1.1 Optical properties of dielectric materials . . . 7
  - 2.1.2 Optical properties of metals . . . 9
  - 2.1.3 Background study of materials to use as a plasmonics device platform . . . 10
  - 2.1.4 Optical properties of metal-dielectric composites . . . 11
  - 2.1.5 Refractive index and dielectric tensor of the composite medium . . . 13
- 2.2 The effective medium theory . . . 14
  - 2.2.1 Effective parallel permittivity . . . 15
  - 2.2.2 Effective perpendicular permittivity . . . 16
- 2.3 The retrieval theory . . . 19
- 2.4 Nonlinear optical properties of metal-dielectric stack . . . 22
  - 2.4.1 Nonlinear Optics - A brief Introduction . . . 22
  - 2.4.2 Nonlinear Refraction . . . 23
  - 2.4.3 Multiphoton absorption . . . 24

3 Modeling and Simulation **26**
- 3.1 Retrieval of the material parameters using transfer matrix method simulations . 26
- 3.2 Design of the sample . . . 27
- 3.3 Anisotropic behaviour of the metal-dielectric stack . . . 30
- 3.4 Transmission and reflection simulations . . . 31

4 Optical characterization of metal-dielectric composites **34**
- 4.1 Fabrication of metal-dielectric multilayer stacks . . . 34
- 4.2 Linear characterization . . . 34
  - 4.2.1 Spectroscopic ellipsometry . . . 35
  - 4.2.2 Transmittance and reflectance . . . 36
- 4.3 Nonlinear characterization: Z-scan technique . . . 36
  - 4.3.1 An overview of the technique . . . 36
  - 4.3.2 Z-scan theory . . . 39

5 Experiment and methods **44**
5.1 Linear measurements 44
5.1.1 Ellipsometric measurements 44
5.1.2 Determination of permittivity of the metal-dielectric stack from transmission measurements 46
5.2 Nonlinear measurements 47
5.2.1 Experimental setup 47
5.2.2 Beam profile 48
5.2.3 Calibration of the Z-scan experimental setup 52

6 Measurements and interpretations of the linear and nonlinear optical response of the Ag-SiO_2 multilayer stack **55**
6.1 Transmission measurements of the Ag-SiO_2 multilayer stack 55
6.2 Nonlinear optical properties of the Ag-SiO_2 multilayer stack 57

7 Conclusion and Future work **66**
7.1 Conclusion 66
7.2 Scope for future work 66

8 Appendix **68**
8.1 Direct inversion method 68
8.2 Automation of the setup 68
8.3 Matlab code for permittivity calculation 70

Acknowledgments

"Coming together is a beginning
Keeping together is a process
Working together is a success" - Henry Ford

It is a genuine pleasure to express my deep sense of thanks and gratitude to my supervisor Prof. Robert Boyd for the continuous support throughout my Master's degree. His patience, motivation, above all his unconditional helping mentality enabled me to a very great extent to accomplish this task. I am indebted for his guidance on this research topic and life in general. The Boyd group indubitably provides its students with a very friendly atmosphere that makes us feel like we are a family. I have gained invaluable experiences being a member of this group.

I want to give a special thanks to our post-doc and my mentor Dr. Orad Reshef for tirelessly helping me with a ton of patience throughout this journey. I also cannot thank him enough for what he has done in teaching me from simple silly things to write complex simulation codes.

I would like to thank my colleague M. Zahirul Alam for giving me scholarly advice and for helping me with the experimental part of my work. I am very grateful to him for solving all the mysteries I had in the lab and the timely help.

Next, I would like to thank our lab manager Dr. Jeremy Upham for his unconditional help and support all the time since I joined the group. He had spent a lot of time in helping me to write abstracts, to make posters, fabricating my sample, etc.

I would also like to thank my fellow labmate Mohammad Karimi who was also involved in the progress of this research. Moreover, I would like to acknowledge all of my friends Justin, Sam, Jeremy, Kaustub, Kashif, Daniel, Ryan, Sijyl, Saad, Boris, Akbar, Aldo, Tuhin, etc for making the lab such a fun place to work.

I also take this opportunity to acknowledge the financial support of the Canada Excellence Research Chairs (CERC) program.

Certainly, none of this would have been possible without the love and support of my family. My deepest appreciation for their patience and understanding.

Most importantly, I would like to thank my wonderful husband Aneesh to whom this thesis is dedicated. His motivation and endless love and encouragement helped me most to complete this thesis. Thanks for believing in me and wanted the best for me.

Chapter 1

Introduction

Efficient nonlinear optical interactions are necessary for many applications in the field of modern photonics. Recently, great emphasis has been given to the greatly enhanced nonlinear optical responses observed in optical materials with dielectric permittivities that vanish at particular wavelengths. These classes of materials are known as epsilon-near-zero (ENZ) materials. In this work, we use a strongly anisotropic nonlinear metamaterial composed of alternating silver and silica layers of subwavelength thickness that acts as an effective ENZ medium. Metamaterials are unique in their ability to control the confinement and propagation of light. The purpose of this thesis is to show, through theory, simulations and experiments, that a metal-dielectric multilayer stack in its ENZ regime shows enhanced nonlinear properties. In this chapter, we give an introduction to epsilon-near-zero media and review the main applications of these materials.

1.1 Background

In this section, we provide the reader with a general understanding by establishing some definitions about the epsilon-near-zero medium. We survey the work that has been performed on various epsilon-near-zero materials and related plasmonic materials in observations of interesting nonlinear phenomena and we summarize their practical implementations.

1.1.1 Epsilon-near-zero condition

Metals are known to possess a fast, extremely large, nonlinear optical response. In particular, the third-order susceptibility of the noble metals can be as much as 10^6 times larger than that of fused silica, with relaxation times in the subpicosecond range [1]. However, metals are not often used as potential candidates for nonlinear applications due to their large attenuation constant, that make samples that are even tens of nanometers thick essentially non-transmitting for optical light. Dielectrics can have a minimal loss, but generally a much weaker nonlinear response. In order to effectively access the nonlinear properties of metals, a promising approach is to use a composite structure with metals and dielectrics in a specific geometry. Many studies have been done in metal-dielectric composite materials [2, 3, 4]. These studies have considered the effective medium composites either in Maxwell Garnett or Bruggeman geometry. An alternative approach is a layered metal-dielectric geometry. This composite structure geometry enables us to modify the propagation of light through the medium by enhancing the transmission. By redirecting the reflected light from the surface towards the forward direction, multiple Bragg reflections can be achieved [5]. This can enhance the transmission of light through the sample even when the total

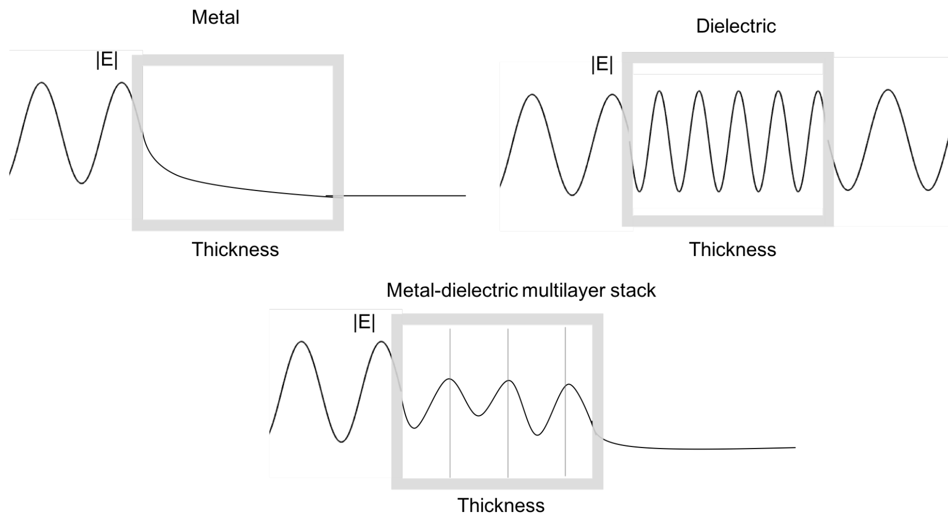

Figure 1.1: Schematic diagram of the electric field distribution through a metal, dielectric and metal-dielectric multilayer stack.

metal thickness in the composite is greater than the conventional skin depth [6]. The modification of the electric field through a metal-dielectric multilayer stack is schematically shown in Fig 1.1. Studies show that the intrinsic nonlinearity of the bulk metals can be enhanced using layered metal-dielectric composite structures [6, 7]. The nonlinear change in the transmission was found to be enhanced by an order of magnitude compared to the bulk metal. Thus, the metal-dielectric composite structures are manifested as potential candidates for various nonlinear applications. However, this is not the only way to enhance the nonlinearity in composite structures. An alternative approach can be explained based on the linear refractive index of the medium. The nonlinear refractive index is related to the linear refractive index of the medium as [11],

$$n_2 = \frac{3}{4 n_0 n_0' \epsilon_0 c} \chi^{(3)}, \tag{1.1}$$

where n_0 is the linear index (complex), n_0' is the real part of index, $\chi^{(3)}$ is the third-order susceptibility and ϵ_0 is the vacuum permittivity. As we can see from the equation, the linear index n_0 is in the denominator. Thus, the intensity-dependent refractive index is a nonlinear process of great practical importance that could be enhanced in the ENZ materials. An enhancement in n_2 when $\epsilon = 0$ is schematically shown in Fig 1.2.

Now, if we examine the expression for refractive index of a medium, we can see that n is related to ϵ and μ by the relation,

$$n_0 = \sqrt{\epsilon \mu}, \tag{1.2}$$

where ϵ is the relative permittivity and μ is the relative permeability of the medium. There are three ways to obtain a zero-index medium, either by tuning ϵ to zero or by tuning μ to zero or by tuning both ϵ and μ to zero. In this work, we are assuming $\mu = 1$ (non-magnetic material), therefore we are discussing only $\epsilon = 0$ cases. These class of materials that exhibit vanishing dielectric permittivity in a particular wavelength range is known as epsilon-near-zero (ENZ) materials [8].

In this section, we will present a literature survey of the works that have been performed in the ENZ materials and the observation of various nonlinear phenomena. The ENZ materials

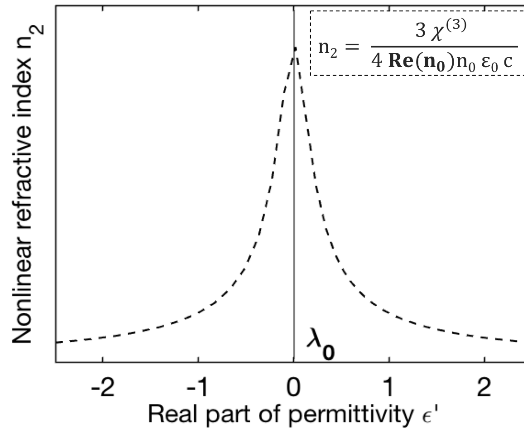

Figure 1.2: Schematic diagram showing the enhancement of n_2 in an ENZ medium.

have exhibited enhanced nonlinear optical properties, with large ultrafast nonlinear refractive indices reported recently in doped semiconducting oxides such as tin-doped indium oxide [9], aluminum-doped zinc oxide [10], etc.

The refractive index of a non-magnetic material ($\mu = 1$) can be defined as the square root of its permittivity, $\mathrm{n} = \sqrt{\epsilon}$. When the real part of ϵ tends to zero, the real and imaginary part of n becomes equal and given by

$$\mathrm{n} = \mathrm{n}' = \sqrt{\frac{|\epsilon''|}{2}}. \tag{1.3}$$

The imaginary part of the permittivity $\epsilon^{''}$ plays a significant role in many materials. This is often referred to as the loss factor, associated with damping losses in the material.. For example, for ITO, the wavelength at which permittivity crosses zero is 1240 nm, and the corresponding $\epsilon^{''} = 0.3$ [9]. This small value of imaginary part of permittivity yields a small real part of the refractive index of 0.4. The nonlinear refractive index can be expressed as

1.1.2 The ENZ medium

In nature, materials with near-zero permittivity are readily available as electron gases, noble metals, doped semiconductors, polar dielectrics, etc. For metals, the classical model used to describe the dielectric constant is the Drude model, which assumes a gas of free carriers. For dielectrics, the model used to describe the dielectric constant is the Lorentz model [12, 13]. At the plasma frequency, the permittivity of metals crosses zero. This frequency is the resonance frequency of the free electron gas around the equilibrium state. For common metals, it is located in deep UV. In homogeneous materials such as doped semiconducting oxides, the ENZ condition occurs in the IR region. For instance, in some tin-doped indium oxide films, it has been observed at wavelengths such as 1240 nm [9], while in aluminium-doped zinc oxide films it has been observed at 1300 nm [14]. The dielectric function of these materials is described by a Drude-type dispersion or sometimes combined models such as the Drude-Lorentz model depending on the constituents [15]. The ENZ wavelength dictated by these bulk materials is not widely tunable over the spectral range. For this reason, these ENZ materials are limited for specific applications alone. Also, due to their large optical losses, metals are largely non-transmitting for optical radiation and hence are not candidate materials for producing large nonlinear optical

interactions. Unlike metals, optical losses of dielectrics are very low, however, their nonlinear response is very small.

1.1.3 Metamaterials as ENZ media and their applications

ENZ materials may also be fabricated as metamaterials composed of constituent materials of subwavelength dimensions. Since the plasma frequency of the metals is in the ultraviolet region, a material with an ENZ region at visible or near-infrared frequencies can be synthesized by embedding these metals in a dielectric host medium [16].

Recently, metamaterials have become an area of intense research due to their ability to realize optical properties that do not occur in natural materials [17]. The advent of the ENZ metamaterials created the opportunity to create anomalous electromagnetic features at microwave and optical frequencies. The wavelength of radiation inside the ENZ medium is extremely large and this allows the light wave to pass through any arbitrary shaped ENZ medium with zero reflection losses at the bends or junctions. This suggests that the electromagnetic wave inside the ENZ metamaterials can be used to squeeze and tunnel energy through narrow arbitrary shaped channels. Generally, coupling energy from an input parallel plate waveguide to an output parallel plate waveguide using an intermediate channel with an arbitrary shape or a narrow cross-section is not possible due to the large reflection from the edges of this intermediate channel, even if, the channel is filled with the same dielectric as the waveguides. But filling the channel with an ENZ material results in the perfect coupling between two waveguides. This phenomenon is referred to as "super-coupling" effect [18]. This is shown in Fig 1.3 (a). There is always a huge impedance mismatch between the ENZ material and the regular material in the waveguides and this can act as a barrier in the coupling. However, it turns out that if at least one of the physical dimensions of the ENZ material channel is small, the wave can tunnel through the narrow channel easily.

Another important property that is associated with the ENZ condition is the near-zero phase variation of an electromagnetic wave inside the ENZ metamaterials over a physically long distance. In particular such important property suggests that the wavefronts in ENZ materials are parallel to the interfaces. Thus, by controlling the shape of the interfaces of an ENZ material, it is possible to tailor the phase radiation pattern of the outgoing radiation. For instance, an incoming planar wavefront can be transformed into a convergent cylindrical wavefront and vice-versa [19]. This is depicted in Fig 1.3 (b). In addition to these amazing applications, another potential application of the ENZ materials is the design of zero-index media (ZIM), where the values of both ϵ and μ are near-zero at the frequency of interest. These materials may have applications in the realization of delay lines, in increasing the directivity of an antenna, in transforming curved wavefronts into planar ones (as described above), and in enhancing the efficiency of some waveguides with abrupt junctions or bends [20]. A ZIM can be realized using metamaterials that consist of resonant non-magnetic inclusions embedded in an ENZ host medium. These inclusions can be designed in such a way that both the effective permittivity and permeability of the composite structure are simultaneously zero [21].

Achieving invisibility or electromagnetic transparency has been the subject of extensive studies in the physics and engineering communities for decades. This has been realized using metamaterial covers with negative or low-permittivity and/or low-permeability materials. Optimal design of these lossless metamaterial covers operating near their plasma resonance may diminish the total scattering cross-section, making these objects nearly invisible or transparent to an outside viewer [22]. Invisible cloaking is another potential application of the ENZ metamaterials which make use of the negative polarizability feature [23].

Another exciting property of ENZ materials is that it can greatly enhance optical nonlinearities [9, 24]. An example is shown in Fig 1.3 (c). In this example of tin-doped indium oxide (ITO)

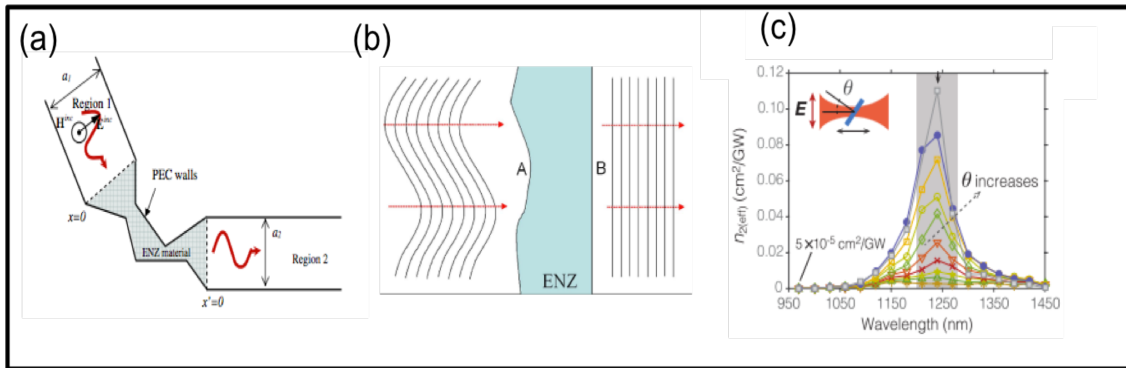

Figure 1.3: Applications of ENZ materials. (a) Super coupling [18]. (b) Tailoring of the radiation pattern [19]. (c) Enhanced nonlinearity [9].

films, an enhancement in nonlinear refractive index is observed in its ENZ wavelength,1240 nm. The exceptional transmission properties of an ENZ ultra-narrow channels are used to boost Kerr nonlinearities. Works have been reported using metamaterials based on plasmonic gratings loaded with nonlinear optical materials to realize an effective ENZ metamaterial in the visible range with large nonlinear optical properties [25]. Such a nonlinear ENZ metamaterial slab may be obtained by carving narrow rectangular apertures loaded with nonlinear optical materials into a silver screen. The working principle is based on the ENZ super coupling transmission within each rectangular slit. This results in a strong and uniform field enhancement inside the nonlinear ENZ slits, which can efficiently boost nonlinear effects compared with conventional resonances. Enhanced nonlinearity is also observed in Au-based plasmonic nanorod metamaterials at their ENZ regime [26]. They observed that the Kerr-type nonlinearity is not limited by the nonlinear properties of the constituents in the metamaterial. The highest third-order nonlinear response has been observed near the ENZ regime. The ENZ behaviour can also be realized by utilizing metal-coated waveguides at the cutoff frequency [27], silver or gold nanowires array embedded in an alumina matrix [28, 29], and the metal-dielectric multilayer structures [30, 31]. There are many ways we can realize an ENZ medium in a metamaterial. Fig 1.4 (a) [16], Fig 1.4 (b) [29] and Fig 1.4 (c) [32] are certain ways of achieving this. Many studies have been done in metal-dielectric layered metamaterials in the homogenized regime. Experimental realization of this kind of metamaterials at the visible wavelengths have been achieved in different metal-dielectric combinations [33, 34, 35].

The novelty we are presenting in this work is, apart from enhancing the transmission and nonlinear response of an otherwise lossy metal, we consider how a carefully designed subwavelength structure could shift the ENZ wavelength from the UV range of a bulk metal into the visible spectrum so that it can serve as a potential candidate for nonlinear applications in the visible spectral range. Also, we will show here how we can change the ENZ condition by tailoring the dimensions of the subwavelength metal and dielectric composites in the stack. This ability to obtain strong nonlinearities at designated optical frequencies makes these metamaterials a flexible platform for the nonlinear applications in the visible spectral range.

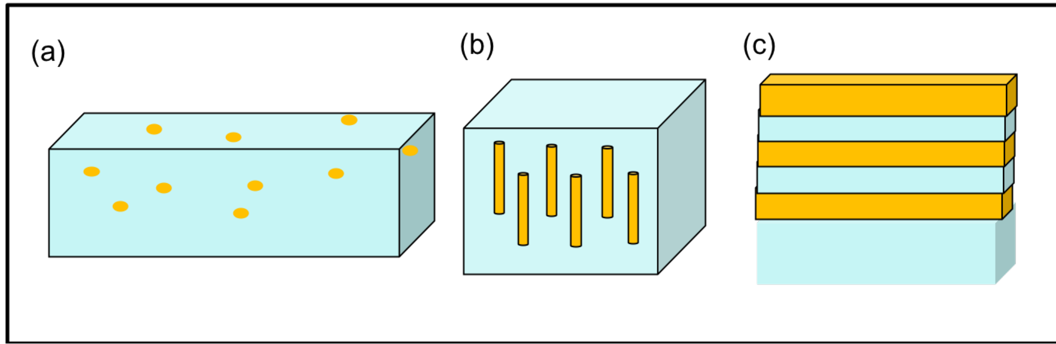

Figure 1.4: Metamaterials as ENZ media. (a) Metal inclusions in a dielectric host. (b) Metal nanorods in a dielectric host. (c) Metal-dielectric multilayer stacks.

1.2 Structure of the thesis

Including the current chapter, Chapter 1, where we present the introduction, this thesis consists of eight chapters. Chapter 2 of the thesis describes the theory of the metal-dielectric multilayer composites. This covers effective medium theory and the linear and nonlinear properties of the sample in detail. Here, we derived the linear effective permittivity function of the sample. This chapter also covers the retrieval theory which we used to make the simulation codes for retrieving the material parameters of the multilayer sample.
In Chapter 3, we outlined the simulation procedures to extract the linear optical properties of the sample such as anisotropy, transmission, reflection etc. We also present the detailed design of the sample based on these simulation results.
Chapter 4 deals with the theory of experimental techniques we used in both linear and nonlinear regime to characterize the optical properties of the sample. The working principle of the characterization tools is explained in details. This Chapter also explains the fabrication procedures for making the subwavelength sample based on the simulation results.
The experiment and methods we adopted in this work are briefly explained in chapter 5. In particular, we describe the experimental setup, methods of data collection, analysis of data, etc. Chapter 6 summarizes the experimental results and the linear and nonlinear characterization of our metal-dielectric multilayer sample. Following that, the conclusions and future work are given in Chapter 7.
Finally, in the Appendix, we show the Labview code we used for the automation of the experiment setup, the Matlab code for the retrieval of permittivity of the metal-dielectric multilayer stack and the direct inversion method we tried in order to extract the permittivity of the sample using ellipsometry parameters.

Chapter 2

Theory

In this chapter, we examine some of the optical properties of the metal-dielectric multilayer stacks and their constituent materials. Following that, we briefly describe the theory behind the effects that will be seen in the simulation and experimental results.

2.1 Linear optical properties of metal-dielectric stacks

Composite optical materials are an important class of materials that exhibit a variety of interesting linear and nonlinear optical properties. They can display properties which are different from that of their constituent materials [36, 37]. In this work, we show such a composite material consisting of subwavelength alternating layers of metal and dielectric arranged in a periodic fashion. First, we explain the basic linear properties of the constituents (metal and dielectric) in the composite and later the properties of the metal-dielectric composite.

2.1.1 Optical properties of dielectric materials

A dielectric material is characterized by a wide energy bandgap, usually larger than 5 eV. As a result, a relatively high energy is necessary to excite a valance band electron into the conduction band. Dielectric materials are poor conductors of electricity; however, they can support an electrostatic field to a great extent with minimum loss of energy as heat [38]. The interaction of light waves inside a dielectric medium can be analyzed using Maxwell's equations. Consider the propagation of an electromagnetic wave through a uniform dielectric medium of dielectric constant ϵ. The dipole moment per unit volume, or polarization P, induced in the medium by the electric field E is given by

$$P = \epsilon_0(\epsilon - 1)E \tag{2.1}$$

Consider a medium with no free charges, so that

$$\rho = 0, \tag{2.2}$$

and no free currents, so that

$$J = 0. \tag{2.3}$$

We also assume that the medium is nonmagnetic, so that

$$B = \mu_0 H. \tag{2.4}$$

Then Maxwell's equations become,

$$\nabla \cdot D = 0, \tag{2.5}$$

$$\nabla \cdot B = 0, \tag{2.6}$$

$$\nabla \times E = -\frac{\partial B}{\partial t}, \tag{2.7}$$

$$\nabla \times H = \frac{\partial D}{\partial t}. \tag{2.8}$$

For non-magnetic materials μ is taken to be unity and this condition simplifies our description of optical materials, especially dielectric materials by assigning a refractive index of the medium,

$$n = \sqrt{\epsilon}. \tag{2.9}$$

Even though all optical materials are dispersive in a strict sense, we omit the argument ω in all permittivity and refractive index expressions to make the equations concise. Thus, electromagnetic waves propagate through dielectric medium travel slower than in vacuum by a factor of n. The dielectric function of such a material is described by the Lorentz model given by [39]

$$\epsilon = 1 + \frac{\omega_1^2}{\omega_0^2 - \omega^2 - i\gamma\omega}, \tag{2.10}$$

where ω_1 and γ are related to the density and damping of bound electrons and ω_0 is the oscillation frequency.

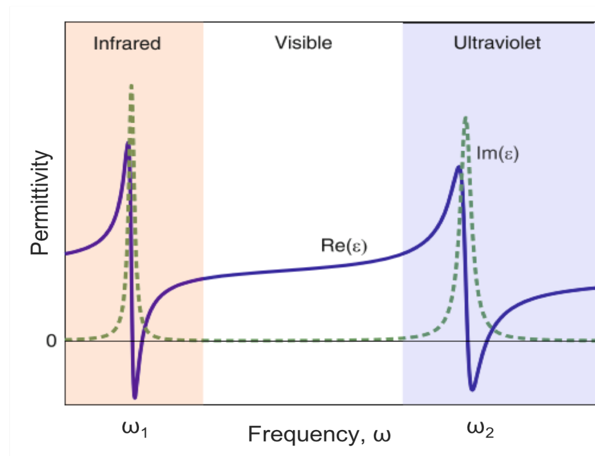

Figure 2.1: The dielectric function of a typical dielectric material with two resonances. ω_1 represents the lattice resonance and ω_2 represents the electron transition resonance [39].

The dielectric function of a typical dielectric material is shown in Fig 2.1. In this example, two resonances are included in the oscillator formula, one in the mid-IR (ω_1) region due to the phonon resonance and other in the UV region (ω_2) due to the electron transition resonance. The function has a Lorentz line shape at each resonance. The resonances at ω_1 and ω_2 cause a large

change in the real part of ϵ. Also, this resonance is associated with a peak in the imaginary part of ϵ which represents the loss. As we can see from the figure, between the two resonance frequencies, the imaginary part is negligible . This makes it obvious why quartz, alumina and similar dielectrics are transparent in the visible spectral range [39].

2.1.2 Optical properties of metals

Metals are known for their high reflectivity and low transmission at optical frequencies. The energy band diagram of metals suggests that there is no gap between the empty energy levels and the occupied ones. As a result, the photon energy from any electromagnetic radiation is enough to excite an electron from a valence band to a conduction band. Similar to the study of dielectric materials in the previous subsection, the light-matter interactions inside metals can be explained by the frequency-dependent permittivity of the metals. There are free electrons inside metals without any restoring force or spring constant. The electromagnetic wave interaction inside the metals is dictated by the collective motion of these free electrons. Therefore, the resonance frequency from the Lorentz model is zero. The classical model used to describe the dielectric function of a metals is the Drude model given by [39]

$$\epsilon = 1 - \frac{\omega_p^2}{\omega^2 + i\Gamma\omega}, \tag{2.11}$$

where Γ is the damping constant, which represents the electron collision rate, and ω_p is the plasma frequency, expressed as,

$$\omega_p = \sqrt{\frac{Ne^2}{m\epsilon_0}} \tag{2.12}$$

with N - density per unit volume of the free carriers,
ϵ_0 - permittivity of the free space,
m - mass of the electron,
$\omega = \frac{2\pi E}{h}$, where E is the photon energy.

The plasma frequency is the natural resonant frequency of a free electron gas around an equilibrium state. For most metals, ω_p is in the deep UV region of the spectrum.
For $\omega < \omega_p$ - the metal is highly absorbing and reflecting, and the refractive index is complex.
For $\omega > \omega_p$- the metal is transparent, and the refractive index is real (k=0).

The Drude model is based on the assumption that all electrons inside the metal are free. It considers only those electrons in the outer orbitals such as 4s, 5s, 6s, etc. However, we have to take into account the contribution from the bound electron charges as well, such as interband transitions, especially for higher frequencies. The interband contribution of bound charges ϵ_{ib} can be explained using the standard Lorentz model. Therefore, the overall dielectric function of metals has both the Drude model (free electrons) and the Lorentz model (bound electrons) contributions, expressed as,

$$\epsilon = \epsilon_{ib} + 1 - \frac{\omega_p^2}{\omega^2 + i\Gamma\omega}. \tag{2.13}$$

The permittivity plot of silver as a function of wavelength is shown in Fig 2.2 [39]. It is clear from the figure that at optical frequencies the real part of the permittivity of metals is negative, unlike the dielectrics which have a positive real permittivity. The negative permittivity of metals at optical frequencies is a result of out-of-phase oscillation of the free electrons with respect to the driving electric field in metals. As a result, most of the incident photons will get reflected

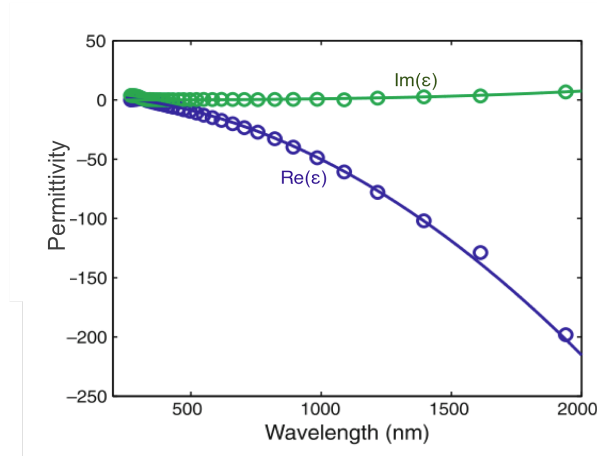

Figure 2.2: Dielectric function of a metal (silver) [39]

at the interface. This behaviour can be illustrated using the refractive index of the metal. The relation between the refractive index and the permittivity is given by

$$\epsilon' = n'^2 - n''^2, \qquad (2.14)$$
$$\epsilon'' = 2n'n'',$$

where n' and ϵ' represents the real part and n'' and ϵ'' represents the imaginary part. Writing in terms of the real and imaginary part of refractive index, equation (2.14) becomes,

$$n'^2 = \frac{1}{2}(\epsilon' + \sqrt{\epsilon'^2 + \epsilon''^2}), \qquad (2.15)$$
$$n''^2 = \frac{1}{2}(-\epsilon' + \sqrt{\epsilon'^2 + \epsilon''^2}).$$

From equation (2.13), along with equation (2.15), we can obtain the complex refractive index of metals. At optical frequencies, the refractive index has a prominent imaginary part while the real part of the index is only slightly larger than zero. This large n'' of metals suggests their lossy nature, which typically reduces the skin depth of metals in the range of tens of nanometer at optical frequencies. The term skin depth in metals is defined as the distance below the surface of the metal where the current density has reduced to $1/e$ of its surface value [40].

2.1.3 Background study of materials to use as a plasmonics device platform

Metals are known for their extremely large nonlinear response [1]. Generally, the skin depth of most of the metals are in the range of tens of nanometer and the thickness of the metal is assumed to be several times the skin depth. The range of skin depth in metals explains why they cannot transmit when the thickness is greater than approximately 50 nm. One way to access the optical nonlinearity of metals is to use a metal-dielectric composite medium [5, 7]. Such metamaterials are significantly thicker than the total thickness of metals present in the sample. This overall thickness of the metamaterial therefore provides much longer effective interaction

length for light with the large nonlinear response of metals compared to the bulk metal at these thicknesses [41].

When choosing a material to create a metamaterial for nonlinear applications, it is usually best to pick the one with the least amount of ohmic loss, and therefore the smallest dampening rate. Comparing the losses of noble metals like silver, gold and copper, we can see that, silver is the best in this regard [42] (damping rate of silver is 0.02 eV, gold is 0.07 eV, copper is 0.07 eV and aluminium is 0.13 eV). Apart from this, another important aspect we have to consider is the interband transition onset. We have to make sure to select a metal whose onset of interband transition is higher than that of the energy of plasmons so that it can support plasmons of desired energy without inducing interband transitions. By looking at the spectral range of the naturally existing ENZ media, none possess an ENZ condition in the visible spectral range. Plasmons that are induced by visible light will have energies ranging from 1.8 eV to 3.1 eV. The onset of interband transitions suggests that silver can support plasmons that span the entire visible spectrum, while gold and copper cannot. The onset of interband transition of silver is 3.9 eV, gold is 2.3 eV, copper is 2. eV and aluminium is 1.41 eV. Based on these data, silver is the obvious choice for nonlinear applications in the visible spectral region, since it has the lowest ohmic loss and a high onset of interband transitions. For applications in the near-infrared spectral region, gold or copper is generally used, but gold is usually preferred over copper since it does not oxidize and is, therefore, more stable. If one wanted to make a device in the ultraviolet regime, aluminium would be the best choice, since it has a higher onset of interband transitions. Other materials do have lower losses than silver and gold, such as sodium and potassium; however, these materials are quite unstable and would therefore not be easy to use in fabricating plasmonic devices. This is the reason why most of the plasmonic devices are made of silver or gold.

2.1.4 Optical properties of metal-dielectric composites

Metals are used for important optical applications because of their large and fast nonlinear response. But the large loss in metals excludes them from applications involving many nonlinear optical interactions. On the other hand, dielectric materials are known to have a minimum loss, but their nonlinear response is very small. In order to effectively access the nonlinear properties of metals, a promising approach is to use a multilayer metal-dielectric structure. Such a metamaterial in which the metal is the dominant nonlinear material can have much larger intensity-dependent changes in the complex amplitude of the transmitted beam than a bulk sample containing the same thickness of metal [5].

In metal-dielectric composites, components are either arranged in a disordered fashion or a periodic fashion, and the overall optical properties of the composite can be remarkably different from those of its constituent materials. The boundary conditions for composite structures are complicated, unlike homogeneous structures, which makes it practically difficult to determine the electromagnetic response by solving Maxwell's equations. However, under certain circumstances, this situation can be treated more simply. The plausible solution for this problem is to treat the composite structure as an effective medium. If the inhomogeneity scale of the composite medium is of subwavelength dimensions, the electrodynamic scattering by the metal or dielectric constituents in the composite will be overshadowed by the effective response of the combined system. Thus, the effective dielectric permittivity of the metal-dielectric composite can be evaluated from the dielectric permittivity of the discrete constituents in the composite as well as their respective fill fractions. Such approaches are called the effective medium approaches.

Maxwell-Garnett theory [43] and the Bruggeman effective medium theory [44] are two popular effective medium approaches. Both the methods are based on averaging the field over a unit-cell. These two methods are distinguished from one another based on the topology of the composite

and the properties of the constituents in the mixture. In composites with Maxwell-Garnett geometry, the inclusion particles embedded in the host material are dilute and have well-defined spherical shapes as shown in Fig 2.3 a. Whereas, in composites with Bruggeman geometry, the inclusions and host play symmetric roles making it difficult to distinguish which is the host and which is the inclusion. This is depicted in Fig 2.3 b. For a metal-dielectric composite, we can visualize the metal as the inclusion and the dielectric as the host. The effective medium expressions for a metal-dielectric composite with a Maxwell-Garnett geometry and a Bruggeman geometry are given in equations (2.16) and (2.17), respectively. These generalized effective medium approximations are the most commonly used method for approximating the effective permittivity of the composite medium. In Maxwell-Garnett geometry, the effective permittivity is expressed as,

$$\epsilon = \epsilon_h \frac{1 + 2f\frac{\epsilon_1 - \epsilon_h}{\epsilon_1 + 2\epsilon_h}}{1 - f\frac{\epsilon_1 - \epsilon_h}{\epsilon_1 + 2\epsilon_h}}, \tag{2.16}$$

where ϵ_1 is the permittivity of the inclusion, ϵ_h is the permittivity of the host, and f is the volume filling fraction of the inclusion.

In Bruggemen geometry, let us consider two spherical particles with permittivities ϵ_1 and ϵ_2 dispersed in a host matrix with a dielectric constant of ϵ_h. The volume filling factors of the two inclusions are f_1 and f_2, respectively. Since each constituent in the composite is regarded as the inclusion, the host medium is composite itself. Therefore, $\epsilon = \epsilon_h$.

$$f_1 \frac{\epsilon_1 - \epsilon}{\epsilon_1 + 2\epsilon} + f_2 \frac{\epsilon_2 - \epsilon}{\epsilon_2 + 2\epsilon} = 0 \tag{2.17}$$

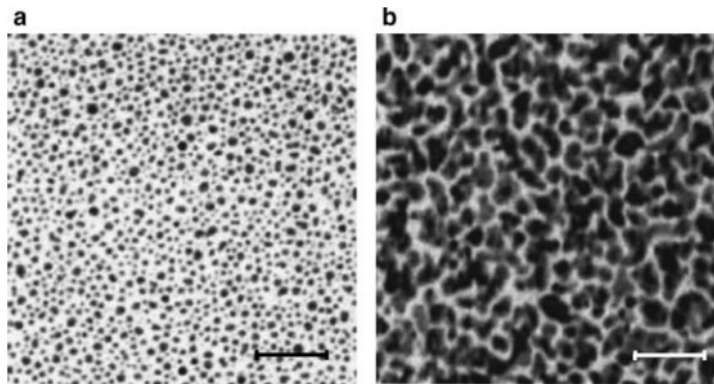

Figure 2.3: TEM images of typical metal-dielectric composites with (a) the Maxwell-Garnett geometry and (b) the Bruggeman geometry. Metals are depicted as dark areas and dielectrics as bright areas. Scale bar is 200 nm [39].

Another well known example of effective medium geometry is multilayer metal-dielectric stacks. When sub-wavelength metallic and dielectric layers are periodically stacked, the coupling of the electromagnetic field at each metal-dielectric plasmonic interface gives rise to a collective response [35]. Each such layer in the multilayer stack can be described by a homogeneous and isotropic permittivity parameter.

2.1.5 Refractive index and dielectric tensor of the composite medium

When the thickness of constituent layers in the metal-dielectric composite is sufficiently thin, far below the operating wavelength, we can treat the system as an effective medium. Such a system can give rise to extreme anisotropy in a uniaxial permittivity tensor [45].
In general, the constitutive relations connecting the electric displacement D and electric field can be written as:

$$\begin{bmatrix} D_x \\ D_y \\ D_z \end{bmatrix} = \begin{bmatrix} \epsilon_{\rm xx} & \epsilon_{\rm xy} & \epsilon_{\rm xz} \\ \epsilon_{\rm yx} & \epsilon_{\rm yy} & \epsilon_{\rm yz} \\ \epsilon_{\rm zx} & \epsilon_{\rm zy} & \epsilon_{\rm zz} \end{bmatrix} \begin{bmatrix} E_x \\ E_y \\ E_z \end{bmatrix} \tag{2.18}$$

where x,y,z represents the arbitrary orthogonal coordinate system. Upon diagonalization, the permittivity tensor assumes the form,

$$\left[\epsilon\right] = \begin{bmatrix} \epsilon_{\rm xx} & 0 & 0 \\ 0 & \epsilon_{\rm yy} & 0 \\ 0 & 0 & \epsilon_{\rm zz} \end{bmatrix} \tag{2.19}$$

in a Cartesian frame of reference oriented along the principal axes of the crystal.

In a biaxial medium, all three dielectric constants are different, $\epsilon_{\rm xx} \neq \epsilon_{\rm yy} \neq \epsilon_{\rm zz}$.

In a uniaxial medium, two of the three are same, $\epsilon_{\rm xx} = \epsilon_{\rm yy} \neq \epsilon_{\rm zz}$.

And in an isotropic medium, all the three are same, $\epsilon_{\rm xx} = \epsilon_{\rm yy} = \epsilon_{\rm zz}$.

For light polarized along one of the principal axes, the refractive index in an anisotropic medium is defined as, $\epsilon_i = n_i^2$. The index seen by the electromagnetic wave interacting with the medium depends on the polarization state. For example, light entering a calcite crystal splits into two rays, each traveling in a different direction with different speed, because the refractive index for one wave is greater than the refractive index for the other wave. The wave with ordinary refractive index is polarized perpendicular to the optical axis and the other with extraordinary refractive index is polarized parallel to the optical axis [35].

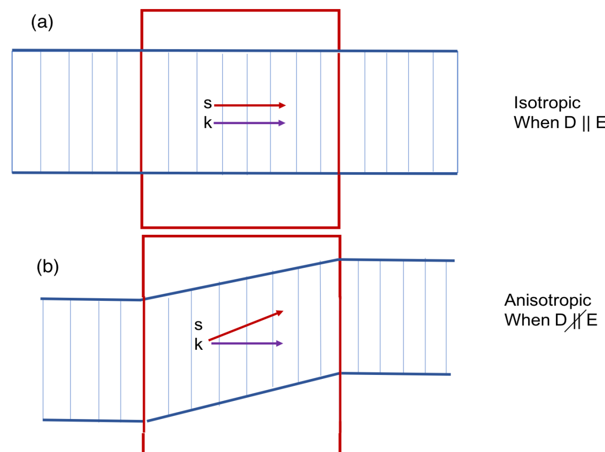

Figure 2.4: Schematic illustration of wave propagation in an isotropic (a) and an anisotropic (b) medium. S is the Poynting vector and k is the wave vector.

The permittivity tensor determines a surface called the index ellipsoid, which illustrates the orientation and relative magnitude of refractive indices in crystals. It is given by

$$\frac{x^2}{\epsilon_{\text{xx}}} + \frac{y^2}{\epsilon_{\text{yy}}} + \frac{z^2}{\epsilon_{\text{zz}}} = 1 \tag{2.20}$$

In terms of refractive index it is expressed as,

$$\frac{x^2}{{n_x}^2} + \frac{y^2}{{n_y}^2} + \frac{z^2}{{n_z}^2} = 1. \tag{2.21}$$

In biaxial media, n_x, n_y, n_z are different.

In uniaxial media, $n_x = n_y = n_o$, where n_o is the ordinary refractive index and $n_z = n_e$, where n_e is the extraordinary refractive index. The observation of two refractive indices for a general orientation of the wavefront is known as birefringence.

For a positive uniaxial medium, $n_e > n_o$ and for a negative uniaxial medium $n_e < n_o$. In the isotropic case, the wave vector k and the Poynting vector S are collinear as shown in Fig 2.4 (a), and in an anisotropic crystal the wave vector surface becomes ellipsoidal and, as a result, the angle between k and S is non-zero. This scenario is shown in Fig 2.4 (b). If we draw a plane through origin which is orthogonal to k-vector, the curve of intersection of this plane with the ellipsoid is an ellipse, as shown in Fig 2.5. The semi-axes of the ellipse thus obtained will be proportional to the reciprocals of the phase velocities and their directions represent the vibrations in D. The ordinary vibration direction lies in the circular section of the index ellipsoid with refractive index n_0. Light travelling along the optic axis experiences just this refractive index, the ordinary refractive index. The extraordinary vibration direction lies in the plane of the wavefront and perpendicular to the ordinary vibration direction, and has refractive index n_e. Optically isotropic materials (e.g. cubic crystals) have one refractive index, with a spherical indicatrix.

Consider a cross-section of the index ellipsoid containing the optic axis and the extraordinary vibration direction. The refractive index in extraordinary axis will depend on angle. For arbitrary values of θ, it is given by [46]

$$\frac{1}{{n_e(\theta)}^2} = \frac{\sin^2(\theta)}{{n_e}^2} + \frac{\cos^2(\theta)}{{n_o}^2(\theta)}. \tag{2.22}$$

2.2 The effective medium theory

In this subsection, we will look at deriving the effective medium permittivity of a metal-dielectric multilayer stack with uniaxial permittivity. A generalized Maxwell-Garnett approach is used to derive the analytical expressions for the effective permittivity in parallel ($\epsilon_{\parallel}$) and perpendicular ($\epsilon_{\perp}$) directions with respect to the layers of the composite material [47, 48]. Here we are taking the limit of infinite number of metal-dielectric interfaces within the stack for homogenization purposes. Fig 2.6 represents the schematic of a multilayer metal-dielectric stack. The individual metal and dielectric layers possess a dielectric permittivity of ϵ_m and ϵ_d, respectively.
The fill fraction of the metal component in the multilayer stack is given by

$$\rho = \frac{d_m}{d_m + d_d}, \tag{2.23}$$

where d_m is the thickness of each metal layers in the stack and d_d is the thickness of each dielectric layers in the stack.

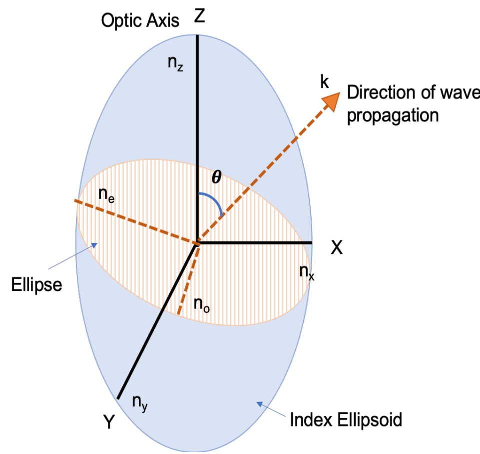

Figure 2.5: Index ellipsoid for a typical anisotropic crystal. n_0 is the ordinary refractive index and n_e is the extraordinary refractive index.

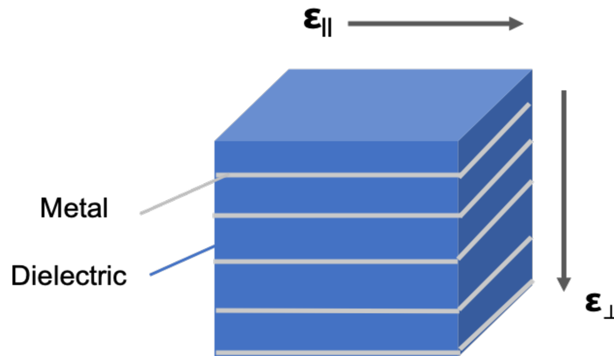

Figure 2.6: Schematic diagram of a metal-dielectric multilayer stack

2.2.1 Effective parallel permittivity

We can write the relation between displacement field (D) and electric field (E) through the following equation,

$$D = \epsilon_{\text{eff}} E, \tag{2.24}$$

where ϵ_{eff} is the effective permittivity of the medium. D and E are the fields averaged over a region larger than the scale of inhomogeneity. When we go from one medium to another, the boundary condition states that the tangential component of the electric field must be continuous across the interface. This implies that, if the electric field is polarized along the plane of the layers, the field is spatially uniform within the stack. Therefore, we can say that the electric field in the metallic layers ($E_m^{||}$) and the dielectric layers ($E_d^{||}$) are equal and we can equate this to the volume-averaged electric field ($E^{||}$) in the parallel direction. This is expressed as,

$$E_m^{||} = E_d^{||} = E^{||}. \tag{2.25}$$

Then the overall electric field in the parallel direction can be written by weighing the fields with the corresponding volume fraction ρ as,

$$\rho E^{\parallel} + (1-\rho)E^{\parallel} = E^{\parallel} \tag{2.26}$$

And, the overall displacement field in the parallel direction can be obtained by averaging the displacement field from the metal and the dielectric. The displacement field components for metals ($D_m^{\parallel}$) and dielectrics ($D_d^{\parallel}$) will not be equal for the perpendicular polarization. This is expressed as,

$$D^{\parallel} = \rho D_m^{\parallel} + (1-\rho)D_d^{\parallel}. \tag{2.27}$$

Written in terms of the electric field, equation (2.27) becomes,

$$\epsilon_{\text{eff}}^{\parallel} E^{\parallel} = \rho\epsilon_m E^{\parallel} + (1-\rho)\epsilon_d E^{\parallel}. \tag{2.28}$$

After cancelling the $E^{\parallel}$ on both sides of the equation, equation (2.28) reduces to,

$$\epsilon_{\text{eff}}^{\parallel} = \rho\epsilon_m + (1-\rho)\epsilon_d. \tag{2.29}$$

Equation (2.29) represents the effective parallel permittivity relation approximated using the effective medium theory. So, when the electric field is polarized in the plane of the layers (or E $\perp$ z), the optical constants of the composite turns out to be the simple average of constituent materials in the composite.

2.2.2 Effective perpendicular permittivity

Here we will look at deriving the effective medium permittivities when the electric field is polarized perpendicular to the plane of layers (E $\parallel$ z). In this case, the electric field becomes non-uniformly distributed between the two components in the composite and the normal component of the electric displacement vector at an interface must be continuous. Therefore, the displacement field in the metallic layers ($D_m^{\perp}$) and the dielectric layers ($D_d^{\perp}$) are equal and we can equate this to the volume-averaged displacement field ($D^{\perp}$) in the parallel direction. This is expressed as,

$$D_m^{\perp} = D_d^{\perp} = D^{\perp}, \tag{2.30}$$

Thus the overall displacement field becomes,

$$\rho D^{\perp} + (1-\rho)D^{\perp} = D^{\perp}. \tag{2.31}$$

The electric field components for metals ($E_m^{\perp}$) and dielectrics ($E_d^{\perp}$) will not be equal for perpendicular polarization. So, we can express the total electric field as the superposition of constituent fields of the components.

$$E^{\perp} = \rho E_m^{\perp} + (1-\rho)E_d^{\perp}. \tag{2.32}$$

Written in terms of the displacement field, equation (2.32) becomes,

$$\frac{D^{\perp}}{\epsilon_{\text{eff}}^{\perp}} = \rho\frac{D^{\perp}}{\epsilon_m^{\perp}} + (1-\rho)\frac{D^{\perp}}{\epsilon_d^{\perp}}. \tag{2.33}$$

The common displacement term $D^{\perp}$ cancels from both sides of equation (2.33). The resultant equation will be,

$$\frac{1}{\epsilon_{\text{eff}}^{\perp}} = \frac{\rho}{\epsilon_m^{\perp}} + \frac{(1-\rho)}{\epsilon_d^{\perp}}. \tag{2.34}$$

Equation (2.34) represents the effective perpendicular permittivity relation approximated using the effective medium theory.

For an arbitrary angle of incidence, we need to modify the effective medium theory equations as a function of angle. Fig 2.7 shows the propagation of a ray through a metal-dielectric stack as described by the effective-medium theory. The angles θ_{in} and θ_{out} are equal and the angle inside the effective medium is given by Snell's law [37].

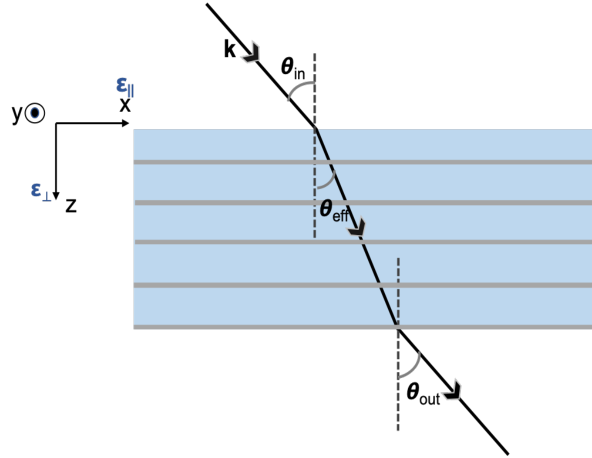

Figure 2.7: Propagation of light through a metal-dielectric multilayer stack as described by the effective medium theory.

Taking into account the angle of incidence θ_{in} and the effective refraction angle θ_{eff} into the stack, equations (2.27) and (2.31) can be associated with the wave parameters for parallel and perpendicular polarization [37, 49]. Assuming a monochromatic plane wave propagating through a non-magnetic uniaxial medium, the dispersion equations are given by [37]

for TE wave:

$$\frac{k_x^2 + k_y^2}{\epsilon_\perp} + \frac{k_z^2}{\epsilon_\perp} = k_0^2, \tag{2.35}$$

and for TM wave:

$$\frac{k_x^2 + k_y^2}{\epsilon_{||}} + \frac{k_z^2}{\epsilon_\perp} = k_0^2, \tag{2.36}$$

where $k_0 = \omega/c$. Fig 2.7 represents the propagation in xz plane. Here k_x is the in-plane wave vector and k_z is the normal component of the wave vector in the multilayer stack. For TE polarization, $k_x = k_0 \sin\theta_{in} = k_0 n_\perp \sin\theta_{\text{eff}}$ and $k_z = k_0 n_\perp \cos\theta_{\text{eff}}$, for TM polarization, $k_x = k_0 n_{||} \sin\theta_{\text{eff}}$ and $k_z = k_0 n_\perp \cos\theta_{\text{eff}}$. Thus, equations (2.35) and (2.36) are associated with the wave parameters by the relation,

for TE polarization,

$$\frac{1}{\epsilon^\perp(\theta_{\text{in}})} = \frac{\sin^2\theta_{\text{eff}}}{\epsilon^\perp} + \frac{\cos^2\theta_{\text{eff}}}{\epsilon^\perp}, \tag{2.37}$$

and for TM polarization,

$$\frac{1}{\epsilon^{||}(\theta_{\text{in}})} = \frac{\sin^2\theta_{\text{eff}}}{\epsilon^{||}} + \frac{\cos^2\theta_{\text{eff}}}{\epsilon^\perp}, \tag{2.38}$$

where θ_{eff} is the effective refraction angle into the slab as shown in Fig 2.7.

Fig 2.8 depicts the permittivity of a multilayer stack consisting of alternating layers of silver (Ag) and silica (SiO_2) with a metallic fill fraction of 0.197 at normal incidence theoretically calculated using equations (2.29) and (2.34). The data for Ag is taken from Johnson and Christy [50] and SiO_2 from Palik [51]. Only the real parts are shown here and the imaginary parts can be calculated similarly. Here the permittivity crosses zero at around 480 nm and this happens when the real part of ϵ_m is equal to $-(1-\rho)\epsilon_\mathrm{d}/\rho$. At the same time, the perpendicular permittivity displays a resonance at a particular wavelength when the real part of ϵ_m is equal to $-\rho\epsilon_\mathrm{d}/(1-\rho)$. The strength of this resonance is limited by the damping constant Γ, given in equation (2.13). For wavelengths above the ENZ point and sufficiently far away from the resonance, the multilayer stack will exhibit hyperbolic behaviour meaning that one of the principal components of their electric effective tensor has the opposite sign to the other two principal components [52]. In these spectral regions above ENZ , the real part of the parallel permittivity (in-plane) will display negative values, which denotes the metallic behaviour and the real part of perpendicular permittivity (out-of-plane) will display positive values, which denotes the dielectric behaviour [53].

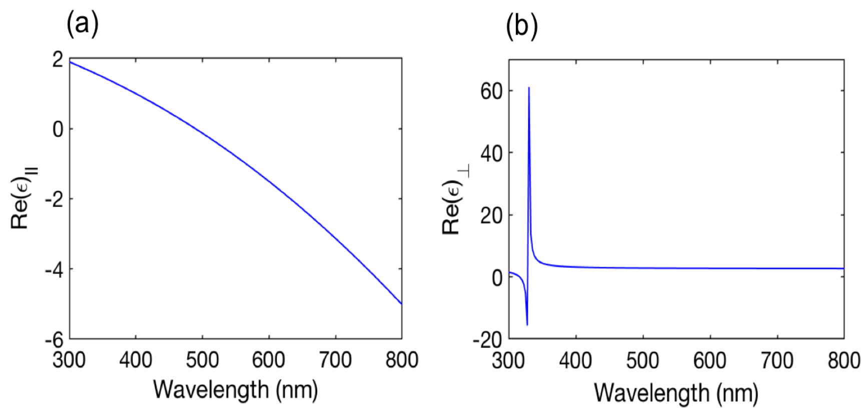

Figure 2.8: (a) Effective parallel and (b) perpendicular permittivity calculated using EMT at normal incidence for a metal fill fraction of 0.19 in the Ag-SiO_2 multilayer stack.

The effect of fill fraction of the metal in the effective permittivity of the multilayer stack is next investigated. The fill fraction is allowed to vary among the values from ρ=0.1 to 0.9 at 0.1 intervals. The results of the effect of fill factor for both polarizations is displayed in Fig 2.9. For parallel permittivity, there is a shift in the ENZ wavelength towards the blue side of the spectrum as the metallic fill fraction increases. This is evident from the fact that, as metallic fill fraction increases, the multilayer stack will behave like a metal and the plasma frequency (ENZ) of metals is in UV region.

The generalized effective medium approximation is the most commonly used method for approximating an effective permittivity tensor for composite structures. However, this method is only valid for a larger number of layers in the stack, because a large number of layers corresponds to an infinite medium. This significantly limit the regime where the effective medium theory is appropriate as a model for physically realizable metamaterials [37].

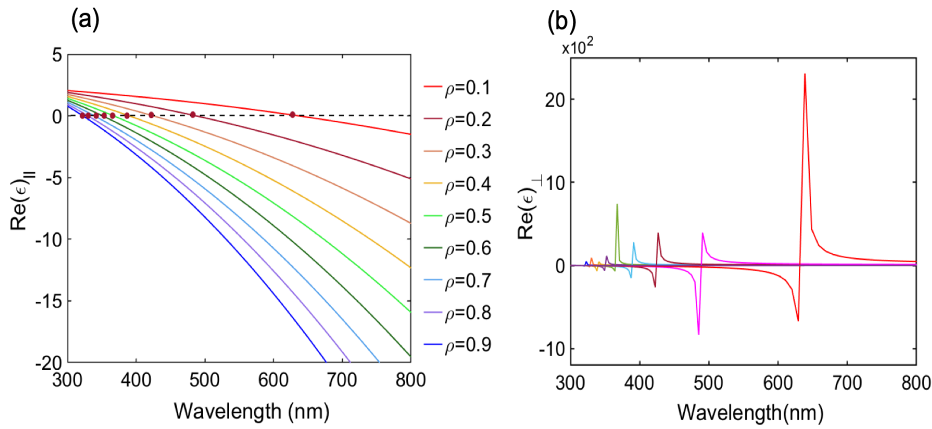

Figure 2.9: (a) Effective parallel and (b) perpendicular permittivities for different metallic fill fractions (the red circle in the parallel permittivity plot (a) denotes the ENZ point for each fill fraction calculated using EMT).

2.3 The retrieval theory

The effective response of a multilayer metal-dielectric stack is often approximated using effective medium theory (EMT), that we discussed in section (2.2). Determining the permittivity of metal-dielectric stacks using EMT is the simplest approach. However, we have to be very careful while using EMT in several aspects because EMT is defined under many approximations. Studies show that effective medium approximation becomes more appropriate for infinite layers [37]. Thus, the effective-medium approach has a rather poor accuracy for finite number of layers and this will limit the regime where EMT can be used to model a realizable design of metal-dielectric composites for specific applications.
The electromagnetic field associated with periodic stacks or photonic crystals has numerous modes. For systems with permittivities exhibiting spatial periodicity, the solutions of Maxwell's equations are Bloch waves [54]. These are the normal modes of any periodic system. In most of the cases, because of the small period, we consider only the zeroth-order mode as being non-evanescent. However, under certain circumstances, the higher-order modes contribute significantly to the field. In these cases, averaging or homogenization process used in EMT will not give reasonable results [49]. Some other studies show that the EMT approximation is mostly valid for low filling fractions, which means when metal layers are thinner [55].

In this section, we present a retrieval method to derive the effective parameters of layered metal-dielectric structures. The first step in this procedure is to obtain the scattering parameters (S-parameters) for a finite-thickness, planar slab of the inhomogeneous structure to be characterized. By inverting the analytical expressions for the S-parameters, one can solve for the refractive index and the impedance. This data can be straightforwardly used to calculate the effective permittivity of the stack for both polarizations. The oblique angles of incidence will sufficiently provide both parallel and perpendicular permittivities.

In a multilayer stack, there will be multiple reflections and transmissions occurring at each interface. They will undergo either destructive or constructive interference. If the field at the beginning of the layer is known, then the field at the end of the layer can be calculated using a simple matrix operation. These coherent optical reflectances and transmittances can be readily

represented as a product of individual matrices at each interface. In other words, the multilayer structure can be regarded as an optical system with one input and one output port and a transfer matrix can be assigned to the system which relates the incident and reflected waves at the input port with the incident and reflected waves at the output port. This matrix method assumes a multilayer structure composed of optically isotropic and homogeneous layers [56].

The transfer matrix method (TMM) predicts the behaviour of multilayer thin film structures in a given configuration. Here we emphasize on scattering matrices obtained using the transfer matrix method for the propagation of light as plane waves through a layered system. For a homogeneous material, the TMM has an analytical form,

$$[\mathrm{T}] = \begin{bmatrix} \cos(\mathrm{nkd}) & -\frac{z}{k}\sin(\mathrm{nkd}) \\ \frac{z}{k}\sin(\mathrm{nkd}) & \cos(\mathrm{nkd}) \end{bmatrix} \tag{2.39}$$

where n is the refractive index of the medium, k is the propagation constant, and d is the thickness of the medium. Writing in terms of the elements,

$$[\mathrm{T}] = \begin{bmatrix} \mathrm{T}_{11} & \mathrm{T}_{12} \\ \mathrm{T}_{21} & \mathrm{T}_{22} \end{bmatrix} \tag{2.40}$$

The scattering parameters (S-parameters) can be found from T matrix as follows [57].

$$\mathrm{S}_{21} = \frac{2}{\mathrm{T}_{11} + \mathrm{T}_{22} + (\mathrm{ikT}_{12} + \mathrm{T}_{21}/\mathrm{ik})} \tag{2.41}$$

$$\mathrm{S}_{11} = \frac{\mathrm{T}_{11} - \mathrm{T}_{22} + (\mathrm{ikT}_{12} - \mathrm{T}_{21}/\mathrm{ik})}{\mathrm{T}_{11} + \mathrm{T}_{22} + (\mathrm{ikT}_{12} + \mathrm{T}_{21}/\mathrm{ik})} \tag{2.42}$$

$$\mathrm{S}_{22} = \frac{\mathrm{T}_{22} - \mathrm{T}_{11} + (\mathrm{ikT}_{12} - \mathrm{T}_{21}/\mathrm{ik})}{\mathrm{T}_{11} + \mathrm{T}_{22} + (\mathrm{ikT}_{12} + \mathrm{T}_{21}/\mathrm{ik})} \tag{2.43}$$

$$\mathrm{S}_{11} = \frac{2\ \det(\mathrm{T})}{\mathrm{T}_{11} + \mathrm{T}_{22} + (\mathrm{ikT}_{12} + \mathrm{T}_{21}/\mathrm{ik})} \tag{2.44}$$

where S_{11} and S_{21} represent the reflection coefficient and transmission coefficient when the incident wave is applied at port 1 and S_{22} and S_{12} represent the reflection coefficient and transmission coefficient when the incident wave is applied at port 2. This is depicted in Fig 2.10.

For homogeneous materials, $S_{21} = S_{12}$ and $S_{11} = S_{22}$. But for inhomogeneous materials, S_{11} and S_{22} are not the same. We find the effective refractive index from the equation (2.3)9 given by

$$\cos(\mathrm{nkd}) = \frac{1 - \mathrm{S}_{11}\mathrm{S}_{22} + \mathrm{S}_{21}^2}{2\mathrm{S}_{21}} \tag{2.45}$$

The S-parameters of a plane wave through an arbitrary multilayer stack using the analytic transfer matrix method is obtained using a script command in Lumerical based on the transfer-matrix-method called "stackrt". For the multilayer stack, the metal is chosen as silver (Ag) and dielectric as silica (SiO_2). For the refractive index and the absorption of these materials, the data reported by Johnson and Christy [50] and Palik [51] is used. The substrate is modelled as glass whose refractive index is approximately 1.5 for a wide range of incident wavelengths. The purpose of the substrate, in general, to hold the material components in place, and its exact

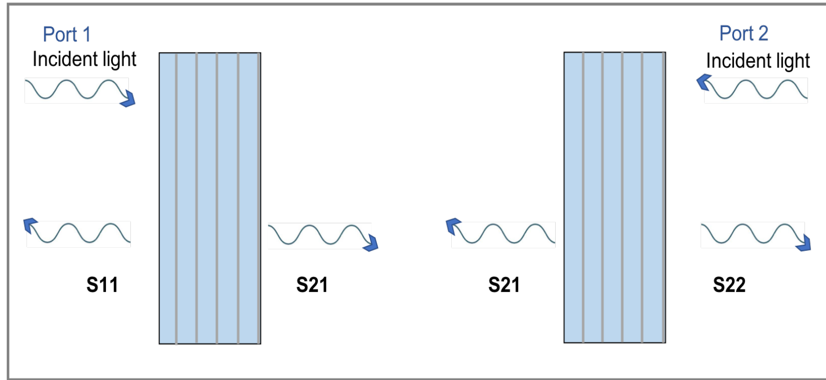

Figure 2.10: S-parameter measurement on a metal-dielectric multilayer stack. S_{11} and S_{22} are the reflection coefficients and S_{21} and S_{12} are the transmission coefficients when the incident light hits on port 1 and port 2, respectively.

physical properties may also vary [58]. Fig 2.11 shows the magnitude of S_{ij} parameters at normal incidence for a homogeneous 80 nm bulk silver and a inhomogeneous 5-layer Ag-SiO_2 multilayer stack with fill fraction of the metal equal to 0.19. In a Ag-SiO_2 multilayer stack, S11 represents the reflection coefficient when the light is incident on the SiO_2 layer. As we mentioned earlier, we can see from the graphs that, for bulk silver $S_{11} = S_{22}$ and for multilayer stack $S_{11} \neq S_{22}$. The origin of the sharp peaks in the dispersion of the S-parameters of the Ag-SiO_2 multilayer stack is not immediately understood, but we believe it will not affect our retrieved permittivity data.

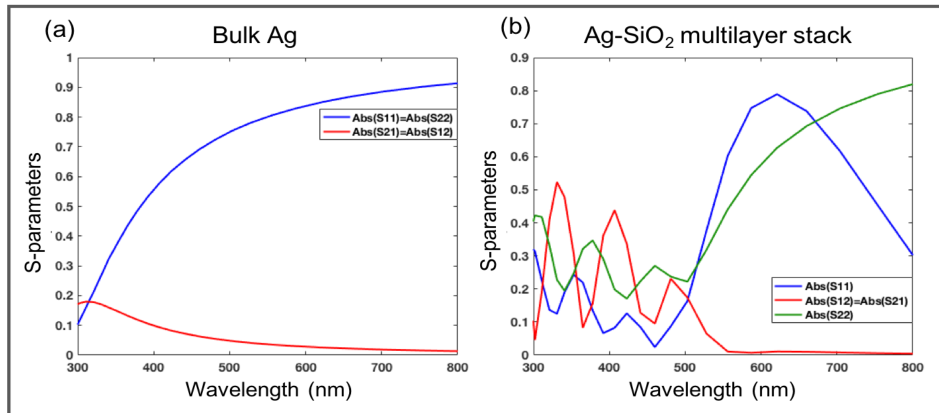

Figure 2.11: Magnitude of S_{ij} parameters for (a) 80 nm silver (b) Ag-SiO_2 multilayer stack.

Using these S-parameters, we retrieved the effective permittivity of a composite structure consisting of 5 bilayers of metal and dielectric with a filling fraction of 0.19. Fig 2.12 shows the retrieved dielectric permittivity of the multilayer stack using TMM. The dielectric permittivity calculated using EMT is also shown for comparison. Although a good agreement between EMT and TMM can be seen in the figure, the approximation for EMT is not valid for smaller number layers. Therefore, TMM is thought to be a more accurate model.

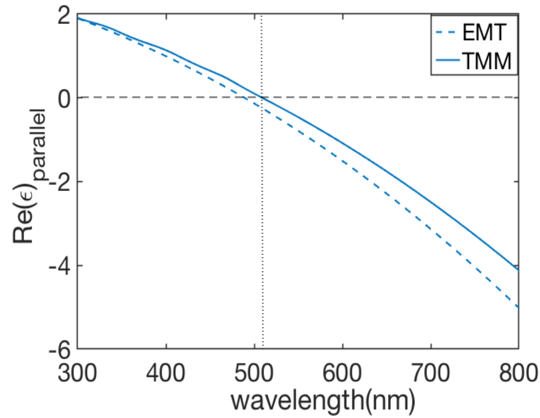

Figure 2.12: Comparison of the dielectric permittivity of a Ag-SiO_2 multilayer stack, with a fill fraction ρ= 0.19, calculated using transfer matrix method (solid line) and effective medium theory (dashed line).

2.4 Nonlinear optical properties of metal-dielectric stack

2.4.1 Nonlinear Optics - A brief Introduction

Nonlinear optics is a branch of optics which deals with the study of phenomena resulting from changes in optical properties caused by high-intensity light like laser sources. As the name "nonlinear" suggests, unlike linear optics, the macroscopic polarization magnitude $\vec{P}(t)$ is no longer linearly proportional to the applied electric field amplitude $\vec{E}(t)$.
In linear optics,

$$\vec{P}(t) = \epsilon_0 \chi^{(1)} \vec{E}(t), \tag{2.46}$$

where, ϵ_0 is the permittivity of the free space and $\chi^{(1)}$ is the linear susceptibility.
In nonlinear optics, $\vec{P}(t)$ can be expressed as the power series in $\vec{E}(t)$.

$$P\vec{(t)} = \epsilon_0[\chi^{(1)}\vec{E}(t) + \chi^{(2)}\vec{E}^2(t) + \chi^{(3)}\vec{E}^3(t) + ...] \tag{2.47}$$

$$= \vec{P}^{(1)}(t) + \vec{P}^{(2)}(t) + \vec{P}^{(3)}(t) + ... \tag{2.48}$$

where, $\chi^{(2)}$ and $\chi^{(3)}$ are second and third order nonlinear optical susceptibilities, respectively [11].

In 1875, John Kerr showed that by the application of a strong DC field, the refractive index in many solids and liquids can be altered. This is the first nonlinear effect observed which is later known as the (DC) Kerr effect. Later in 1894, Friedrich Pockels reported a related effect, where refractive index change is proportional to the electric field. This is now known as Pockels or electro-optic effect. Pockels effect arises only in crystalline materials that lack centro-symmetry. Shortly after the invention of the first laser by Maiman in 1960, Peter Franken and his coworkers carried out the first nonlinear optical experiments using a laser in 1961. They observed the second harmonic generation(SHG) of light in a quartz crystal using a ruby laser. This marked the new era of the nonlinear optics field.

In the next section, a brief introduction to some of the nonlinear effects, which is of interest in this work is given.

2.4.2 Nonlinear Refraction

At high optical intensities, there is an intensity dependent change that occurs to a material's refractive index. This nonlinear index change plays a crucial role in many important nonlinear optical phenomena. The refractive index of the materials due to nonlinearity can be described by the relation,

$$n = n_0 + n_2 I, \tag{2.49}$$

where n_2 is the intensity-dependent refractive index and I is the intensity. This change in the refractive index is called the Kerr effect. The nonlinear susceptibility $\chi^{(3)}$ is related to the nonlinear refractive index n_2 by,

$$n_2 = \frac{3}{2n_0 \mathrm{Re}(\mathrm{n}_0)\epsilon_0 \mathrm{c}} \chi^{(3)}, \tag{2.50}$$

where n_0 is the linear refractive index.

One of the mechanisms caused by the intensity-dependent refractive index is self-focussing. The self-focusing effect is illustrated in Fig 2.13. This occurs when an intense laser beam increases the refractive index of the medium and thus causes the beam to come to a focus within the material. Under these conditions, the material behaves like a positive lens. This effect can even lead to the intensity at the focal spot of the self-focused beam becoming sufficient to create optical damage within the material.

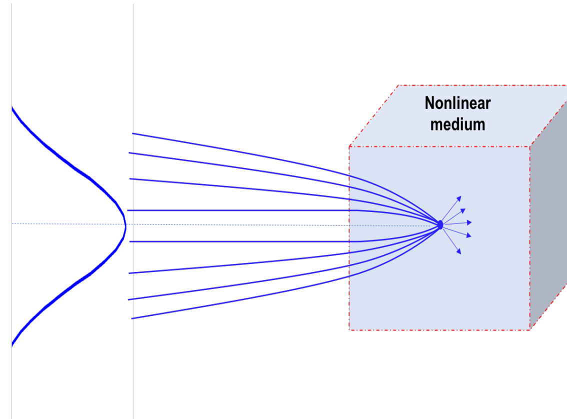

Figure 2.13: Schematic illustration of self-focusing of light.

The power of the laser beam is crucial in determining whether self-focusing will occur. Self-focusing occurs if the radiation power is greater than the critical power for that material.

$$P_{cr} = \frac{\pi(0.61)^2 \lambda_0^2}{8 n_0 n_2}, \tag{2.51}$$

where λ_0 is the vacuum wavelength of the laser source.
For $P >> P_{cr}$, this leads to the breakup of beam into components where each beam has an approximate power of P_{cr}. This process is called filamentation and this occurs as a result of the growth of imperfections of the laser wavefront by means of the amplification associated with the forward four-wave mixing process.

The relationship between nonlinear susceptibility and nonlinear refractive index in the context of metal-dielectric multilayer stacks will be different from that of equation (2.50), because the

latter assumes a homogeneous medium. A theoretical analysis of the nonlinear susceptibility of a composite material was performed by Boyd et *al* in 1994 [59]. Assuming that each component of the composite structure has a third-order nonlinear susceptibility given by $\chi_m^{(3)}$, for metal, and $\chi_d^{(3)}$, for dielectric, we can denote the effective nonlinear susceptibility of the composite as [59],

$$\chi_{\text{eff}}^{(3)} = \frac{\frac{\rho\chi_m^{(3)}}{|\epsilon_m|^2{\epsilon_m}^2} + \frac{(1-\rho)\chi_d^{(3)}}{|\epsilon_d|^2{\epsilon_d}^2}}{\left| \frac{\rho}{\epsilon_m} + \frac{(1-\rho)}{\epsilon_d} \right|^2 \left[\frac{\rho}{\epsilon_m} + \frac{(1-\rho)}{\epsilon_d}\right]^2}. \tag{2.52}$$

2.4.3 Multiphoton absorption

In addition to an intensity dependent change of the refractive index, sufficiently intense beams can also induce nonlinear changes to absorption. Linear absorption occurs in semiconductors and insulators if the photon energy is at least larger than the bandgap energy. But if the incident intensity of the laser beam is high enough, it is possible to bridge the bandgap by simultaneous absorption of two or more low energy photons. This occurs when the sum of the photon energies of low energy photons is greater than bandgap energy. This phenomenon is called multiphoton absorption and the nonlinear absorption coefficient is denoted by β. In the linear regime, the absorption rate is proportional to the optical intensity, while in the multiphoton absorption processes of order n, the absorption rate is proportional to the nth power of optical intensity. This gives insight to how the absorption rate can be small for low intensities and can become larger for high optical intensities [11]. The schematic of a two-photon absorption process is shown in Fig 2.14.

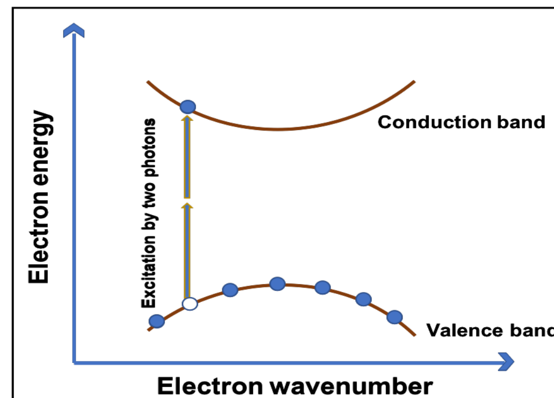

Figure 2.14: Schematic illustration of two-photon absorption.

However, in some cases, high intensities of light can have the saturation of absorption instead. This property of materials by which absorption decreases with the intensity of the radiation is called saturable absorption. After the absorption of a photon by the atom, it requires a certain time to return to its initial state. During this time gap atoms no longer absorbs light. In fact, if the intensity is high enough, the entire medium can saturate. The consequence of this is to induce a reduction in the absorption constant which is proportional to the pump intensity. Saturable absorbers are used for passive mode locking, Q-switching, etc. The dependence of the measured

absorption coefficient α on the intensity I of the incident laser is given by the expression

$$\alpha = \frac{\alpha_0}{1 + I/I_s}, \tag{2.53}$$

where α_0 is the low-intensity absorption coefficient, and I_s is the saturation intensity [11].

We have seen the optical properties of the metal-dielectric multilayer stacks and their constituent materials. In the next chapter, we will see the application of these theories in simulations and experiments.

Chapter 3

Modeling and Simulation

To determine the potential capabilities and fundamental limitations of any optical device, it is necessary to perform simulations before the actual fabrication of the device. This allows us to have a systematic method to design a structure for a specific application. We performed transfer matrix method (TMM) simulations while varying the structural parameters in order to qualify and quantify the linear optical properties of the device. TMM simulations return the scattering parameters of a device and we wrote a retrieval code to extract the effective refractive index from the S-parameters [57, 60]. We wrote a second level of the retrieval code to find an optimal design for the fabrication. In this Matlab code, we varied the thickness of the metal and dielectric layers and thus optimized the design parameters with minimal loss and with the epsilon-near-zero crossing at a designated wavelength.

3.1 Retrieval of the material parameters using transfer matrix method simulations

Following the steps described in section 2.3, the retrieved material parameters for a multilayer stack are presented below. The retrieved material parameters of a bulk silver sample (80 nm thick) and a multilayer stack composed of 5 alternating layers of Ag (16 nm thick) and SiO_2(65 nm thick) are shown in Fig 3.1. The parallel permittivity of the bulk Ag calculated at normal incidence shows the Drude behaviour of the metal. For the multilayer stack, the zero crossing wavelength is shifted to the red side of the spectrum with respect to the bulk Ag. The reason for this shift is attributed by the presence of SiO_2 layers alternately placed between the Ag layers. This is a consequence of the multiple Bragg reflections created by the periodic arrangement of the metal and dielectric layers. We also compared our results with the parameters obtained using the effective medium theory. As shown in Fig (3.2), the results from the retrieval method (solid line) differ considerably from the generalized effective medium theory (dotted line) results. This discrepancy is expected because of the weaker validity of the approximations made in the effective medium theory. For an Ag thickness of 16 nm and a SiO_2 thickness of 65 nm, the number of bilayers are 5. A better agreement between the TMM results and the effective medium results are expected for large number of layers in the medium.

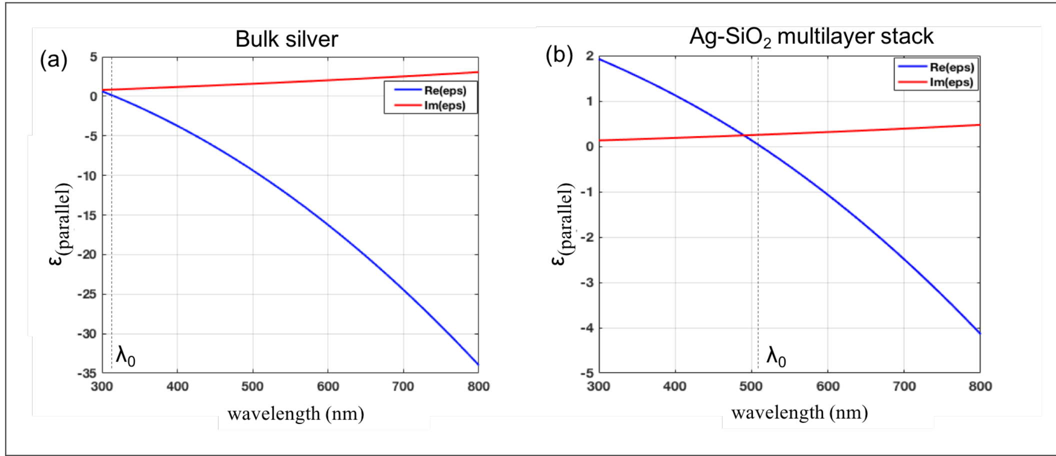

Figure 3.1: $\epsilon_{\text{parallel}}$ for (a) a bulk Ag of 80 nm thick, (b) a multilayer stack consisting of 5 alternating layers of Ag and SiO_2. The zero-crossing λ_0 wavelength is also shown.

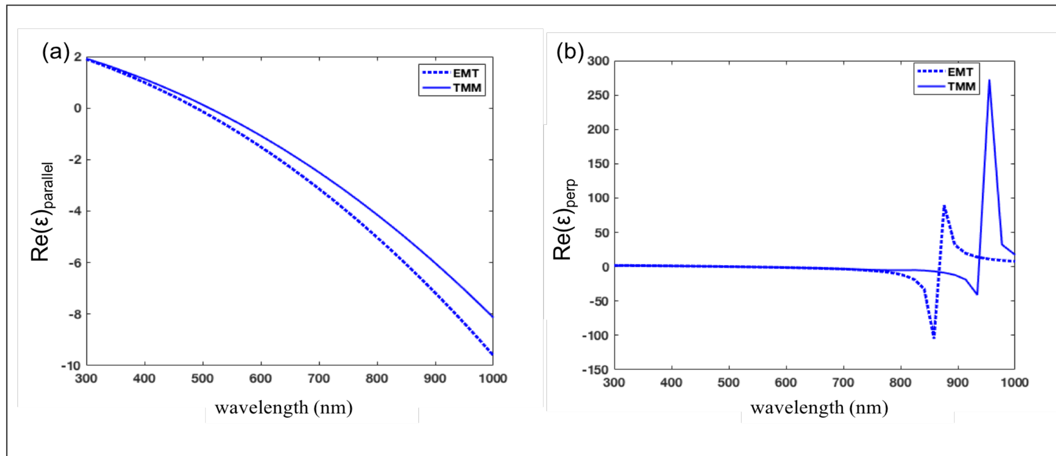

Figure 3.2: Comparison of EMT results with TMM results for the Ag-SiO_2 multilayer sample with a filling fraction of 0.2 for (a) $\epsilon_{\text{parallel}}$ (b) ϵ_{perp} calculated at 10° incident angle. The dotted line represents EMT and solid line represents TMM.

3.2 Design of the sample

An advanced retrieval code is written to optimize the thickness of the metal and dielectric layer of the multilayer stack which corresponds to a minimal loss. An advantage of the metal-dielectric multilayer stack is its ability to tune the ENZ wavelength within the entire visible spectrum. This tunability is achieved by changing the thickness of individual layers in the composite. Fig 3.3 shows the first step in the retrieval process towards optimizing the sample parameters.

The next step is to optimize the thickness of Ag and SiO_2, considering the facts that loss (imaginary part of permittivity) should be minimum and an ENZ wavelength within the range of our applications. The extracted values of permittivities are used to calculate the ENZ wavelength. The ENZ wavelength and losses are plotted as a function of the thickness of Ag in the x-axis and

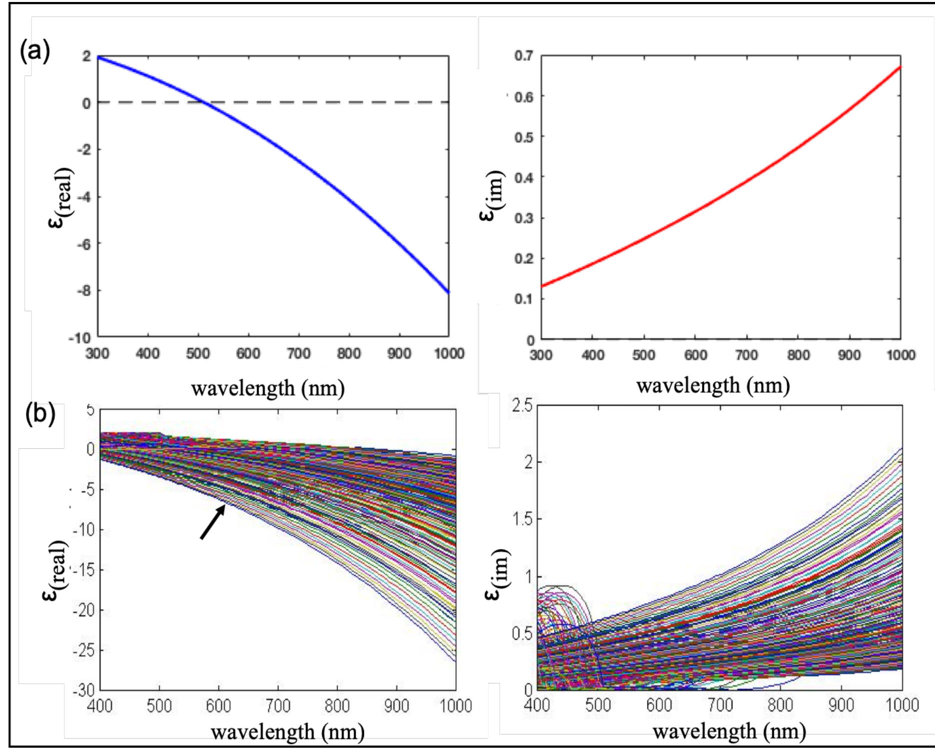

Figure 3.3: Steps in the retrieval process towards optimizing the thickness of the multilayer stack. (a) Extracting ϵ_{real} and ϵ_{imag} of the Ag-SiO_2 multilayer stack for a given thickness of Ag and SiO_2. (b) Repeating the same step by sweeping over a wide range of thicknesses of Ag and SiO_2. The arrow indicates the increasing thickness direction.

the thickness of SiO_2 in the y-axis. The colour map showed in Fig 3.4 serve as a guide chart, from where we can pick the thickness of Ag and SiO_2 for the fabrication. From this design chart, the thickness of Ag is chosen to be 16 nm and thickness of SiO_2 is chosen to be 65 nm. This gives an ENZ wavelength of 509 nm with sufficiently low loss (Im ϵ) 0.2 to allow for practical transmission measurements.

The electric field distribution within a bulk Ag of thickness 80 nm and a Ag-SiO_2 multilayer stack of overall thickness 405 nm is shown in Fig 3.5. Here the electric field is normalized to the value of the incident electric field. In Ag-SiO_2 multilayer stack, 80 nm bulk Ag is split into five 16 nm sublayers and embedded between 65 nm of SiO_2 in a periodic fashion. As we can see, the field distribution inside the metal has an exponential decay. By employing multiple Bragg reflections, the field inside the Ag-SiO_2 multilayer can be modified to allow more transmission. If we look at the dispersion relation of metals, the modes would be evanescent. But for the combined system, it supports the propagation of modes which would normally be evanescent, and these modes travel in a preferred direction. This can be explained based on the coupling to surface plasmons that exist on the metal-dielectric boundaries as light travels through the sample [48].

The electric field distribution as a function of wavelength is calculated using TMM and shown in Fig (3.6). An enhancement in the electric field is observed at the ENZ wavelength. This can be explained based on the boundary conditions we discussed in subsection 2.2.2. The reason

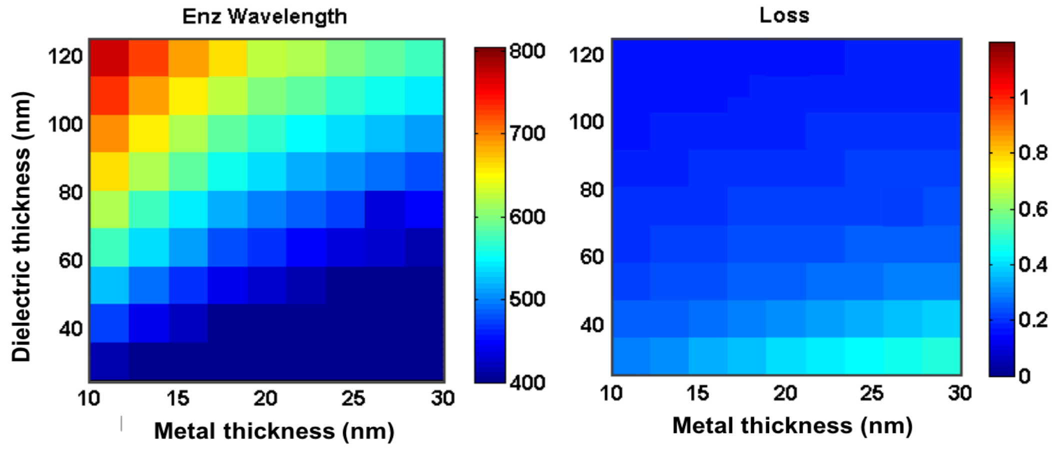

Figure 3.4: The ENZ wavelength and loss of a 5-layer Ag-SiO_2 multilayer stack as a function of thickness of Ag and SiO_2. Note the tunability of ENZ wavelength in the entire visible spectrum.

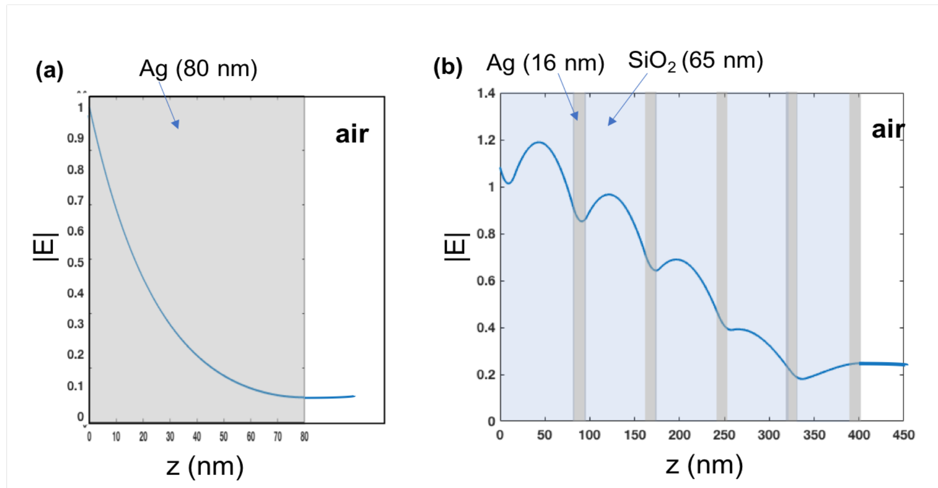

Figure 3.5: Electric field distribution in (a) 80 nm bulk Ag (b) multilayer stack with Ag and SiO_2 layer thicknesses of 16 and 65 nm, respectively, at the ENZ wavelength.

for the magnitude of the electric field going beyond 1 is the back reflection. When light is polarized perpendicular to the layers, the normal component of the D field is continuous at the interfaces and can be written as, $\mathrm{D}^{\perp}_{\mathrm{Ag-SiO_2}} = \mathrm{D}^{\perp}_{\mathrm{air}}$. This yields the following relation for the field components normal to the interface: $E^{\perp}_{Ag-\mathrm{SiO_2}} = \mathrm{E}^{\perp}_{\mathrm{air}}/\epsilon_{\mathrm{eff}}$. In the ENZ regime, ϵ_{eff} approaches zero and this results in a huge enhancement in the electric field. However, this is limited by the non-vanishing imaginary part of the dielectric constant.

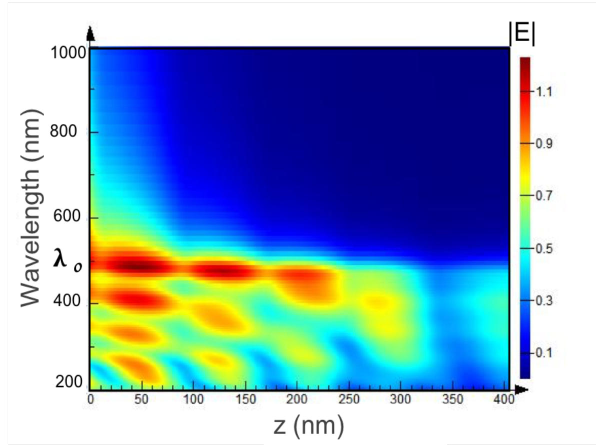

Figure 3.6: Electric field distribution of the Ag-SiO_2 multilayer stack as a function of wavelength. Note the electric field enhancement at λ_0.

3.3 Anisotropic behaviour of the metal-dielectric stack

An anisotropic material is a class of material in which one of the components of the dielectric permittivity tensor has different values in different directions. A multilayer consisting of alternating layers of metal and dielectric gives rise to extreme anisotropy. Even though each layer can be described by a homogeneous and isotropic permittivity parameters, when the layers are of sub-wavelength thickness, we can treat the whole system as a single anisotropic medium with an effective dielectric permittivity. Since the device is anisotropic, the retrieved permittivities also depend on the polarization of the electric field for oblique incident angles. Here we study the cases when the electric field is polarized parallel (p) and perpendicular (s) to the z-axis of the sample for oblique angles of incidence. At normal incidence, the permittivity in parallel and perpendicular directions are the same but for non-normal incidences, it will change. This is depicted in Fig (3.7). We have shown that, for the non-normal incidence of light, for different polarizations, we have λ_0(p) different from that of λ_0(s) confirming the anisotropy of the sample. In this case, λ_0(p) =1.6 $\times$ λ_0(s), substantiating the type of anisotropy present in the sample is Type 1 anisotropy, where Type 1 anisotropy is defined as the condition when $\epsilon_p > 0$ and $\epsilon_s < 0$ in the zero crossing wavelength range [61]. In s polarization, as the incident angle changes, the zero crossing wavelength λ_0 remains the same as in normal incidence case. At the same time, for p polarization, λ_0 undergoes a shift to the higher wavelength side as we increase the angle of incidence as shown in Fig 3.8. This is another demonstration of the strong anisotropy in the metal-dielectric multilayer sample.

The electric field distribution is calculated as a function of incident angle for both polarizations. Since the sample is anisotropic, the electric field distribution will be different for s and p polarizations. In s polarization, we can see that the enhancement in the electric field is maximum around λ_0(s)= 508 nm for all angles of incidence. But for p polarization, the electric field enhancement shifts to higher wavelength side confirming the results shown in Fig 3.8. This is illustrated in Fig 3.9 for both s and p polarizations.

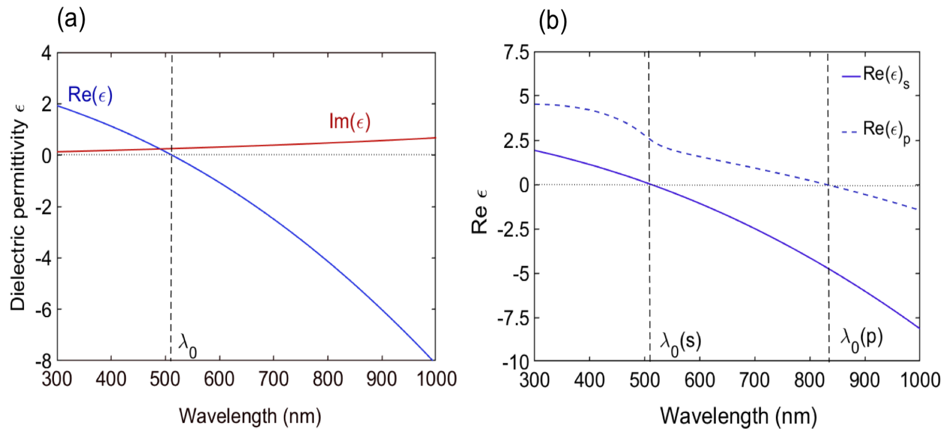

Figure 3.7: Permittivity of the Ag-SiO_2 multilayer stack for parallel (p) and perpendicular (s) polarizations (a) at normal incidence (b) at an oblique angle of incidence (10°).

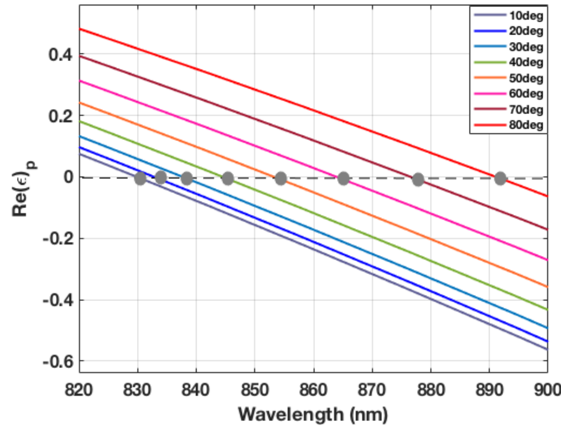

Figure 3.8: Shift in λ_0(p) of the Ag-SiO_2 multilayer stack for different angles of incidence for p polarized light.

3.4 Transmission and reflection simulations

We study theoretically the linear transmission and reflection of the multilayer stack using TMM simulations. Two sets of simulations are done for a plane wave that was polarized parallel and perpendicular to the layers in the composite. Also, the simulations are done for various angles of incidence. As a first step, a Ag-SiO_2 multilayer stack is modelled based on the Ag and SiO_2 dielectric data according to Johnson and Christy [50] and Palik [51], respectively. An illustration of the plane wave incident on a Ag-SiO_2 multilayer stack is shown in Fig (3.10). When light is coming at normal incidence, the transmission and reflection in both parallel (p) and perpendicular (s) polarizations will remain the same. Fig 3.11 displays the transmission and reflection of the multilayer stack at normal incidence and Fig (3.12) shows the transmission and reflection at oblique incidence for both s and p polarizations. The sample's reflectance and

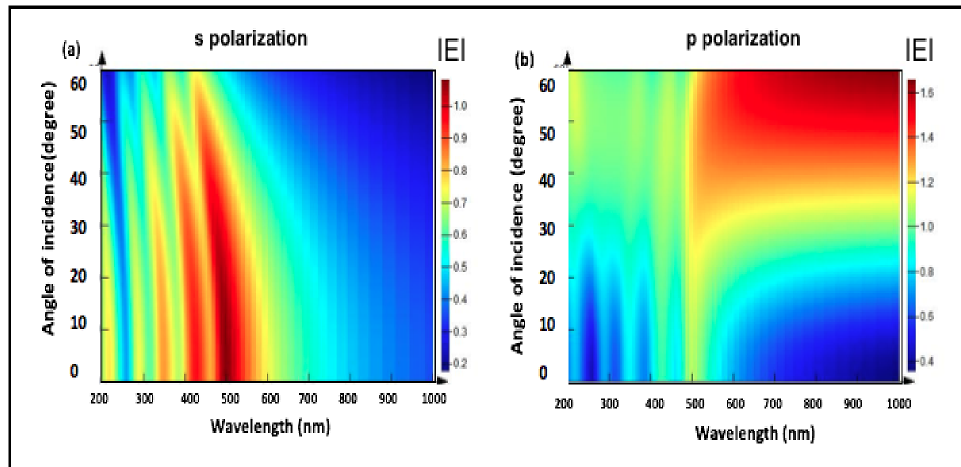

Figure 3.9: Electric field enhancement of the Ag-SiO_2 multilayer stack as a function of angle for (a)s polarization (b) p polarization.

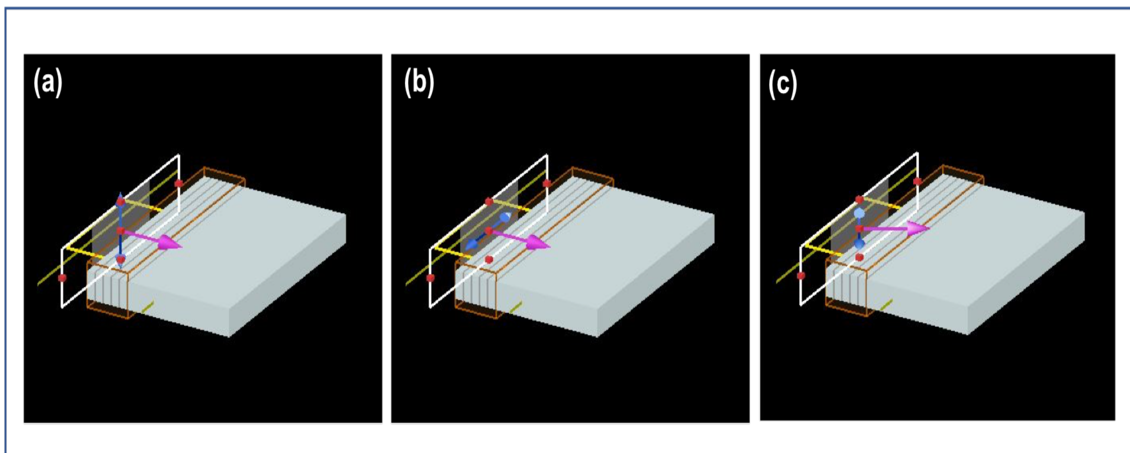

Figure 3.10: An illustration of a plane wave incidence on a Ag-SiO_2 multilayer stack (a) When light is polarized perpendicular to the layers (b) when light is polarized parallel to the layers (c) When light is coming at an oblique angle of incidence.

transmittance spectra in s and p polarization was calculated as the function of the incidence angle is shown in Fig 3.12 (a) to (d). As we can see from the figure, the transmission goes down for longer wavelengths while reflection goes up. This is because, at higher wavelengths the metallic property dominates in the metal-dielectric composites. For s polarization, transmission and reflection do not change considerably as a function of angle of incidence, while in p polarization, a considerable change is observed. This is consistent with the simulation results for electric field enhancement depicted in Fig 3.9.

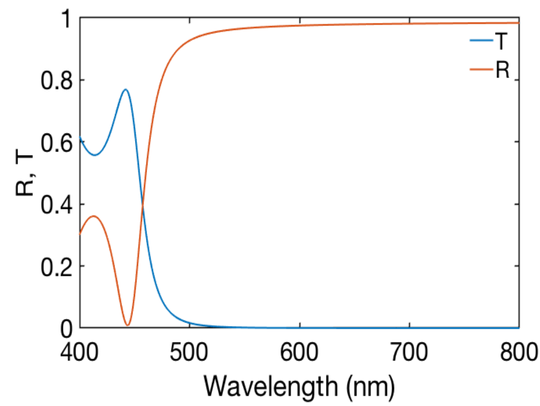

Figure 3.11: Transmission and reflection of the Ag-SiO_2 multilayer stack extracted from TMM simulations at normal incidence.

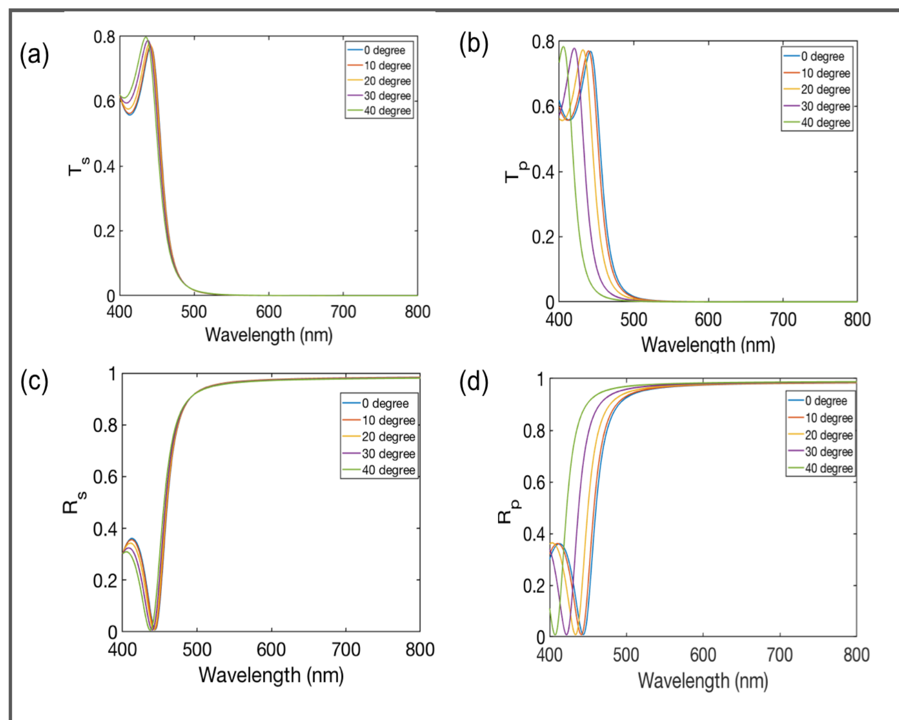

Figure 3.12: Transmission and reflection spectra of the Ag-SiO_2 multilayer stack calculated using TMM simulations for various angles of incidence for both s (a and c) and p (b and d) polarizations.

Chapter 4

Optical characterization of metal-dielectric composites

In this chapter, we provide a brief overview of the techniques we used to characterize our metal-dielectric multilayer sample. The working principles and theory are explained in detail.

4.1 Fabrication of metal-dielectric multilayer stacks

The design of the metal-dielectric multilayer stack using transfer matrix method was discussed in previous chapter. Having established a design for the Ag-SiO_2 multilayer stack that has both a desired epsilon-zero-crossing and a small amount of loss, we investigate fabricating a practical device and designing an experiment for its characterization.

The sample was fabricated using an e-beam evaporation technique. Electron beam evaporation technique is a form of physical vapour deposition method in which the target material to be used to be deposited on the substrate is bombarded with an electron beam from a charged tungsten filament. The electron beam evaporates and converts the target material to a gaseous state for deposition on the material to be coated. The atoms or molecules in the gaseous state then precipitate and form a thin film coating on the substrate. The whole process is taking place in a high vacuum chamber. Starting with a 1.1 mm thick microscopic glass slide as the substrate, Ag films and SiO_2 films were deposited with a Angstrom Nexdep Series Thermal/Electron Beam Evaporator. This evaporator offers automated vacuum operations and deposition rate control and has the capability to uniformly deposit across a large target area. The deposition rates of Ag and SiO_2 layers were 1 Å/s. The Scanning electron microscopy (SEM) image of the fabricated sample is shown in Fig 4.1. The top layer of the Ag-SiO_2 multilayer stack, which is in contact with air, is the SiO_2 layer. This is done in order to prevent the oxidation that might happen to the Ag layer when exposed to air. A close examination of the top layer of the sample is done and ensured surface uniformity.

4.2 Linear characterization

In this section, we briefly explain different experimental techniques we used for the linear characterization of our multilayer stack.

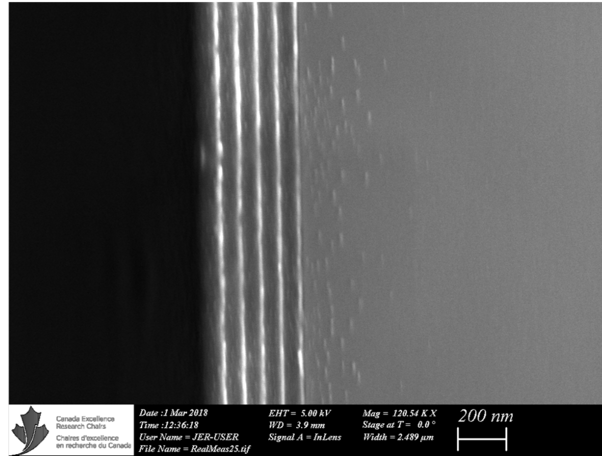

Figure 4.1: Scanning electron microscopy image of the Ag-SiO_2 multilayer stack. There are a total of 5 bilayers of Ag (bright) and SiO_2 (dark). The top layer is SiO_2 to prevent the oxidation of Ag when exposed to air.

4.2.1 Spectroscopic ellipsometry

Spectroscopic ellipsometry is a widely used optical metrology technique for determining the thin film thickness and optical constants (n, k). The ellipsometer does not measure the refractive index directly; instead, it measures the change in polarization of the light as it is reflected from the surface of a film or stack of films. These data are very useful and can be used to extract many pieces of information from the sample under investigation. The mathematical theory for ellipsometric analysis is based on the Fresnel reflection or transmission equations for polarized light encountering boundaries in planar multilayered materials. If the refractive index of the film is known, we can calculate the film thickness and vice versa. The same is applicable to the multilayer structures. If we know the thickness of each layer, we can calculate the effective index of the stack considering it as an effective medium. The procedure for the ellipsometry method is as follows [62].

- The ellipsometric angles Ψ and Δ as a function of wavelength are collected.
- A model of the sample to determine the sample parameters is created.
- Once the model is built, the calculated data is fitted to the experimental data and the best-fit is determined.
- The best-fit model is then evaluated and make sure the predictive model is physically reasonable and whether the different parameters are unique and are not correlated.

The fundamental equation of ellipsometry is given by

$$\rho = \tan(\Psi) \exp i\Delta, \tag{4.1}$$

where Ψ and Δ are the measured ellipsometric parameters and ρ is the ratio of Fresnel reflection coefficients of the p and s polarization of the incident light, respectively.

We tried to determine the permittivity of the layered metal-dielectric composite using a Horiba JOBINYVON Spectroscopic Ellipsometer. It is necessary to create a model of the sample

to determine the sample parameters. Since our sample contains both metal and dielectric, we created a Drude-Lorentz model to fit the experimental results which take into account both the metal and dielectric properties. Once the model is built, the calculated data must be fitted to the experimental data and the best match between the two sets has to be found.

One of the potential problems that can arise when dealing with the layered metal-dielectric composite structures is, the accuracy reduces as the number of layers increases. Since our sample has five bilayers, this can turn out to be a problem. For a fully transparent sample, the refractive index and thickness can be simultaneously determined, but if the sample has some absorption, then the solution matching the change in polarization to the thickness and the refractive index will not be unique. The Horiba Spectrometer we used for the measurement is a fixed-angle ellipsometer. Since our metal-dielectric stack is an anisotropic sample, the need for angular dependence measurements seems to be very crucial in this case. Taking into account of these potential problems, a supplemental linear characterization technique is also required to arrive at a unique solution.

Another approach: Modelling in ellipsometry becomes tricky when we have complex samples. Knowing this fact we tried another method. We relied upon ellipsometry only to collect the primary data Ψ and Δ. Then we used these values to extract the real and imaginary part of the refractive index without going into the process of modelling. This method is referred to as the direct inversion method. The details of this method are given in the appendix. The refractive index values calculated using the direct inversion method were not in agreement with the effective medium theory and hence this method is ruled out. This method needs a lot of computation time and advanced simulation routine for dealing anisotropic inhomogeneous multilayer samples.

4.2.2 Transmittance and reflectance

The transmittance of the sample was measured using an Ocean optics spectrophotometer. We used a super-continuum laser as the light source. In this method, a beam with a wavelength ranging from UV to NIR passes through the sample. The sample absorbs this radiation. The amount of radiation that is absorbed depends on the sample properties. When radiation is absorbed by the sample, the energy of the atoms in the sample increases and a spectrum is obtained. Transmission measurements were done for a few sets of incidence angles. The sample is placed in a rotation stage. The technique we used to to derive effective parameters is based on the simulated or measured reflection and transmission coefficients of the metal-dielectric stack. We assumed the stack to be a homogeneous medium with complex permittivity. By inverting the analytical expressions for R and T, one can solve for the refractive index and the impedance. Then, this data can be used to calculate the permittivity of the multilayer stack [63]. A schematic diagram of both linear characterizations is shown in Fig 4.2.

4.3 Nonlinear characterization: Z-scan technique

4.3.1 An overview of the technique

Z-scan technique is a single beam spectroscopic technique used to measure both the two-photon absorption coefficient and the nonlinear refractive index in samples [64]. The transmittance of the beam through the sample before and after the focal position is recorded in the far-field as a function of the position z. There are two types of measurement techniques, one is the open-aperture method and other is the closed-aperture method. In the open-aperture method, the entire transmitted beam is collected. This method is only sensitive to the nonlinear absorption and is used to obtain the nonlinear absorption coefficient, β. This can be used to extract the

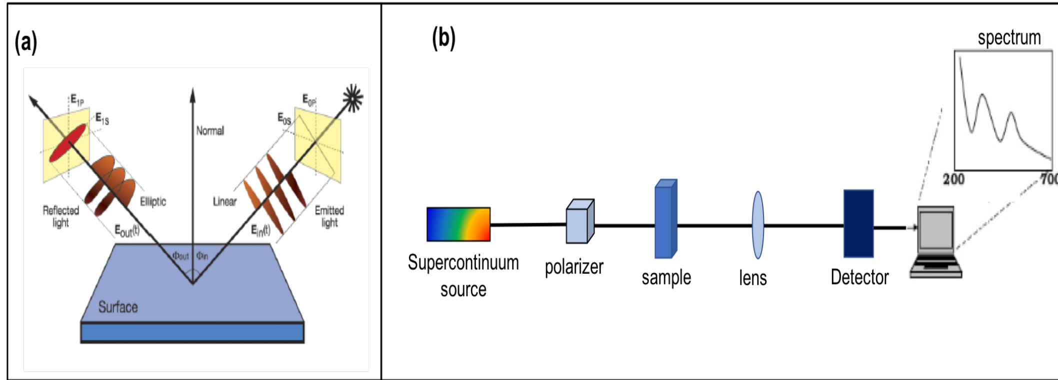

Figure 4.2: Linear characterization techniques (a) Ellipsometry (b) Spectroscopy

imaginary part of $\chi^{(3)}$. The closed-aperture method is sensitive to both nonlinear refraction and nonlinear absorption. Hence it is necessary to first extract the imaginary part of the phase shift from the open-aperture scan for calculating the real phase shift from the closed-aperture scan. Before the actual nonlinear characterization of our metal-dielectric multilayer stack, the experimental setup need to be calibrated with known samples such as carbon-disulphide (CS_2) or fused silica. The configuration of the Z-scan setup is shown in Fig 4.3.

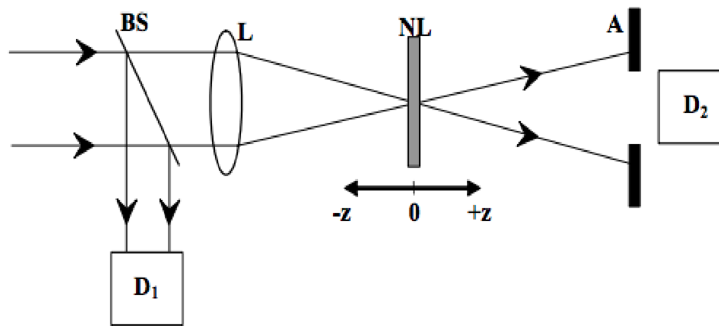

Figure 4.3: Schematic diagram of a Z-scan technique. BS is a beamsplitter, L is a focusing lens, D_1 is a reference detector and D_2 is a probe detector. The sample moves between -z to +z position in a translation stage. A is an aperture for the closed-aperture measurements.

The nonlinear absorption coefficient β can be determined directly from the open-aperture measurements. In the open-aperture measurements, the aperture is removed and the total transmittance is collected using a lens. By measuring the whole signal, the beam small distortions become insignificant which makes the measurement insensitive to beam size variations due to nonlinear refraction. Thus, the measured transmittance is then independent of the nonlinear refraction and only dependent on the nonlinear absorption. For a Gaussian beam, the normalized transmittance is given by

$$T_{\mathrm{OA}}(z) = 1 - \frac{\Delta\Psi}{1+x^2}, \tag{4.2}$$

where $x = z/z_0$ and z_0 is the Rayleigh length, and $\Delta\Psi = \frac{1}{2\sqrt{2}}\beta I_0 L_{\mathrm{eff}}$.

The transmission data collected from the open-aperture detector when plotted against the position depicts a valley or peak symmetric around the focus. The multi-photon absorption suppresses the peak and enhances the valley, while saturation produces the opposite effect [64].

In the closed-aperture measurement, only a small part of the intensity transmitted through the sample is collected. Thus, the variations in the transmission correspond to both nonlinear absorption and self-focusing or defocusing caused by the nonlinear refraction. When the sample is moved along the z-axis, the sample acts as a lens of variable focal length. The shape of the graph for a closed-aperture scan is different for material with negative and positive nonlinear refractive index. Let us consider a sample with negative nonlinear refractive index. When the sample is far from the focus, the laser intensity will be low and the sample exhibits a very small nonlinear refractive index. As the sample comes closer to the focus, it acts as a negative lens and starts collimating the beam. Thus, it has a smaller spot size at the aperture which results in higher transmittance through the aperture. This effect increases as we move closer and closer to the focus and maximum transmittance will occur just in front of the focus. As we continue to move the sample forward past the focus, the beam starts diverging because of the negative lensing and hence, the transmittance keeps on decreasing as we move farther and farther from the focus. Thus the overall graph looks like a peak followed by a valley for negative refractive index materials. For a positive refractive index materials, the graph is inverted, valley followed by a peak. The direct impact of this is, by looking at the shape of the graph we know the sign of the nonlinear refractive index. Fig 4.4 shows the closed-aperture signal for a sample with a positive and negative nonlinear refractive index [65].

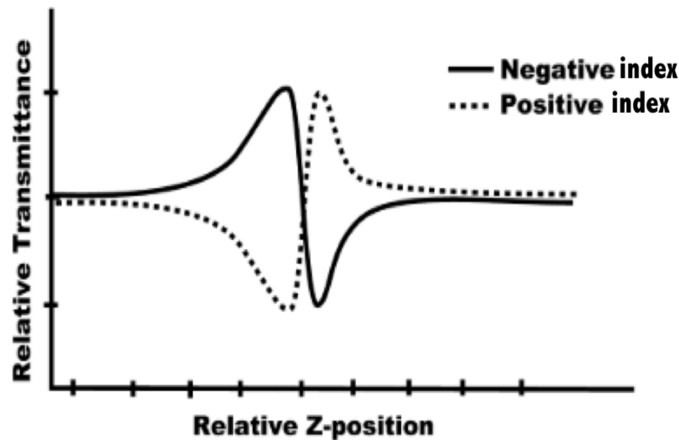

Figure 4.4: A representative closed-aperture Z-scan signal showing both positive (dotted line) and negative (solid line) nonlinear refractive index.

In most cases the closed-aperture Z-scan signal is actually a combination of the nonlinear refraction and nonlinear absorption. This implies that the nonlinear refraction will not occur on its own, but along with the nonlinear absorption. Therefore, we need both closed- and open-aperture signals to extract the nonlinear refraction. However, the open-aperture signal, which measures the total transmittance of the sample, is independent of the nonlinear refraction and is only dependent on the nonlinear absorption. There is a common practice of dividing the closed-aperture signal with the open-aperture signal to obtain the nonlinear refraction. This is primarily based on the approximation discussed by Sheik Bahae *et al.* that Z-scan is not dominated by the nonlinear absorption. Fig 4.5 is an example of this division process [65]. This simple division

gives a curve that closely approximates what would be obtained with a closed-aperture Z-scan signal on a material having the same nonlinear refractive index but no nonlinear absorption. For a Gaussian beam, the normalized change in transmittance is given by

$$T_{\text{CA}} = 1 + \frac{4(z/z_0)\Delta\Phi}{(1+(z/z_0)^2)(9+(z/z_0)^2)} \tag{4.3}$$

where $\Delta\Phi$ is defined as the real part of nonlinear phase shift given by $\Delta\Phi$= $(1\text{-S})^{0.25}$ k $n_2 I_0 L_{\text{eff}}$. These equations are explained in detail in the next section.

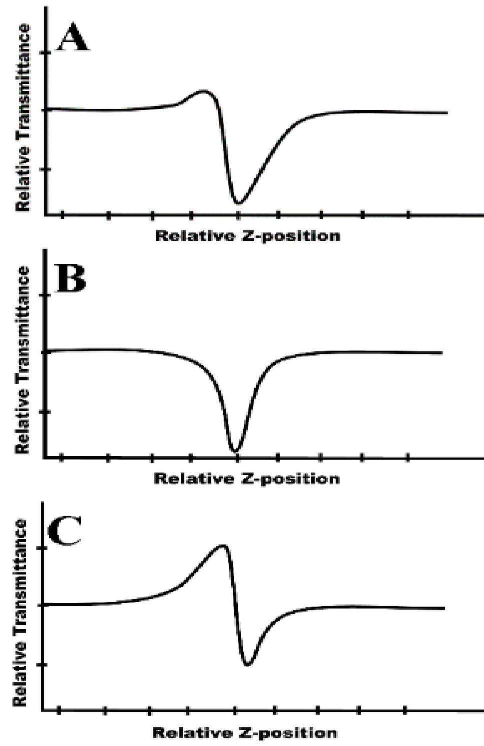

Figure 4.5: Representative Z-scan signals (A) a closed-aperture signal, (B) an open-aperture signal, (C) division of a closed-aperture signal with an open-aperture signal.

4.3.2 Z-scan theory

In this section, we will discuss the theory of the Z-scan technique. Any assumptions and simplifications we used in deriving the Z-scan equations are taken from the pioneer work by Sheik Bahae *et al.* [64, 66].

Nonlinear refraction: The primary assumption for explaining the Z-scan theory is, the incident beam interacting with the matter is described as a linearly polarized Gaussian electric field. Then the equation for finding the nonlinear refraction from the Z-scan data will be derived from the properties of Gaussian beam as a function of sample position, the phase shift introduced

by the sample, the propagation of Gaussian beam through free space up to the aperture, and the transmittance of the beam through the aperture. The electric field of the Gaussian beam can be expressed as

$$E(r,t,z) = E_0(t)\frac{w_0}{w(z)}\exp(-\frac{r^2}{w^2(z)} - \frac{ikr^2}{2R(z)})e^{-i\phi(z,t)}, \tag{4.4}$$

where z is the distance from the waist and w_0 is the beam waist radius in the focal plane. $E_0(t)$ contains the temporal envelope of the laser pulse and denotes the electric field at the waist. The beam radius $w(z)$ can be expressed as a function of position through the relation,

$$w(z) = \sqrt{w_0^2\left(1 + \frac{z^2}{z_0^2}\right)}, \tag{4.5}$$

and the radius of curvature $R(z)$ can be explained as

$$R(z) = z\left(1 + \frac{z^2}{z_0^2}\right). \tag{4.6}$$

The Rayleigh length or the diffraction length of the beam is given by

$$z_0 = kw_0^2/2, \tag{4.7}$$

where $k = 2\pi/\lambda$.

The term $e^{-i\phi(z,t)}$ in equation (4.4) contains all the radially uniform phase variations. As we are only concerned about radial phase variations $\Delta\Phi(r)$, the slowly varying envelope approximation (SVEA) applies, and all other phase changes that are uniform in r are ignored. Therefore, $e^{-i\phi(z,t)}$ is omitted from following analysis of the Z-scan theory. The SVEA assumes that the magnitude and phase of the forward travelling wave amplitude vary slowly in space and time compared to the entire optical wavelength and period respectively. If the sample length is small enough such that changes in the beam diameter within the sample due to either diffraction or nonlinear refraction can be neglected, the medium is regarded as thin. In the thin film approximation, the sample thickness is regarded as smaller than the diffraction length ($L < z_0$). These approximations allow one to neglect the changes in the beam diameter within the sample due to the linear diffraction and nonlinear refraction. So this allows the laser-sample interaction to happen only at one position rather than spreading through the entire interaction region. By satisfying these conditions we can treat the self refraction effect as 'external self action'. For linear diffraction, this condition is shown as $L << z_0$, while for nonlinear refraction, it will be $L << z_0/\Delta\Phi_0$. In most Z-scan experiments, the condition for nonlinear refraction is found to be automatically satisfied since the value of $\Delta\Phi$ is small. Under these assumptions, the amplitude and nonlinear phase change $\Delta\Phi$ of the electric field within the sample are now governed by equations,

$$\frac{d\Delta\Phi}{dz'} = \Delta n(I)k \tag{4.8}$$

$$\frac{dI}{dz'} = -\alpha(I)I, \tag{4.9}$$

where z' is the propagation depth in the sample and $\alpha(I)$ includes linear and nonlinear absorption terms. If we are considering only the cubic nonlinearity and if the nonlinear absorption is negligible, the solution of the differential equations (4.8) and (4.9) gives us the phase shift $\Delta\Phi$ at the exit surface of the sample. It follows the radial variation of the incident radiation as a function of the position z of the sample, given by

$$\Delta\Phi(z,r,t) = \Delta\Phi_0(z,t)\exp\left(-\frac{2r^2}{w^2(z)}\right), \tag{4.10}$$

where

$$\Delta\Phi_0(z,t) = \frac{\Delta\Phi_0(t)}{1+\frac{z^2}{z_0^2}}, \tag{4.11}$$

where $\Delta\Phi_0(t)$ is the on-axis phase shift at the focus, given by

$$\Delta\Phi_0(t) = k\Delta n_0(t)L_{\text{eff}}, \tag{4.12}$$

where L_{eff} is the effective length and $\Delta n_0 = n_2 I_0(t)$ with $I_0(t)$ as the on-axis intensity at the focus (z=0) since we ignored the fresnel reflection losses. The electric field distribution exiting from the sample including the nonlinear phase distortion is given by

$$E_e(r,z,t) = E(z,r,t)e^{-\alpha L/2}e^{i\Delta\Phi(z,r,t)}. \tag{4.13}$$

By using this complex electric field exiting from the sample, we can deduce the far-field pattern of the beam at the aperture using Huygen's principle by performing a zeroth-order Hankel transformation of E_e. Rather than performing this complicated procedure, a simpler approach to this is the Gaussian decomposition (GD) method. In the GD method, the complex electric field at the exit plane of the sample is decomposed into a summation of Gaussian beams through a Taylor series expansion of the nonlinear phase term. In this approach, only small phase changes are considered, which implies that only the first few terms of the Taylor expansion need to be considered. The Taylor series expansion of the nonlinear phase shift, $e^{i\Delta\Phi(z,r,t)}$, is given by

$$e^{i\Delta\Phi(z,r,t)} = \sum_{m=0}^{\infty} \frac{i\Delta\Phi_0(z,t)^m}{m!} e^{-2mr^2/w^2(z)}. \tag{4.14}$$

Here, each Gaussian beam is propagated individually to the aperture plane and there they resummed to reconstruct the beam. By taking into account the initial beam curvature for the focussed beam, the resultant field pattern at the aperture is given by

$$E_a(r,t) = E(z,r=0,t)e^{-\alpha L/2}\sum_{m=0}^{\infty} \frac{[i\Delta\Phi_0(z,t)]^m}{m!}\frac{w_{m0}}{w_m}.\exp\left(-\frac{r^2}{w_m^2} - \frac{ikr^2}{2R_m} + i\theta_m\right). \tag{4.15}$$

If we are considering d as the propagation distance in the free space from the sample to the aperture, terms in equation (4.15) can be expressed as the following.

$$w_{m0}^2 = \frac{w^2(z)}{2m+1} \tag{4.16}$$

$$w_m^2 = w_{m0}^2\left[g^2 + \frac{d^2}{d_m^2}\right], \tag{4.17}$$

where $g = 1 + d/R(z)$, and R(z) is the radius of curvature.

$$R_m = d\left[1 - \frac{g}{g^2 + d^2/d_m^2}\right]^{-1} \tag{4.18}$$

$$\theta_m = \tan^{-1}\left[\frac{d/d_m}{g}\right] \tag{4.19}$$

$$d_m = \frac{kw_{m0}^2}{2} \tag{4.20}$$

By spatially integrating equation (4.15) up to the aperture radius, we can calculate the power through the aperture. By including a temporal variation of the pulse, the normalized closed-aperture Z-scan transmittance can be obtained as,

$$T(z) = \frac{\int_{-\infty}^{\infty} P_T(\Delta\Phi_0(t))dt}{S\int_{-\infty}^{\infty} P_i(t)dt}, \tag{4.21}$$

where $P_i(t)$ is the instantaneous input power given by

$$P_i(t) = \pi w_0^2 I_0(t)/2 \tag{4.22}$$

and S is the linear transmittance through the aperture given by

$$S = 1 - \exp(-2r_a^2/w_a^2) \tag{4.23}$$

An important thing to consider here is that unless the far field condition for the aperture plane is satisfied, i.e., $d >> z_0$, for a given $\Delta\Phi_0$, the magnitude and shape of T(z) does not depend on the wavelength or geometry. The S term in equation (4.23) plays an important role since large aperture reduces the variations in T(z). For very large aperture or no aperture (i.e, S=1), the variations in T(z) disappear and the value of T(z) becomes 1 independent of the z position or $\Delta\Phi_0$. There is an easily measurable quantity called ΔT_{p-v}, which is the difference between the peak and valley in the transmittance curve of the closed-aperture Z-scan signal as shown in Fig 4.6. The variation of ΔT_{p-v} as a function of $|\Delta\Phi_0|$, for different aperture sizes are done by Sheik Bahae *etal*, and found that dependence is almost linear. Also this value is not dependent on the laser wavelength or geometry. This dependence is described within a 2% accuracy as

$$\Delta T_{p-v} \approx 0.406(1-S)^{0.25}|\Delta\Phi_0|, \tag{4.24}$$

for $|\Delta\Phi_0| \leq \pi$.
In terms of the z position, this can be denoted as $\Delta Z_{p-v} \approx 1.7z_0$. This equation (4.24) can directly be used to calculate the nonlinear refractive index with good accuracy. We can deduce similar equations for higher order nonlinearities also. For example, for the fifth order nonlinearity, the equation for ΔT_{p-v} is given by

$$\Delta T_{p-v} \approx 0.21(1-S)^{0.25}|\Delta\Phi_0|, \tag{4.25}$$

or in terms of the z-position $\Delta Z_{p-v} \approx 0.21z_0$.

Nonlinear absorption : All we discussed above is the closed-aperture Z-scan measurements for extracting the nonlinear refractive index. Now for the open-aperture measurements, we removed the aperture and the whole transmitted light is collected. By doing so, the Z-scan signal will become insensitive to the nonlinear refraction and now it is only a function of the nonlinear absorption. We gets an open-aperture signal that is symmetric around the focus, where there is a minimum transmittance in case of the multi-photon absorption and a maximum transmittance in case of the saturation of absorption. Here we are taking into account of the two-photon absorption. This gives an insight that it is still the third-order nonlinear susceptibility which governs the nonlinear absorption. The complex third order susceptibility is given by

$$\chi^{(3)} = \chi_R^{(3)} + i\chi_i^{(3)}, \tag{4.26}$$

where the imaginary part of susceptibility $\chi_i^{(3)}$ is related to the absorption coefficient β by the relation,

$$\chi_i^{(3)} = \frac{n_0^2\epsilon_0 c^2}{\omega}\beta, \tag{4.27}$$

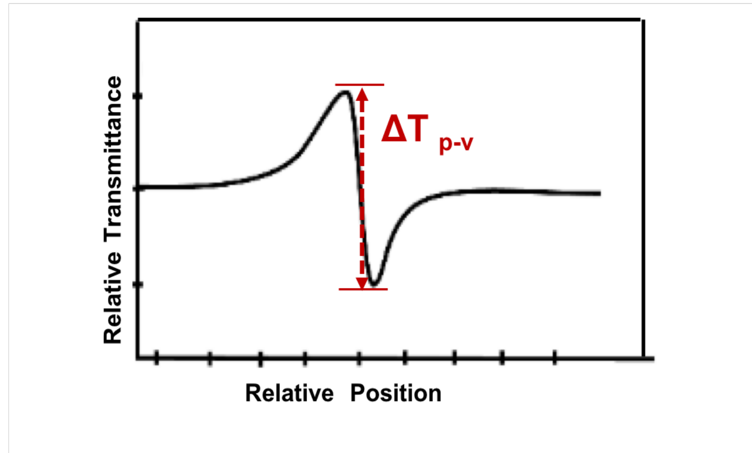

Figure 4.6: An example of peak to valley ΔT_{p-v} calculation in a closed-aperture Z-scan signal

where ω is the optical frequency.
Similarly the real part of susceptibility $\chi_R^{(3)}$ is related to the nonlinear refractive index n_2 by the relation,

$$\chi_R^{(3)} = 2n_0^2\epsilon_0 c n_2 \tag{4.28}$$

Here we are concerned only with the low excitation effects where the free carrier effects (refractive and absorptive) are neglected. In light of these approximations equations (4.8) and (4.9) can be reexamined with following substitution,

$$\alpha(I) = \alpha + \beta I \tag{4.29}$$

This leads to the irradiance distribution and phase shift at the exit surface of the sample given by

$$I_e(z,r,t) = \frac{I(z,r,t)e^{-\alpha L}}{1+q(z,r,t)} \tag{4.30}$$

$$\Delta\Phi(z,r,t) = \frac{k\gamma}{\beta}\ln[1+q(z,r,t)], \tag{4.31}$$

where $q(z,r,t) = \beta I(z,r,t)L_{\text{eff}}$ and L_{eff} is the effective length of the sample. After solving a series of equations and assuming a Gaussian pulse, we will arrive at the final equation for the normalized transmittance of the sample from the open-aperture Z-scan measurement. This is given by

$$T(z) = \sum_{m=0}^{\infty}\frac{[-q_0(z)]^m}{(m+1)^{3/2}}, \tag{4.32}$$

where q_0 is defined as,

$$q_0 = \frac{\beta I_0 L_{\text{eff}}}{1+\frac{z^2}{z_0^2}}. \tag{4.33}$$

The nonlinear absorption coefficient, β, can be determined by fitting this function in equation (4.32) to the transmittance data obtained from the Z-scan signal in the open-aperture mode. After obtaining β, n_2 can be determined from the closed-aperture Z-scan signal.

Chapter 5

Experiment and methods

An accurate technique for determining the film thickness and optical constants is important for the complete characterization of the sample. In this chapter, we will explain the linear and nonlinear experimental characterization techniques we adopted for the characterization of the metal-dielectric multilayer stack.

5.1 Linear measurements

The effective medium approximation (EMA) has been widely applied to model the effect of a solid sample with surface roughness in spectroscopic ellipsometry (SE). There are two specific cases to utilize the EMA model. One is utilizing the EMA model to perform the inversion of the optical constants of solid samples from the SE measurements. Another is utilizing the EMA model to estimate the thickness of the rough layer at the solid surface from the SE measurements under the condition in which the optical constants of the samples are known.

5.1.1 Ellipsometric measurements

The linear permittivities of the samples were measured by spectroscopic ellipsometry using a Horiba Spectroscopic ellipsometer. First, we measured the refractive index of a single 16 nm thick Ag film. To avoid the oxidationof Ag layers, we deposited a 40 nm thick layer of SiO_2 on top of the 16 nm Ag. Generally, if the thickness of the thin film is known, ellipsometry can be used to calculate the refractive index as a function of wavelength. If the sample is completely transparent, the refractive index is purely real. However, if the sample has some absorption, the refractive index becomes complex and it could be difficult to calculate the refractive index and thickness simultaneously [67]. In our case, the silver sample is only 16 nm thick, which is thin enough to be transparent. So we have to take into account the precise thickness of the sample. If the thickness of the thin layer is not precisely known, this introduces two additional unknowns into the analysis. For samples with a thickness much greater than the skin depth, the light does not pass through the back interface of the film since the sample is thick enough to be opaque. This will make things simpler because now we only have to take into account the top surface reflections and thus the sample can be considered as infinitely thick. The substrate used for depositing all samples intended for nonlinear characterization is a standard microscopic glass slide. However, ellipsometric measurements using transparent substrates are less accurate compared to those deposited on silicon wafer substrates. So we made some additional samples with the substrate as silicon wafer for ellipsometric analysis.

The permittivity of the 16 nm silver film was fitted to the Drude model. For the capping layer of 40 nm SiO_2, a Lorentz model is used. The permittivity data of silver extracted from ellipsometry is shown in Fig 5.1. A comparison of the ellipsometry data with the simulation is

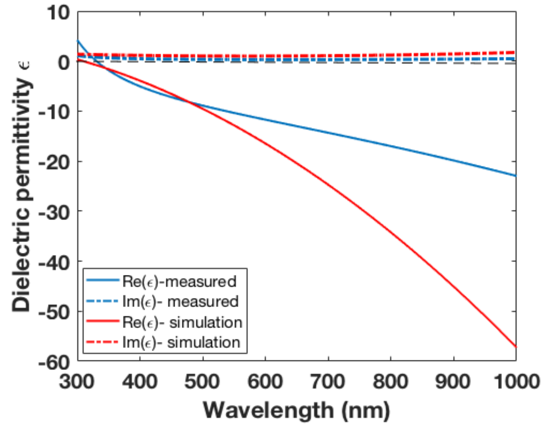

Figure 5.1: Measured permittivity of 16 nm of Ag using the ellipsometer (blue). Simulation using TMM is also plotted (red).

also shown in Fig 5.1. The measured permittivity matches with the permittivity extracted by TMM simulations at smaller wavelengths and shows some discrepancy at the higher wavelength region. This variation in the permittivity values could be attributed in part to varying densities of the Ag films from that of the literature values [50].

Unlike a single Ag film, the data analysis become more complicated when we measure the multilayer sample. Accuracy will be lost as the number of layers increases. Also, the Horiba Spectrometer is a fixed-angle ellipsometer. Variable angle spectroscopic ellipsometry (VASE) performs the above measurement as a function of both wavelength and angle of incidence. Adding multiple angles to spectroscopic capability provides new information because of the different optical path lengths traversed, and it optimizes sensitivity to the unknown parameters. Using a fixed-angle ellipsometer makes it difficult to find the unique solution of an anisotropic sample. VASE is mostly preferred for optically anisotropic samples. In our case, we have overall 10 layers of metals and dielectrics periodically stacked over a glass substrate and the sample is highly anisotropic. All these factors combine to make the analysis of ellipsometric measurements impractical to use as a linear characterization technique. If the model does not adequately represent the true sample structure, then the parameters extracted from the model will not be physically reasonable [68].
In this case, supplemental data such as transmittance or reflectance would be needed to arrive at a unique solution. The measured ellipsometric parameters ψ and Δ are plotted in Fig 5.2 (a) for an incident angle of 70° (which is the default angle in the ellipsometer we used for the measurement), and the extracted permittivity plots are shown in Fig 5.2 (b). The permittivity of the Ag-SiO_2 multilayer sample is modelled using a Drude-Lorentz model with additional anisotropic features. Fig 5.2 (a) shows that the ψ and Δ fit are almost in good agreement with experimental data; however, the dispersion model we obtained from the fit gives unrealistic values like negative values for imaginary permittivity. What this means is that even if a good fit is obtained with sensitivity to all fit parameters, not all the parameters will necessarily have been uniquely determined with physically reasonable values.

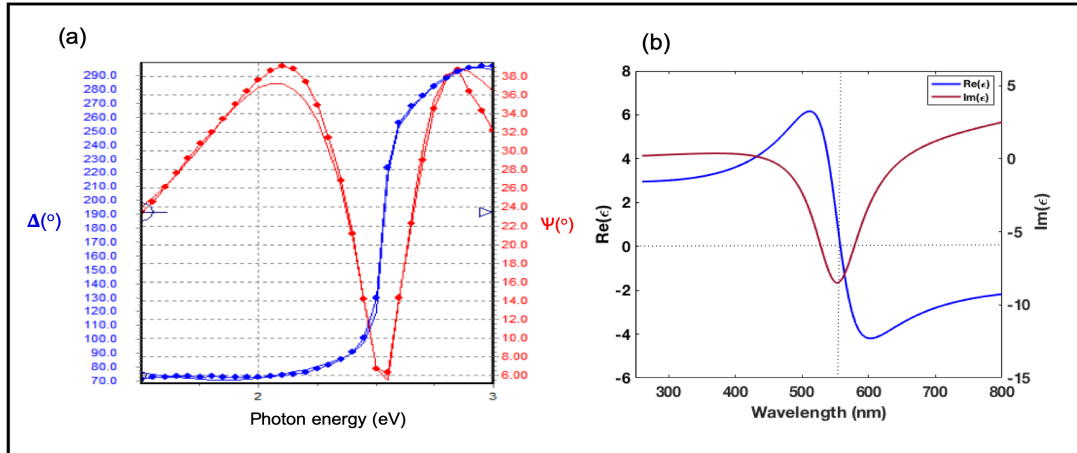

Figure 5.2: (a) The measured ellipsometric parameters ψ and Δ of the Ag-SiO_2 multilayer sample for 70° incident angle as a function of the photon energy. (b) The extracted permittivity of the multilayer sample using a Drude-Lorentz model (these results are unphysical and thus cannot be used).

Fig 5.2 (a) shows that the ψ and Δ fits are agreeing well with the collected data, but Fig 5.2 (b) shows that the derived permittivity from the Drude-Lorentz model shows some unrealistic values like a negative loss. Even though the real part of permittivity crosses zero at 550 nm, it may not be the actual zero-crossing wavelength because the imaginary part is not in agreement with the model. What this means is that even if a good fit is obtained with sensitivity to all fit parameters, not all the parameters will necessarily have been uniquely determined. For isotropic samples with only a few layers, this fixed angle ellipsometry can be a very reliable tool. Metal-dielectric multilayer samples are a complex scenario which can only be modelled using a variable angle spectroscopic ellipsometry. Variable angle spectroscopic ellipsometry has the advantage over fixed angle measurements in that, it acquires large amounts of data and can be optimized for particular film thicknesses or optical parameters. So we ruled out the ellipsometry method as a linear characterization technique for the metal-dielectric stack and hence we turned to a different procedure.

5.1.2 Determination of permittivity of the metal-dielectric stack from transmission measurements

To characterize the linear properties of the metal-dielectric stack we built a simple setup for the measurement of the transmission. A super-continuum source covering the visible-NIR spectrum was collimated with an objective lens, with controlled polarization. The transmitted beam from the sample were then focused on the tip of a multimode fibre and analyzed with a Ocean Optics spectrometer. The measurements were done for various angles of incidence for both polarizations. A reference signal is recorded by collecting the spectra from the super-continuum source without any sample. The normalized transmittance is then calculated by dividing the measured transmittance from the sample by the reference signal. The data were then used to retrieve the effective complex permittivity of the multilayer sample. The experimental transmission spectrum were compared with those calculated with the TMM simulation. The results are shown in the next chapter.

5.2 Nonlinear measurements

5.2.1 Experimental setup

We have explained in section 4.3 about the Z-scan theory and derived the equations used for fitting the Z-scan signals. Now we discuss the experimental setup and the functionalities of the major components in the setup. Fig 5.3 shows the schematic diagram of the complete experiment setup.

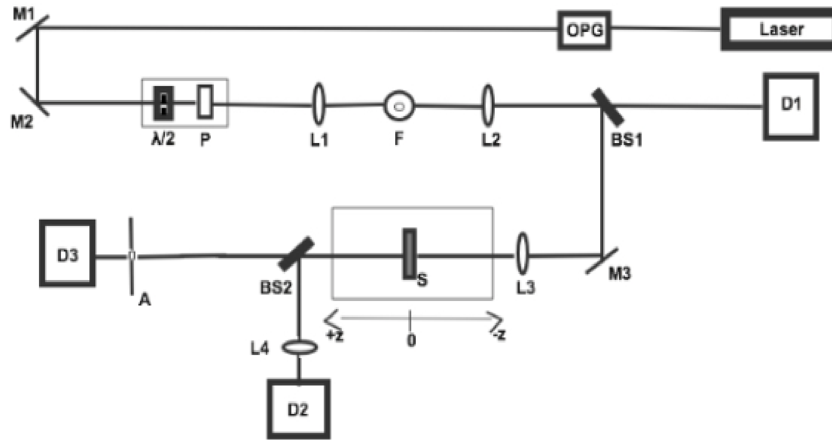

Figure 5.3: Schematic diagram for the Z-scan experimental setup.

The Z-scan measurements were done using laser pulses with a repetition rate of 50 Hz and a pulse duration of 28 ps from an EKSPLA optical parametric generator (OPG). A PL2230 Series picosecond EKSPLA laser is used to provide the 355 nm pump beam for the pulse generation inside the OPG. The pulse from the OPG is first sent through a half-wave plate. Half-wave plates are typically used as polarization rotators. We are using achromatic half-wave plates with AR coatings. The half-wave plate is mounted on a motorized rotation stage so that it can be used as a continuously adjustable polarization rotator. Then the beam passes through a polarizer. Here we are using a Glan Taylor polarizer, that is known for producing extremely pure linear polarization with an extinction ratio greater than 100,000:1. When we use a half-wave plate in conjunction with a polarizer, the combination act as a power controller for the total setup. The theory of the operation is based on Malus law [69]. The intensity of the linearly polarized light passes through a polarizer given by

$$I = I_0 \cos(2\theta), \tag{5.1}$$

where I_0 is the input intensity and θ is the angle between the direction of polarization and the axis of the polarizer. Since the half-wave plate is mounted on a rotation stage, it enables the continuous rotation of the polarization direction of the linearly polarized light. If we are rotating the half-wave plate by an angle ϕ, the polarization will rotate by an angle 2ϕ, where ϕ is known as the azimuth of the half-wave plate. By a 45° rotation, we can achieve a complete attenuation range.

Next, the beam is spatially filtered using a lens-pinhole combination. Spatial filtering, also known as mode cleaning, is an important part of the laser experiments that rely on Gaussian optics. As the name suggests, it is used to clean up the beam. The necessity of this arises

from the fact that lasers will not produce pure Gaussian beams as output all the time. The spatial filter part consists of a lens or a microscopic objective and a pinhole aperture with a positioning mechanism with precision in x-, y-, and z-axes. A pinhole is placed at the focal point of the lens after careful calculation of the beam spot size and the pinhole aperture size. The precise adjustments can be done using a positioning mechanism along with the pinhole. Now the "unclean" (multimode) Gaussian beam passes through the filtering part and only the central maximum of diffraction pattern will come out on the other side. Thus the unwanted multiple order energy peaks, the scattered light produced either by dust or other imperfections on the optical components, will all get removed and we will get a beam without any spatial distortion.

In the next step, this spatially filtered Gaussian beam is focused on the sample by a lens. Here we used a diffraction-limited, high precision aspheric lens of focal length 100 mm. This provides us with diffraction-limited performance for on-axis beam focusing and collimation. The spot size of the focused beam and Rayleigh range is calculated and made sure that the sample is satisfying the thin-film approximation as per our theory ($L < z_0$).

The most important part of the Z-scan setup is the translation stage. The sample is translated along the z-direction (optical axis) across the focal point. We used a 25 mm automated translation stage to serve this purpose. By using an automated translation stage, the sample movement can be done with precision and we can eliminate the conventional problems such as misalignment and vibrations while moving the sample. After the translation stage, we used a beam splitter to split the beam into two. The reflected beam from beam splitter is sent to the open-aperture detector and transmitted beam is sent to the closed-aperture detector, respectively. The beam splitters we used in this experiment are Pellicle beamsplitters which are especially good for minimizing chromatic dispersion and good at eliminating ghosting. A lens is placed before the open-aperture detector to collect all the transmitted light from the sample to measure the nonlinear absorption and a pinhole is placed in front of the closed-aperture detector to collect only the central part of the beam in order to obtain the small distortions in the beam and thereby calculating nonlinear refraction. Positioning the aperture for the closed-aperture signal is very important because the measurements are very sensitive. So we placed the aperture in a two-axis stage mount with the possibility of precise x and y movement.

There is a third detector we used to collect the reference beam before the sample. We normalized our open- and closed-aperture Z-scan signals by dividing them with the reference signal. This will reduce the impact of inbuilt power fluctuations of the laser. So this allows us to get a comparatively noise-free Z-scan signal. We also performed a signal averaging in all the three detectors to reduce the noise factor. We implemented this by iterating every single measurement over 100 times and averaged them to get a signal with reduced noise. The lowest bound of our tunable laser is 410 nm and when approaching the lower wavelength limit, large power fluctuations are observed, necessitating these measurements.

5.2.2 Beam profile

In most laser applications, it is necessary to understand the beam profile and propagation characteristics of the laser beam. Most lasers can be made to operate on its fundamental transverse mode (TEM00 mode) with a Gaussian profile. When refracted by a lens, the Gaussian beam is transformed into another Gaussian beam(parameters will change). The reason is that the Fourier transform of the Gaussian electric field distribution is again Fourier. This implies that along the propagation path, the Gaussian source distribution will remain unchanged and makes it easy to picture the electric field distribution at any point of propagation length. The electric

field distribution is given by

$$E_s = E_0 \exp\left(-\frac{r^2}{w^2}\right) \quad , \tag{5.2}$$

where is the radial coordinate and w is the beam radius. Because of this self-Fourier transform

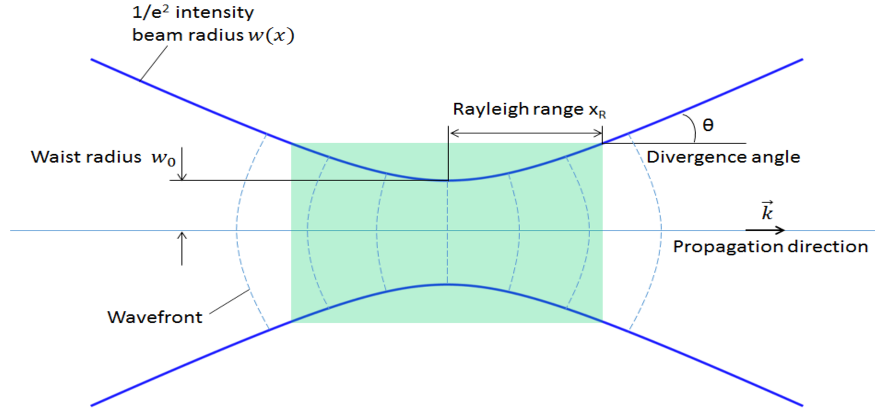

Figure 5.4: Propagation of the Gaussian beam

characteristic of the Gaussian beam, the transverse distribution of the intensity remains Gaussian at every point along the propagation length and only the radius of the Gaussian beam and the radius of curvature R(z) of the wavefront change during the propagation. At a position z along the beam (measured from the focus), the spot size parameter w is given by

$$w(z) = w_0\sqrt{1 + \left(\frac{z}{z_0}\right)^2} \tag{5.3}$$

where w_0 is the beam waist and z_0 is the Rayleigh range given by $z_0 = \frac{\pi w_o^2}{\lambda}$.

The Z-scan theory is based on the assumption that the incident beam is Gaussian (TEM00). Because of the lowest-order self-consistent field distribution of the Gaussian beam, chances of beam distortions caused by the intra-cavity elements are very small. Therefore, the output beam profile of many lasers are Gaussian. However, this is not always the case. Sometimes, the diffraction effects in the laser resonator cavity induces a change in the beam mode as it propagates outside the laser resulting in a non-Gaussian beam profile. So, it is critical to analyze the output beam from the laser. Our beam profile is visualized using a Gentec beam profiling camera. The picosecond laser pulse used in our experiment is shown in Fig 5.5 (a), which is clearly a non-Gaussian beam. This exemplified the need for a method to improve the beam quality, to produce a Gaussian beam. We adopted a spatial filtering technique to polish the beam profile. The spatial filter set-up consists of a lens and a pinhole aperture attached to a positioning mechanism. The positioning mechanism has a precision X-Y-Z movements that allows us to precisely centre the pinhole at the focal point of the lens. The spatial filter removes the higher order spatial modes coexist inside the laser pulse. Since different modes have different spot sizes at the focus and the desired TEM00 Gaussian mode has the smallest spot size at the focus, only this mode gets through through the pinhole, while all other modes are blocked. In simple words, only the maximum of the diffraction pattern pass through the pinhole removing all the higher order peaks. For getting the optimal results, we need to wisely choose the perfect

combination of pinhole and lens. The pinhole we are using is a diamond aperture of 75 μm diameter and the lens has a focal length of 100 mm. Fig 5.5 (b) shows the laser beam profile after the spatial filter, demonstrating the importance of spatial filtering in laser experiments.

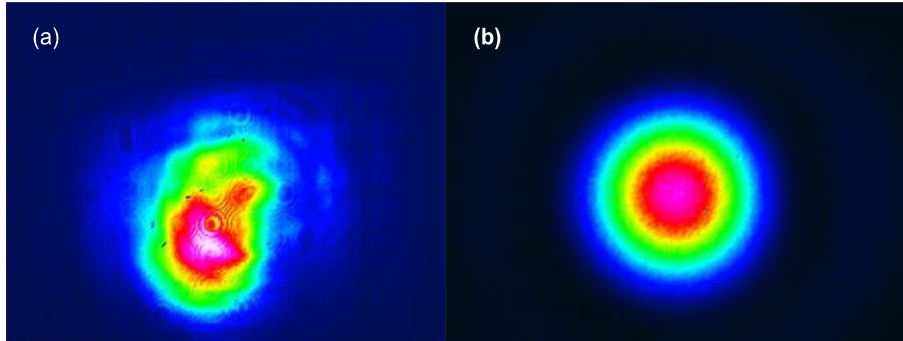

Figure 5.5: Intensity profile of the beam (a) before spatial filter (b) after spatial filter. A nearly Gaussian beam is obtained after the spatial filtering.

The beam profile for the entire focal plane is measured as a function of z position. Fig (5.6) shows the visual representation of Eq (5.3) using the beam profiling camera. As we can see in figure, at the focal point, beam size is the smallest and the intensity is maximum.

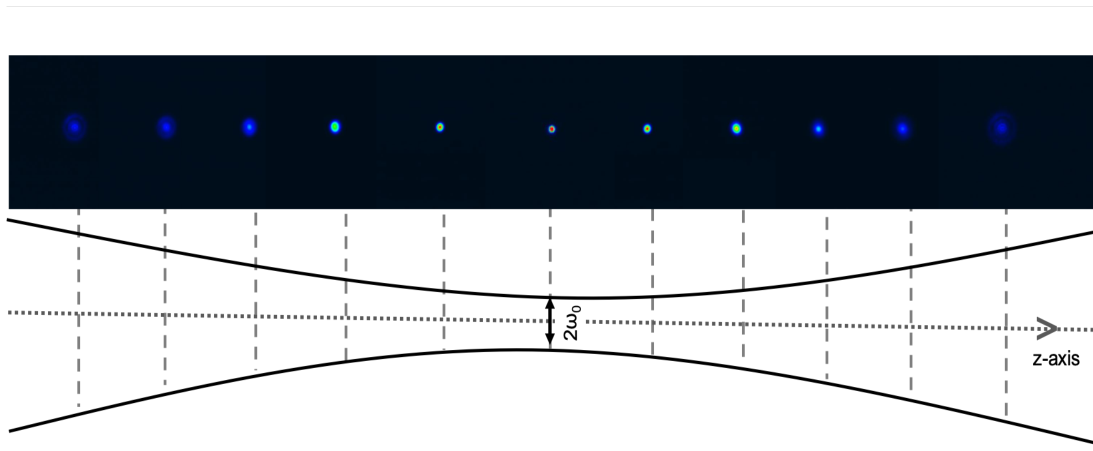

Figure 5.6: Beam propagation as a function of z position.

Beam ellipticity is another parameter which is of great importance in the Z-scan measurements. The various beam shapes are described by an ellipticity parameter e, which is defined as the ratio of the semimajor axis to the semiminor axes (or vertical diameter to horizontal diameter of the Gaussian beam). Large ellipticity values of the beam can badly affect the signal shape in Z-scan measurements. Wicksted *et* al [70] studied the effects of beam ellipticity on Z-scan measurements and noticed that with an increase in ellipticity, both the peak and valley reduce from their symmetric maxima and minima that were attained in the circular limit ($e = 1$). It can also lead to an additional peak and valley in the signal. Fig 5.8 shows an example of a Z-scan signal with $e = 5.5$ [70]. A Z-scan signal with $e = 1$ is shown in the inset for comparison.

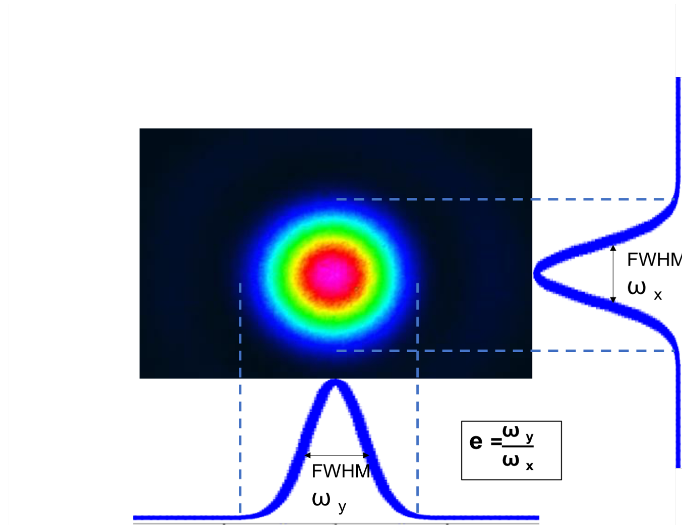

Figure 5.7: Ellipticity measurement of the Gaussian beam.

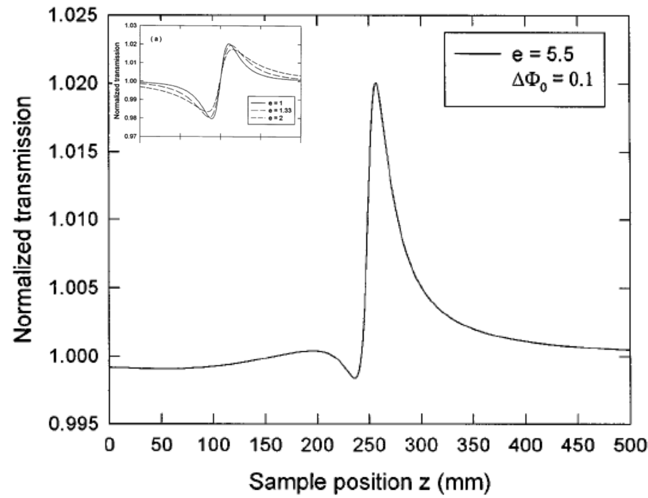

Figure 5.8: Closed-aperture Z-scan signal of a beam with an ellipticity $e = 5.5$. Beam with ellipticity close to 1 is shown in the inset for comparison [70].

The beam ellipticity is measured at different positions along the propagation length. For some measurements the e parameter is high and that can happen due to many reasons. One among the reasons is that if the laser beam is not passing through the centre of the lens, it can make the beam elliptical. So the idea is to measure the beam ellipticity at every point and based on how much it is deviating from the circular case, we can realign the system till we get a reasonable e parameter. Fig (5.9) shows the vertical and horizontal beam profile with different ellipticity values.

Fig 5.9 (a) shows the input beam profile of the beam and (b) and (c) shows the Gaussian fit

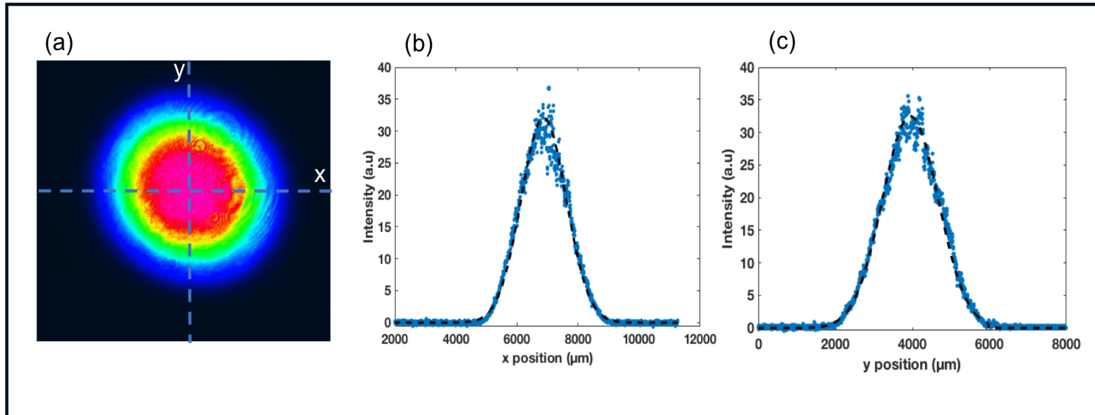

Figure 5.9: Input beam profile measured at 520 nm before the focussing lens. Gaussian fit of the experimental beam profile in the (b) x direction, (c) y direction.

of the experimental beam profile. In the x-direction, the gaussian fit to the experimental beam profile is 90.15% and in the y-direction it is 91.98%. The $1/e^2$ diameter of the input beam is 2959 μm in the x-direction and 2909 μm in the y-direction, which gives an ellipticity of 1.01. We measured the beam parameters for all the operating wavelengths and given in table (5.1). The

focussed spot size is related to the intensity of the beam by the relation,

$$I_0 = \frac{P}{\pi w_0^2}, \tag{5.4}$$

where w_0 is the focussed spot diameter ($1/e^2$). This square dependence of w_0 to I_0 indicates that, a small error in the value of beam parameter measurement affects the peak intensity value greatly. This will approximately produce an uncertainty of 10% in the final value of n_2 and β.

5.2.3 Calibration of the Z-scan experimental setup

After building an experimental setup, we should evaluate the functioning of the components of the setup. By doing so, we can determine how these components will affect the overall quality of the measurements. So the first thing we need to do once the setup is build is to calibrate it with a known material. Carbon disulfide (CS_2) is widely used as a reference standard for nonlinear measurements [71]. The nonlinear response in CS_2 can be attributed to the intramolecular interactions, the orientational Kerr effect and the electronic Kerr effect. All these processes results in a change in the refractive index of CS_2. The response time of the orientational Kerr effect is 1.5 ps and other two processes are 200 fs. Our experiments are mainly performed using picosecond pulses and for such short laser pulses, the Kerr nonlinearities seem to dominate. In certain cases, the thermal lens effect also contributes to the nonlinear refraction. There are two main reasons for the thermal lens effect. One is due to the propagation of the acoustic wave, which is produced as a result of the absorption of radiation in the medium. The other is due to the change in the medium density that can occur as a result of the accumulation of thermal energy in the absorbing region [72]. Numerous nonlinear measurements were performed on CS_2. The values reported for nonlinear refractive index is in the order 10^{-5} cm^2/GW [73, 74]. Other studies were also done to find the dependence of the nonlinear refractive index on the pulse

Beam parameters			
Wavelength (nm)	**Input beam diameter-** $1/e^2$ (μm)	**Focused spot diameter-** $1/e^2$ (μm)	**Focused spot diameter -FWHM** (μm)
410	2417	21.59	18.36
420	2425	22.05	18.74
430	2444	22.40	19.04
440	2527	22.17	18.84
450	2587	22.15	18.82
460	2598	22.54	19.16
470	2648	22.59	19.21
480	2752	22.21	18.87
490	2793	22.34	18.98
500	2857	22.28	18.94
510	2981	21.78	18.51
520	2934	22.56	19.18
530	3058	22.07	18.75
540	3170	21.69	18.43
550	3239	21.62	18.38
560	3382	21.08	17.92
570	3400	20.97	17.82

Table 5.1: Beam parameters

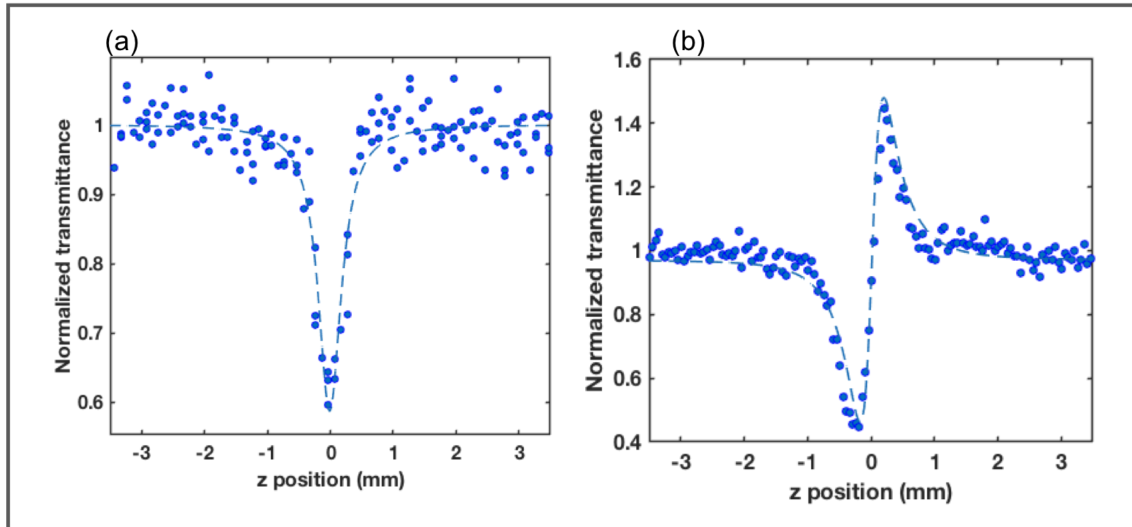

Figure 5.10: The open-aperture (a) and closed-aperture (b) Z-scan signal of CS_2. The dashed line represents a theoretical fit to the experimental points.

duration. We performed the Z-scan measurement of CS_2 in order to calibrate our experimental setup using a 28 picosecond pulse with a repetition rate of 50 Hz. We presume a nearly Gaussian spatial distribution for the measurements. The operating wavelength was 600 nm. The beam waist radius w_0 (FWHM) was 8.1 μm and intensity of the beam at the focus was 5.4 GW/cm^2. All measurements on CS_2 (Sigma-Aldrich, 270660, 99.9%) were conducted using 0.05 mm path length, UV quartz cuvettes. The open-aperture and closed-aperture signals were collected. The pulse width of the beam used in all our measurements was 28 picosecond. Fig 5.10 (a) and (b) and are the open- and closed-aperture Z-scan signals of CS_2, respectively. The measured values of the refractive index n_2 is 9.2 $\times 10^{-4}$cm^2/GW and the nonlinear absorption coefficient β is 43.47 cm/GW with an uncertainty of 35% in both measurements. The source of uncertainty is the power fluctuations that occurred in the laser signal.

Having established methods for characterizing the linear and nonlinear optical response of the samples experimentally, we next proceed with the characterization of our multilayer metal-dielectric stack with the zero-crossing at our designated wavelength.

Chapter 6

Measurements and interpretations of the linear and nonlinear optical response of the Ag-SiO_2 multilayer stack

In this chapter, we present the results of the experiments we described in chapter 5 and we present a discussion of these results by applying the analysis described in chapters 2, 3, and 4. We also discuss briefly the scientific impact of these results from the perspective of the motivations of this research work.

6.1 Transmission measurements of the Ag-SiO_2 multilayer stack

The linear response of the Ag-SiO_2 multilayer stack is characterized by the transmission measurement. In this section, we demonstrate that the traditional procedure of obtaining material parameters from transmission or reflection data can be successfully applied to metamaterials.

A super-continuum laser was used as the source, and the transmission spectrum was collected using an Ocean Optics spectrometer. The measured transmission spectrum of the sample was normalized to that obtained from the super-continuum source without the sample. Fig 6.1 shows the transmission spectra of the Ag-SiO_2 multilayer stack taken at different angles of incidence for p polarization. The transmission curves shift towards shorter wavelength as the angle of incidence increases. In the inset to Fig 6.1, we also show the zoomed-in view of the region around 450 nm. We compared the measured transmission spectra to those expected from the TMM simulations for several thicknesses of metal and dielectric layers in the stack. We found that for a metal-dielectric multilayer stack with thickness of 16 nm of silver and 56 nm of SiO_2 the TMM simulations are consistent with the experimental data as shown in Fig 6.1. In the next step, we analyzed the reflection and transmission calculated from the TMM simulations for this metal-dielectric multilayer stack of 16 nm of silver and 56 nm of SiO_2 to determine the effective permittivity.

The permittivity extracted using the transmission data is shown in Fig 6.2. The zero-crossing wavelength occurs at 484 nm, which is close to the predicted zero-crossing wavelength in our de-

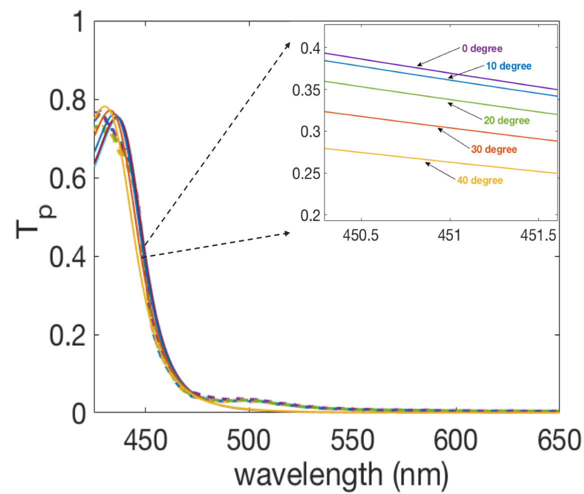

Figure 6.1: Transmission spectra of the Ag-SiO_2 multilayer stack . The inset shows a zoomed-in view of the simulation spectra around 450 nm. The solid lines are taken from the TMM simulation data and the dashed lines are the measurements. Colours represent different angles of incidence.

vice design (509 nm). The 5% deviation is likely due to experimental errors during measurement. The cause of the sharp peak in permittivity near 460 nm is not immediately understood, but we believe it will not affect our results since it is removed from the zero-crossing wavelength.

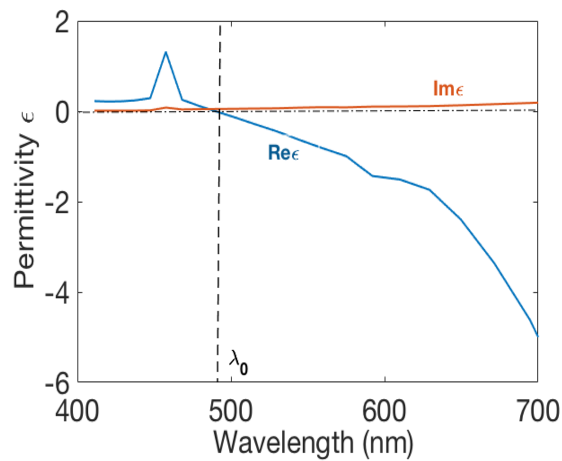

Figure 6.2: Dielectric permittivity of Ag-SiO_2 multilayer stack calculated using the transmission and reflection data.

6.2 Nonlinear optical properties of the Ag-SiO_2 multilayer stack

The nonlinear optical properties of the Ag-SiO_2 multilayer stack were investigated by a Z-scan technique using picosecond laser pulses with tunable wavelength. Both open- and closed-aperture measurements were performed in the spectral range from 410 nm to 580 nm, including the ENZ regime of the metamaterial's dispersion. Similar Z-scan measurements were performed under the same conditions for a 16 nm thick Ag single layer for comparison. The open- and closed-aperture signals were normalized by dividing the signal measured by a reference detector. The reference detector was used to compensate for the fluctuations that occurred in the laser signal.

In the open-aperture measurement, shown in Fig 6.3 (a), all the transmitted intensity through the sample was collected. This gives an unambiguous measurement of the nonlinear absorption. The variations in the transmission are strongest at the focus and smallest away from it. A positive peak-shaped dependence as seen in Fig 6.3 (a) corresponds to a negative value of β (saturable absorption). In the closed-aperture measurement ((6.3) (b)), only a small part of the intensity ($\approx$ 10%) transmitted through the sample was collected. Thus, variations in the transmission correspond to both nonlinear absorption and nonlinear refraction. Therefore, the closed-aperture signal depends also upon the open-aperture results. The dependence solely on nonlinear refraction can be obtained by dividing the close aperture curve with the open-aperture curve as seen in Fig (6.3) (c). The curves in Fig (6.3) (b) and (c) correspond to a positive value of the nonlinear refractive index (focusing nonlinearity). However, this method for finding the purely refractive effect by the division of closed-aperture signal by open-aperture signal results in an uncertainty of 10% [64]. Apart from the uncertainty of this method, this division approach will not work for samples with large nonlinear absorption. As we can see from Fig 6.3 (b), the shape of the closed-aperture signal is similar in shape to the open-aperture signal. For a beam with small ellipticity and waist separation the area decreases, reaches its minimum, and then increases parabolically in a symmetric manner as a function of sample position z. This severe asymmetry in the closed-aperture signal is due to the large change in the absorption and thus it differs from the normally symmetric closed-aperture Z-scan curve . So, it is evident that the sample has large nonlinear absorption and hence division process will result in larger uncertainty. We first extracted the imaginary part of the nonlinear phase shift Ψ from the open-aperture measurement. We used this value of $\Delta\Psi$ from the open-aperture data to find the real part of the phase shift $\Delta\Phi$ from the closed-aperture data. The extracted values of the nonlinear phase shift were used in the standard expression to calculate n_2 and β. Assuming a beam with a Gaussian spatial profile, the transmission in the case of open aperture is given by [64]

$$T_{\mathrm{OA}} = 1 - \frac{\Delta\Psi}{1 + (z/z_0)^2}, \tag{6.1}$$

where z_0 is the Rayleigh range and $\Delta\Psi$ is defined as the imaginary part of nonlinear phase shift given by

$$\Delta\Psi = \frac{\beta I_0 L_{\mathrm{eff}}}{2\sqrt{2}}, \tag{6.2}$$

where β is the nonlinear absorption coefficient, I_0 is the peak intensity and L_{eff} is the effective sample thickness. In the case of closed-aperture, the transmission after the aperture is given by [75]

$$T_{\mathrm{CA}} = 1 + \frac{4(z/z_0)\Delta\Phi}{(1 + (z/z_0)^2)(9 + (z/z_0)^2)} - \frac{2((z/z_0)^2 + 3)\Delta\Psi}{(1 + (z/z_0)^2)(9 + (z/z_0)^2)}, \tag{6.3}$$

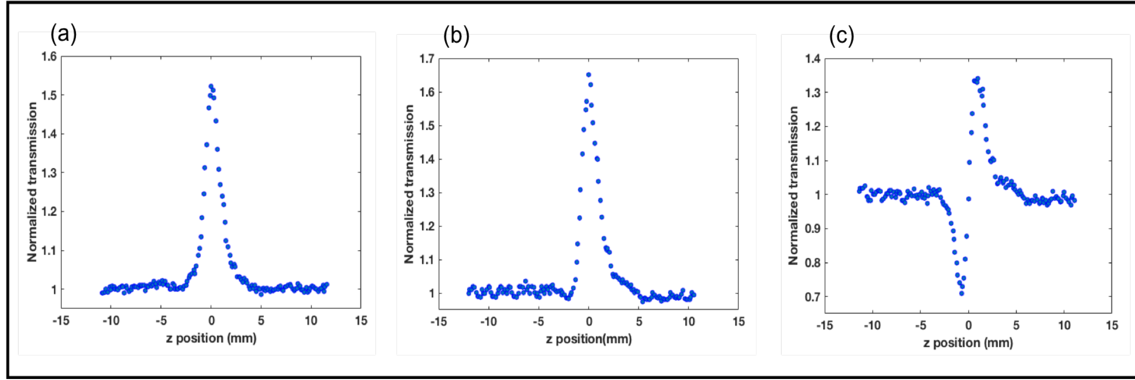

Figure 6.3: Z-scan signal of the Ag-SiO_2 multilayer stack at the ENZ wavelength. (a) the open-aperture signal, (b) the closed-aperture signal, (c) division of the closed-aperture signal by the open-aperture signal.

where $\Delta\Phi$ is defined as the real part of nonlinear phase shift given by

$$\Delta\Phi = (1-S)^{0.25} k n_2 I_0 L_{\text{eff}}, \tag{6.4}$$

where $k = 2\pi/\lambda$, n_2 is the nonlinear refractive index, and S is the transmission through the aperture given by $S = 1 - \exp \frac{-2r_a^2}{w_a^2}$, with r_a is the radius of the aperture and w_a is the radius of the beam at the aperture. The beam radius at the aperture is 6 mm and aperture radius is 0.5 mm. This gives a value of $S = 0.003$. The term $(1-S)^{0.25}$ in equation (6.4) becomes 0.999 ≈ 1. Fig 6.4 shows representative closed and open-aperture signals near the ENZ wavelength (500 nm). The β calculated from Fig 6.4 (a) is 1.81×10^5 and n_2 from Fig 6.4 (b) is 1.41. This calculated value of n_2 is 10^7 times larger than the n_2 of fused silica ($3.2 \times 10^{-7}\text{cm}^2/\text{GW}$).

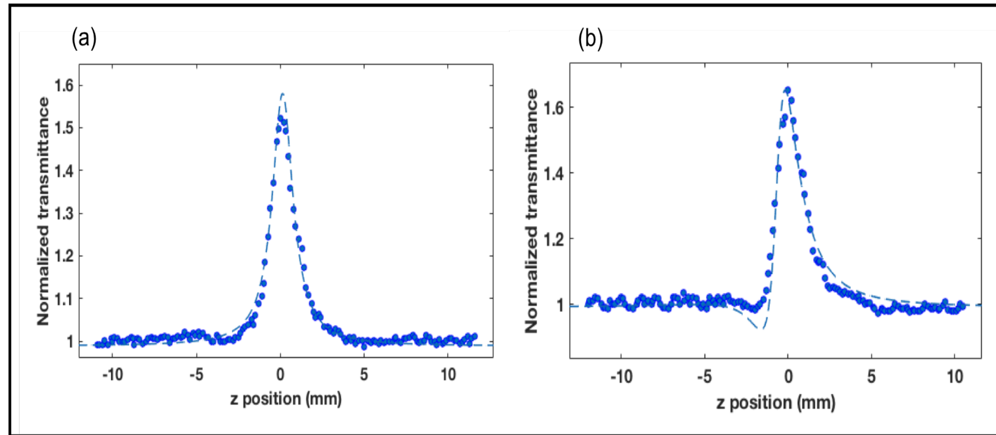

Figure 6.4: A theoretical fit (dotted lines) to the Z-scan signal of the Ag-SiO_2 multilayer stack at the ENZ wavelength using equations (6.1) and (6.3). (a) The open-aperture signal and (b) the closed-aperture signal.

The main source of uncertainty in the value of n_2 is the absolute measurement of the irra-

diance. A plot of nonlinear phase shift $\Delta\Phi$ versus peak laser irradiance I_0 as measured from various Z-scans on the same sample at the same wavelength is shown in Fig (6.5). The nonlinear phase-shift increases linearly with the irradiance on the sample as per equation (6.4). This in turn can also be used to find the damage threshold of the sample. The slope of the linear fit gives the nonlinear refractive index. From Fig (6.5), we calculated the slope of the linear fit m equal to 0.006 and the nonlinear refractive index n_2 is determined using the equation $m = k * n_2 * L_{\text{eff}}$ and found to be 1.3 cm^2/MW at 500 nm. The experimental data is represented by the circle points with each point has an error bar. The error bars have been evaluated by calculating the standard error over 3 measurements.

A deviation from the linear behaviour could be the result of either higher-order nonlinearities or the laser damage of the sample. In most cases, the laser damage to the sample can be visually determined. In this experiment, we determined that the sample undergoes laser damage if the intensity goes above 300 MW/cm^2. So for all the experimental measurements, we set the intensity of the laser beam below 300 MW/cm^2 to avoid the laser-induced damage.

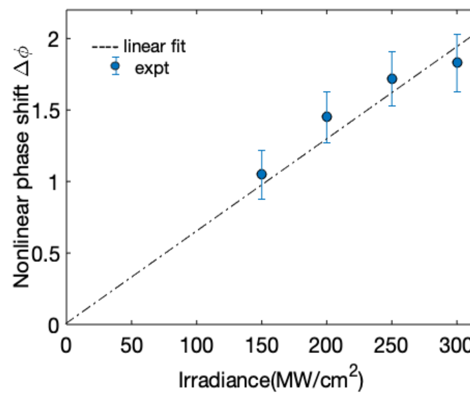

Figure 6.5: Nonlinear phase shift $\Delta\Phi$ of the Ag-SiO_2 multilayer stack as a function of the peak irradiance at 500 nm. The dashed line is a linear fit to the experimental data passing through the origin.

Fig (6.6) shows the closed-aperture Z-scan signal measured at different wavelengths at and away from the ENZ region. As we can see from Fig 6.6 (a), at shorter wavelength, the closed aperture Z-scan signal is symmetric with respect to the focus (i.e, at $z = 0$). As we moves to higher wavelength region, the closed-aperture signal differs entirely from those obtained at lower wavelength region and they are asymmetric. This happens as a result of the large change in the absorption at higher wavelengths. With increase in absorption, the valley of the transmittance is severely suppressed and the peak is greatly enhanced, as shown in Fig 6.6 (b) and (c). The larger distortions in the Z-scan signals in the smaller wavelength region is because of fluctuations in the OPG output in the lower wavelength limit.

Another interesting thing we noted is the switching in the sign of the nonlinear absorption as a function of wavelength. The change from reverse saturable absorption (RSA) to saturable absorption (SA) is observed between 445 nm and 450 nm. This is shown in Fig 6.7. Below 450 nm RSA is observed and above 450 nm SA is observed. The physical mechanism behind these processes is still to be fully investigated.

The change in nonlinear transmittance as a function of the incidence angle is shown in Fig (6.8). As we can see from the figure, the transmission goes down as we increase the angle of

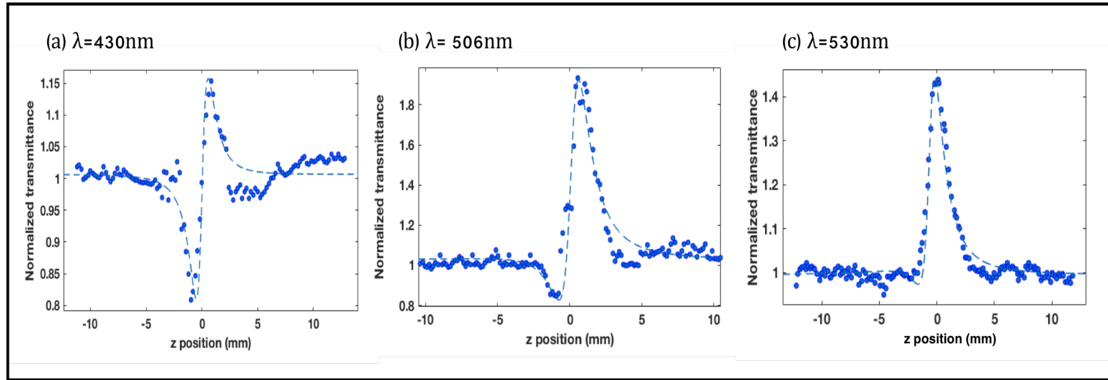

Figure 6.6: The closed-aperture signal of the Ag-SiO_2 multilayer stack at different wavelengths (a) at 430 nm (away from the ENZ wavelength towards the blue side of the spectrum), (b) at 506 nm(the ENZ wavelength) and (c) at 530 nm (away from the ENZ wavelength towards the red side of the spectrum)

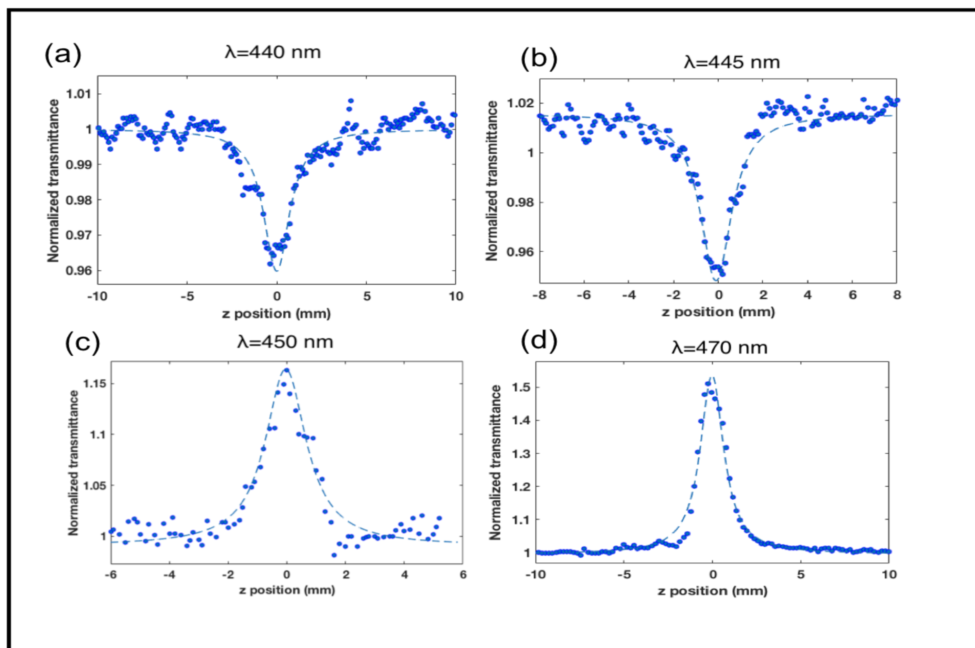

Figure 6.7: The open-aperture signal of the Ag-SiO_2 multilayer stack showing a transition from reverse-saturable absorption (RSA) to saturable absorption (SA) as a function of excitation wavelength. (a) and (b) shows RSA and (c) and (d) shows SA.

incidence. This is presumably is a result of the increase in Fresnel reflection for oblique angles of incidence, which reduces the intensity of light coupling into the stack and experiencing a reduced nonlinear response. To confirm this we calculated the Fresnel transmission coefficient for difference incident angles and plotted them against the peak height of nonlinear transmittance in Fig 6.8. We used the linear refractive index n_0 extracted from transfer matrix method to calculate

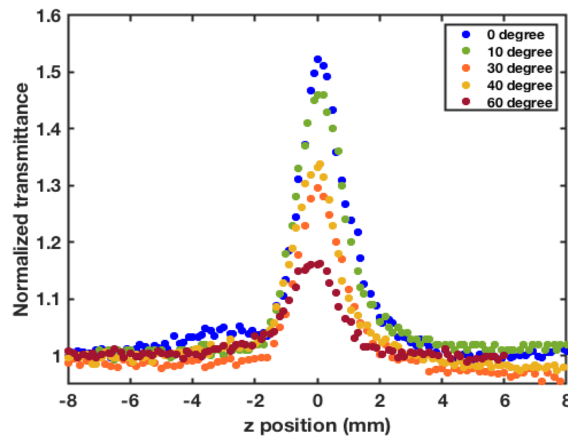

Figure 6.8: The nonlinear transmittance of the Ag-SiO_2 multilayer stack as a function of angle of incidence measured at 500 nm. Colours represent different angles of incidence.

the Fresnel coefficients. The peak height and the Fresnel transmission coefficients show a linear dependence. The peak height of nonlinear transmittance reduces with decrease in transmission coefficient or increase in reflection coefficient. This justifies our assumption that the reduction in nonlinear transmittance may due to the Fresnel losses at oblique angles of incidences. This is depicted in Fig 6.9.

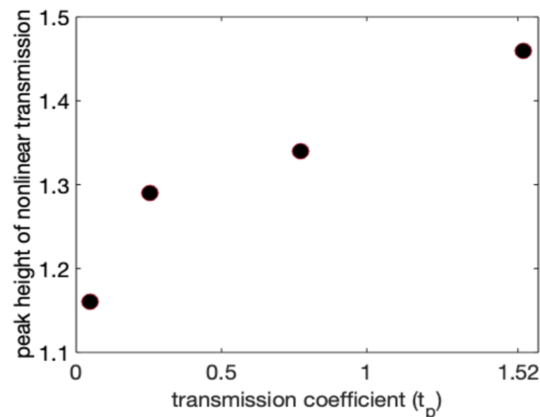

Figure 6.9: The peak height of the nonlinear transmission for different angles of incidence as a function of the Fresnel transmission coefficient. This explains the behaviour seen in Fig (6.8) and is presumably is a result of the Fresnel losses for oblique angles of incidence.

Comparison of nonlinearity of bulk Ag with Ag-SiO_2 multilayer stack

Metals are known to possess a fast, extremely large, nonlinear optical response. Noble metal nanoparticles possess closely spaced energy bands which allow conduction electrons to move almost freely. When excited with light, the oscillation of the free electrons in the s–p conduction

band gives rise to surface plasmon resonance. These surface plasmon resonances can lead to the enhancement of the third-order susceptibility when they are pumped by lasers operating at the UV-visible-infrared range [76, 77]. The third-order susceptibility of the noble metals is almost 10^6 times larger than that of fused silica, with relaxation times in the subpicosecond range [1]. Fig 6.10 shows the open- and the closed-aperture Z-scan signal of a bulk silver film of thickness 16 nm. A thin layer of SiO_2 is deposited on top of the silver layer to its prevent oxidation. (The thickness of SiO_2 is 40 nm, and thus the contribution of nonlinearity from the deposited SiO_2 layer is persumed negligible). The comparison of normalized transmittance from a bulk

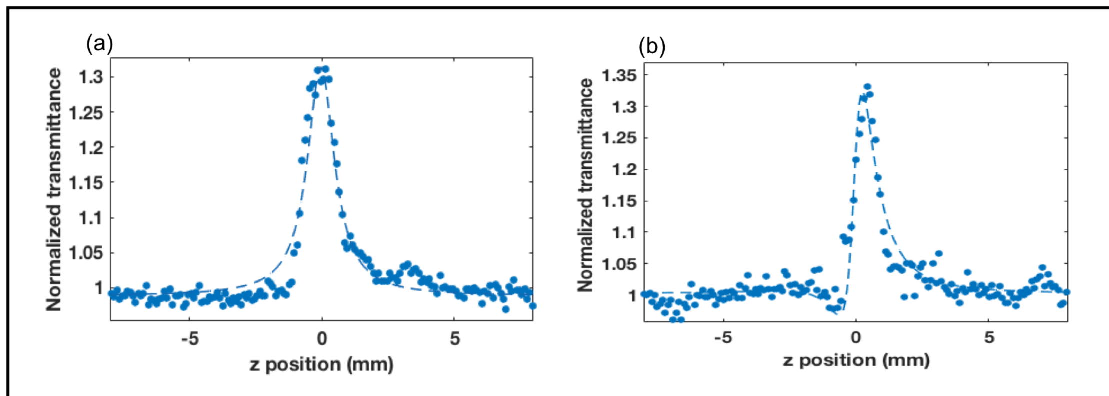

Figure 6.10: Z-scan traces showing the normalized transmission of the bulk silver sample at 500 nm (a) open-aperture signal (b) closed-aperture signal. The intensity at the focus was 500 MW/cm^2. The dashed lines represent a theoretical fit.

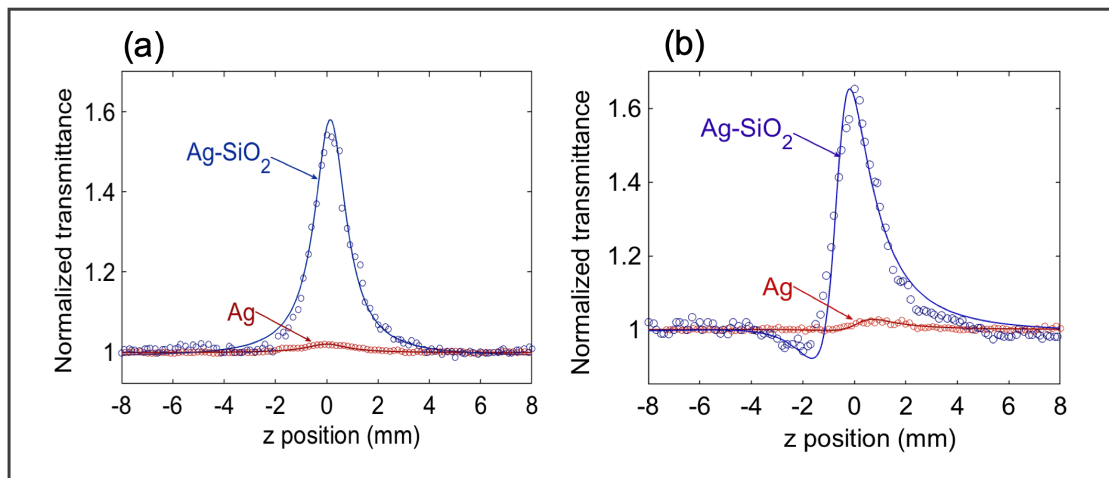

Figure 6.11: (a) The open aperture and (b) the closed aperture Z-scan traces showing the normalized transmission of the bulk Ag and the Ag-SiO_2 multilayer stack at 500 nm. The intensity at the focus was 200 MW/cm^2. The solid lines represent a theoretical fit.

Ag (16 nm) and a Ag-SiO_2 sample at 500 nm is shown in the Fig 6.11. At 500 nm (the ENZ regime), the nonlinear response of the bulk silver film is much smaller than that the Ag-SiO_2

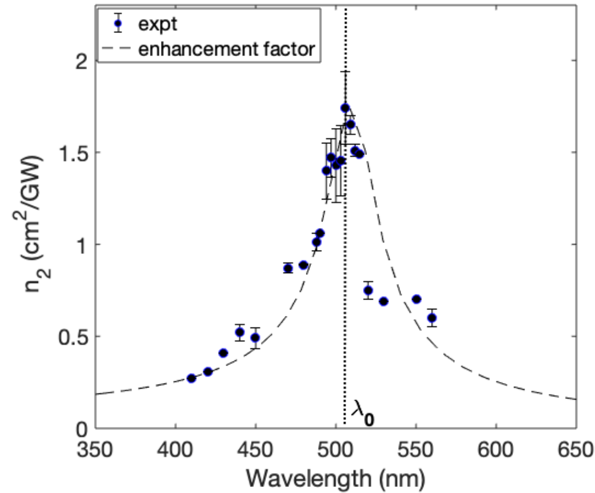

Figure 6.12: The nonlinear refractive index n_2 of the Ag-SiO_2 multilayer stack as a function of wavelength. Note the strong enhancement of n_2 at the ENZ wavelength λ_0. The dashed line represents the enhancement factor calculated using equation (2.50). The error bars indicate the deviations of the nonlinear refractive indices caused by the power fluctuations of the laser, evaluated as the standard error over 3 measurements.

multilayer stack. The nonlinear refractive index n_2 and absorption coefficient β extracted from the Z-scan signal are 0.07 cm^2/GW and -6844 cm/GW respectively. The n_2 of the Ag-SiO_2 multilayer stack is approximately 20 times larger than the n_2 of the bulk Ag sample. The source of optical nonlinearity in noble metals is normally due to the Fermi smearing mechanism [78]. By comparing the multilayer sample and the bulk metal sample containing 16 nm thickness of silver, an enhancement in the nonlinearity is observed as shown in Fig (6.11).

The nonlinear refractive index n_2 and nonlinear absorption coefficient β extracted from the open-aperture and closed-aperture Z-scan signals for various wavelengths are tabulated in table (6.1). The largest value of n_2 and β is observed at 506 nm. This is approximately 7 times larger than the n_2 value observed away from the ENZ wavelength.

The variation of the nonlinear refractive index n_2 as a function of wavelength is shown in Fig 6.12. The experimental data is represented by the circle points with each point has an error bar. The error bars have been evaluated as the standard error over 3 measurements. The Ag-SiO_2 multilayer stack clearly shows a large enhancement of the nonlinear Kerr index close to the ENZ wavelength. An enhancement factor is also plotted in the same figure using the equation (2.50). The linear refractive index n_0 value used here is the one we calculated using TMM simulations and $\chi^{(3)}$ value is assumed to be a constant across the spectrum. The experimental plot is in good agreement with the theoretical results. The variation of the nonlinear absorption constant β is shown in Fig 6.13. The experimental data is represented by the circle points with each point has an error bar. The error bars represent the experimental uncertainty mainly caused by the power fluctuations in laser. The error bars have been evaluated as the standard error over 3 measurements. The presence of an ENZ wavelength significantly modifies the behaviour of the

Nonlinear coefficients		
Wavelength (nm)	$n_2(cm^2/GW)$	$\beta(cm/GW)$
410	0.27	5.59×10^3
420	0.31	1.04×10^4
430	0.41	9.9×10^3
440	0.52 ±0.05	$-(3.4 \pm 0.1) \times 10^4$
450	0.49 ±0.06	$-(3.3 \pm 0.1) \times 10^4$
470	0.87 ±0.03	$-(1.06 \pm 0.02) \times 10^5$
480	0.899 ±0.002	$-(1.15 \pm 0.03) \times 10^5$
488	1.01 ±0.05	$-(1.66 \pm 0.09) \times 10^5$
490	1.06	$-(1.81 \times 10^5$
494	1.4 ±0.1	$-(1.5 \pm 0.2) \times 10^5$
497	1.5 ±0.1	$-(1.6 \pm 0.1) \times 10^5$
500	1.4 ±0.1	$-(1.9 \pm 0.1) \times 10^5$
503	1.4 ±0.2	$-(2.18 \pm .09) \times 10^5$
506	1.7 ±0.2	$-(2.3 \pm 0.2) \times 10^5$
509	1.65 ±0.05	$-(1.66 \pm 0.02) \times 10^5$
512	1.51 ±0.03	$-(1.23 \pm 0.02) \times 10^5$
515	1.49	-1.45×10^5
520	0.75 ±0.05	-1.2×10^5
530	0.69	-1.16×10^5
550	0.70	$-(1.3 \pm 0.2) \times 10^5$
560	0.60 ±0.05	$-(1.06 \pm .05) \times 10^5$

Table 6.1: Nonlinear coefficients of the Ag-SiO_2 multilayer stack extracted from the Z-scan signals.

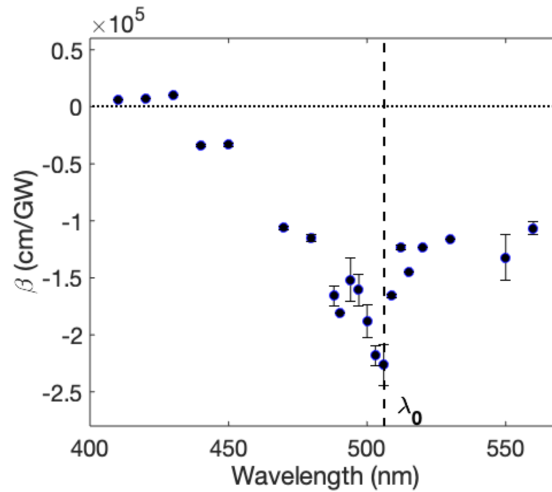

Figure 6.13: The nonlinear absorption coefficient β of the Ag-SiO_2 multilayer stack as a function of wavelength. Note the strong enhancement of β at the ENZ wavelength λ_0. The error bars indicate the deviations of the nonlinear absorption coefficient caused by the power fluctuations of the laser, evaluated as the standard error over 3 measurements. Where the error bars are not visible, they are smaller than the size of the markers.

Ag-SiO_2 multilayer stack. A peak is observed at 506 nm, thus indicating an enhancement of n_2 at the wavelength, just as our design predicted. From simulations, we found that the ENZ wavelength is located at 509 nm. This huge enhancement at the ENZ wavelength is approximately 7 times larger than the n_2 value away from the ENZ region (410 nm). The nonlinear absorption shows a more complex behaviour and even changes its sign. The transition from positive to negative nonlinear absorption occurs at 445 nm.

Thus, we have shown that an enhanced nonlinearity of the metal-dielectric multilayer stack arises from the specific dispersion of the plasmonic metamaterial that results in vanishingly small permittivity at some particular wavelength. Also, the wavelength at which permittivity crosses zero can be tuned as desired by engineering the metamaterial's geometrical structure with the same constituent materials, and therefore a strong nonlinear response can be achieved at the wavelength needed for any specific application. This result suggests that the nonlinear optical response is only a perturbation to the linear response. These metal-dielectric stacks can be used as a promising candidate for nonlinear applications, especially in the visible spectral range. This open new windows to nonlinear applications in nano-photonics, plasmonics, and nonlinear nano-optics in the visible spectrum.

Chapter 7

Conclusion and Future work

7.1 Conclusion

The ENZ materials possess exotic electromagnetic properties. But, those advantages have been restricted to the wavelengths where existing materials provided such an enhancement. We designed an optical metamaterial composed of alternating layers of metal and dielectric at nanometer- scale thickness such that its epsilon-near-zero wavelength lies in the visible spectrum. We have shown that the ENZ metamaterials realized using periodic metal-dielectric multilayer stacks have interesting properties in nonlinear optics, due to their potential to alter and access novel nonlinear propagation regimes. We observed a giant nonlinear phase shift in the multilayer stack at their ENZ regime which is not achievable in the constituent materials alone. This ENZ condition can be tuned over the entire visible spectrum by varying the layer thickness of the device.

The sample was fabricated onto a standard glass substrate by e-beam evaporation. The third-order nonlinearity of the Ag-SiO_2 multilayer stack was studied at different angles of incidence and different wavelengths using a picosecond Z-scan technique. A 28-picosecond pulsed laser with a repetition rate of 50 Hz pumps an optical parametric amplifier to produce light pulses spanning the wavelength range 410 nm to 560 nm. In the samples different nonlinear effects such as saturable absorption, two photon absorption and self-focusing were observed. Nonlinear refraction and absorption coefficients were measured using closed-aperture and open-aperture Z-scan methods, respectively. The nonlinear absorption coefficient β and the nonlinear refractive index n_2 of the Ag-SiO_2 multilayer stack extracted from the Z-scan fitting at the ENZ wavelength are $2.6 \pm 0.5 \times 10^5$ cm/GW and 2.3 ± 0.5 cm^2/GW, respectively. This is 10^7 times larger than the nonlinear refractive index of fused silica (3.2×10^{-7} cm^2/GW) and 20 times higher than the bulk silver. The ability to obtain strong nonlinearities at designated optical frequencies makes these metamaterials a flexible platform for the nonlinear applications in the visible spectral range. Also, the results of this work confirm that the enhancement of nonlinear optical properties at the ENZ regime can be generalized to a broader class of materials.

7.2 Scope for future work

Some major exciting results we observed during the completion of this thesis were left for future consideration. In this thesis, we presented the nonlinear optical properties of metal-dielectric stacks in their ENZ regime. We reported third order nonlinearity ($\chi^{(3)}$) we observed using a Z-

scan experimental setup. We extracted the nonlinear refractive index n_2 and nonlinear absorption coefficient β by fitting the open-aperture and closed-aperture Z-scan signals to the theoretical Z-scan equations (6.1) and (6.3). However, here we report measurements of higher-order nonlinearity by cranking up the intensity of the laser beam at the focus. At higher intensities, the $\chi^{(3)}$ effect get dominated by higher order nonlinearities like $\chi^{(5)}$, $\chi^{(7)}$ etc. This has been reported in chalcogenide glasses also. This suggests that materials appropriate to applications requiring higher-order nonlinearities in visible spectral range can also be realized using similar samples and methods.This seems to be really exciting for the future work. Figure 7.1 shows some traces of higher order nonlinearities at 440 nm at higher intensities.

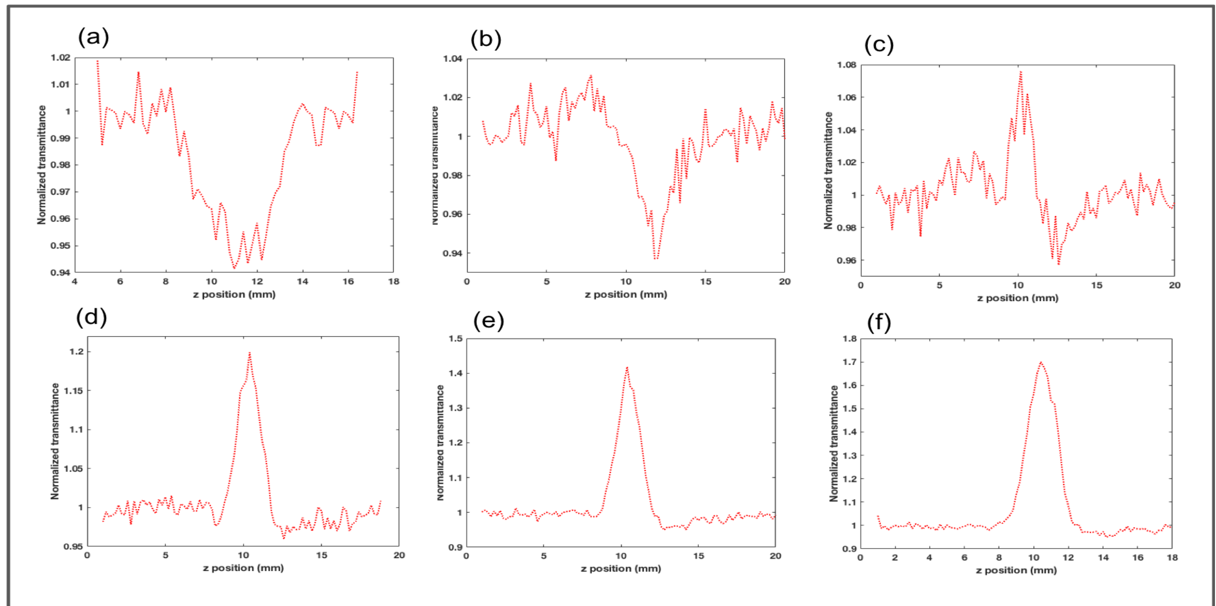

Figure 7.1: Normalized transmittance of the Ag-SiO_2 measured at 450 nm at intensities (a) 150 MW/cm^2 (b) 235 MW/cm^2 (c) 300 MW/cm^2 (d) 350 MW/cm^2 (e) 500 MW/cm^2 (f) 550 MW/cm^2. The change in sign of the nonlinear absorption coefficient as a function of intensity indicates the presence of higher-order nonlinear responses.

We have seen that how the nonlinear optical properties of metal-dielectric multilayer stack is enhanced at their ENZ regime. The applications for the ENZ nonlinear media, especially in the visible spectral range, are exciting and offer great potential to impact various fields of nonlinear optics and plasmonics. Based on the exciting research activity of this field, it is anticipated that research on the nonlinear properties in the ENZ materials will keep producing amazing results in the coming years.

Chapter 8

Appendix

8.1 Direct inversion method

Another approach we tried to extract the n and k of metal-dielectric multilayer stack is the direct inversion method. This is a semi-analytical method for n-k inversion of ellipsometry data ψ and Δ. The measured parameters from ellipsometer ψ and Δ are called ellipsometric angles. In this method, we performed an inversion of the ellipsometric spectra for the determination of optical constants without requiring particular assumptions about the shape of a model dielectric function like in the traditional method of data fitting. They are related to the ratio of the complex Fresnel reflection coefficients r_s and r_p. This is expressed by the fundamental equation of ellipsometry as,

$$\frac{r_p}{r_s} = \tan \Psi e^{(i\Delta)} \tag{8.1}$$

From Fresnel reflection coefficients we can calculate the effective refractive index of the sample. Fig 8.1 shows the method of extracting the refractive index from ellipsometric angles ψ and Δ. This method works by refashioning the ellipsometric equations under a parametric polynomial form and finding the polynomial solutions of the obtained parametric curves. The intersections of the curves define solutions of the ellipsometry problem. The black cross marks in Fig (8.1) represents the solution of the method which in fact depends mostly on the initial guess. Meanwhile, a good initial guess can essentially reduce the computational eort and leads to a solution. The extracted values were not in agreement with the effective medium theory and hence were ruled out. This method needs a lot of computation time for anisotropic inhomogeneous multilayer samples. For simpler samples like ZnO, this method was able to extract all the solutions in a given range of n and k values without requiring guess values; overcoming the ambiguous determination by standard least-squares methods [79].

8.2 Automation of the setup

Collecting the data from Z-scan manually is a very tedious and time consuming process. The movement of translation stage is typically about step size of 50 to100 micron which takes not less than 200 steps for each measurement. Also at each steps, we should acquire data from three detectors (reference detector, open-aperture detector and closed-aperture detector). All these step has to repeated for every wavelength range of choice and also for different power, which is achieved by rotating the half-wave plate. Considering all these facts, automating the

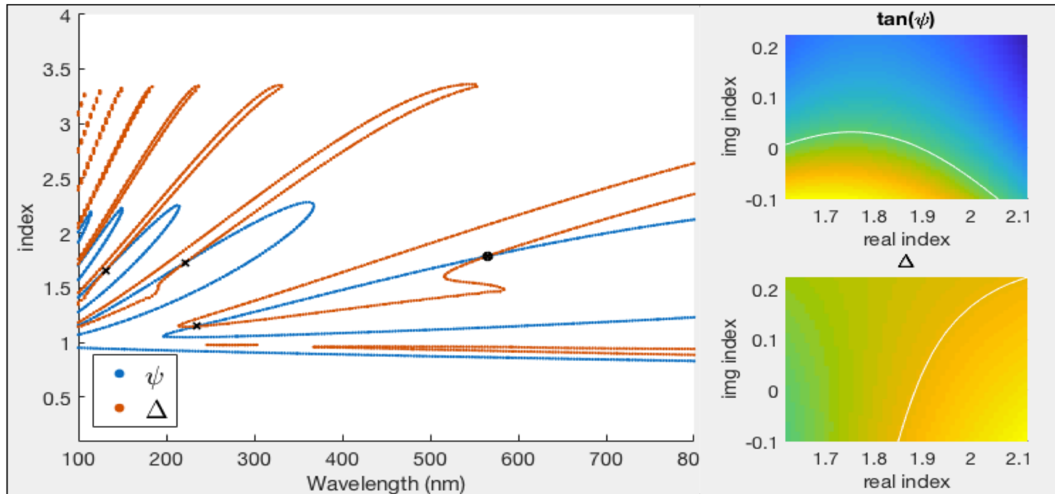

Figure 8.1: Direct inversion method to extract the refractive index from ellipsometric angles ψ and Δ. The first figure shows the solution curves and the second figure represents the n and k extracted.

setup seems to be very essential. Automation of the experiment setup is done using the software Labview. Labview can synchronize and control the processes such as movement of translational stage, rotation of half-wave plate for power control, rotation of the sample (if required) etc. It is inclusive of tools for acquiring, analyzing, displaying and saving data. It not only save the time, but also can eliminate the human errors for such a large set of measurements.
To take in account of the power fluctuations from laser, we adopted another method while collecting data. Using labview, power is collected 50 times for every single step. It is programmed in such a way that a 'for loop' with 50 iterations is created and the average of that 50 measurements is calculated for every step. Even though it is bit time consuming than the normal way, this will help to improve the shape and quality of the Z-scan signal.
The block diagram of labview code made for automating the whole experiment is shown in Fig (8.2).

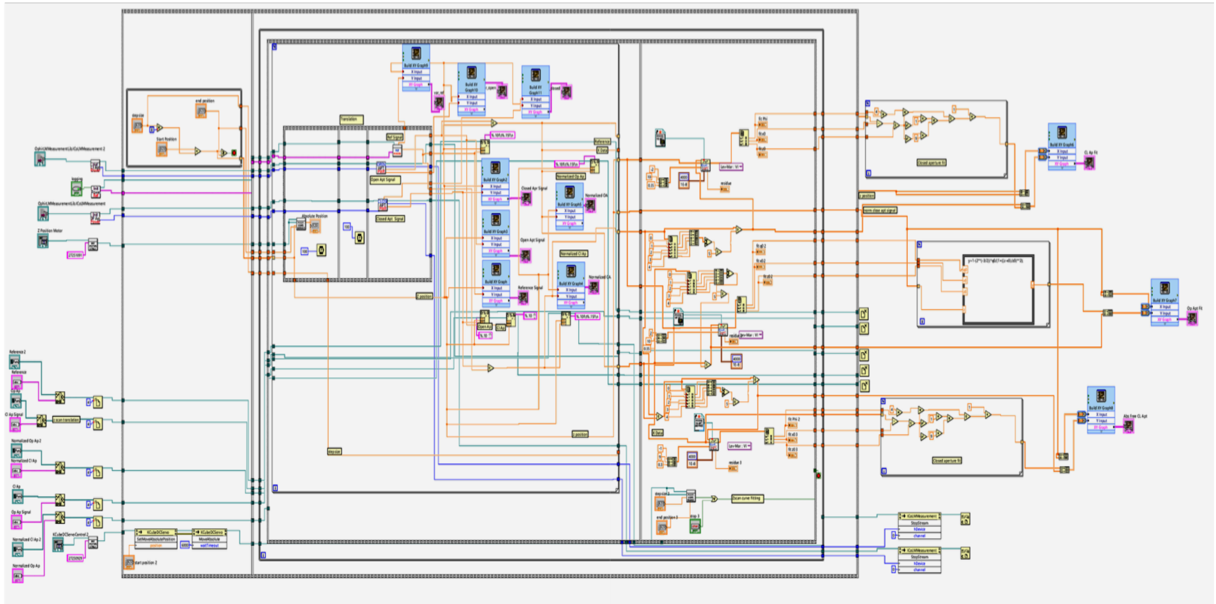

Figure 8.2: Block diagram of the labview code

8.3 Matlab code for permittivity calculation

In this section, we present a retrieval Matlab code we used to extract the effective parameters of layered metal-dielectric stack structures. The first step in this procedure is to obtain the scattering parameters (S-parameters) for a finite-thickness, planar slab of the inhomogeneous structure to be characterized. This is done using Lumerical simulation. We used a function called "stackrt" which gives us the scattering parameters of the multilayer stack using the transfer matrix method. By inverting the analytical expressions for the S-parameters, one can solve for the refractive index and the impedance. this data can be straightforwardly used to calculate the effective permittivity of the stack for both polarizations. The scattering parameters are used as the initial data for the retrieval matlab code for the retrieval process.

Matlab Code

```
1 function retrieval
2 close all
3
4 % This Matlab code calculates the effective refractive index and
     impedance. We use Eq. (9) from:
5 % D. R. Smith et al., "Electromagnetic parameter retrieval from
     inhomogeneous metamaterials", Phys Rev E 71, 036617 (2005)
6 % More details here: https://kb.lumerical.com/en/
     metamaterials_bulk_effective_properties.html
7
```

```
8  % Here we load the data we obtained from the Lumerical simulation
     using the principle of Transfer Matrix Method
9  f = load('SiO2_Ag_65_16_sample);
10
11 total_thickness = f.total_thickness;
12 bilayer_thickness = f.bilayer_thickness;
13 w = f.w;
14 k = f.k;
15
16 E_field = f.field.Es;
17 E_field = E_field(:,2,:); % Considering normal incidence Ex and Ez
     are all zero
18 z = f.field.z;
19
20 % scattering parameters
21 S11 = f.S11;
22 S12 = f.S12;
23 S21 = f.S21;
24 S22 = f.S22;
25
26 % Transfer Matrix parameters:
27 T11 = (1./(2*S21)) .* ((1+S11) .* (1-S22) + S21.*S12);
28 T22 = (1./(2*S21)) .* ((1-S11) .* (1+S22) + S21.*S12);
29 T12 = (1./(2*S21)) .* ((1+S11) .* (1+S22) - S21.*S12);
30 T21 = (1./(2*S21)) .* ((1-S11) .* (1-S22) - S21.*S12);
31
32 % Impedances from Transfer Matrixes:
33 Z_eff_1 = ((T22 - T11) + sqrt((T22-T11).^2 + 4*T12.*T21))./(2*T21);
34 Z_eff_2 = ((T22 - T11) - sqrt((T22-T11).^2 + 4*T12.*T21))./(2*T21);
35
36 % First step is to use the phases from the actual field to help
     decide which branch to pick
37
38 % Finding the edges of the bilayers
39 num_bilayers = round(max(z)/bilayer_thickness);
40
41 bilayer_edges = zeros(1, num_bilayers);
42 for i = 0:num_bilayers
43     bilayer_edges(i+1) = findsmallest(z-bilayer_thickness*i);
44 end
45
46 % Keep the data at the longest wavelength only:
47 E_field = squeeze(E_field(:, :, end));
48
49 % The E field at the edges of the bilayers:
50 E_field_edges = E_field(bilayer_edges);
51
52 % The change in magnitude of E at these locations(imag n)
```

```
53 p = polyfit([1:num_bilayers-1]'*bilayer_thickness, log(abs(
       E_field_edges(2:end-1))),1) * w(end) / (2*pi);
54 n_imag_guess = -p(1);
55
56 % The change in the average amount the phase (real n)
57 p = polyfit([1:num_bilayers-1]'*bilayer_thickness, angle(
       E_field_edges(2:end-1)),1) * w(end) / (2*pi);
58 n_real_guess = p(1);
59
60 n_guess = n_real_guess + 1i*n_imag_guess
61
62 % Finally, plug in the scattering elements into Eq. (9) from our
       reference:
63 cosnkd = (1-S11.*S22 + S21.^2)./(2*S21);
64
65 % initial guess:
66 n_eff = acos(cosnkd) ./ (k*total_thickness);
67
68 % advanced guess:
69 n_eff(length(w)) = n_guess;
70 phases = -10*pi:2*pi:10*pi;
71
72 for i = length(w)-1:-1:1
73     temp = acos(cosnkd(i));
74     temp = [temp+phases -temp+phases] ./ (k(i)*total_thickness);
75
76     % We want the solution we choose to be closest to the most recent
77     % point:
78     differences = (real(temp) - real(n_eff(i+1))) .* (imag(temp) -
           imag(n_eff(i+1)));
79
80     % We also want the solution to have a similar slope to what we
           already
81     % have (to get "smooth" curves). (Only works after the second
           point.)
82     if i<length(w)-1
83         slopes = abs(real(temp) - real(n_eff(i+1))) - abs(real(n_eff(
               i+1)) - real(n_eff(i+2)));
84     else
85         slopes = 1;
86     end
87
88     thisone = findsmallest(differences.*slopes);
89         % find which solution is closest to the previous one:
90
91     n_eff(i) = temp(thisone);
92 end
93
94 % Once the loop is over, replace our "guess point":
```

```
95        temp = acos(cosnkd(end));
96        temp = [temp+phases -temp+phases] ./ (k(end)*total_thickness);
97        temp = [temp -temp]; %#ok<AGROW>
98
99        differences = (real(temp) - real(n_eff(end-1))) .* (imag(temp) -
              imag(n_eff(end-1)));
100       slopes = abs(real(temp) - real(n_eff(end-1)) - abs(real(n_eff(
              end-1)) - real(n_eff(end-2)));
101
102       n_eff(end) = temp(findsmallest(differences.*slopes));
103   plot(w*1e9, real(n_eff.^2));
104   hold on
105   plot(w*1e9, imag(n_eff.^2));
106   plot(w*1e9, zeros(size(w)), '--k');
107   % Returns the index where the smallest value appears. Good for
          optimizing!
108   function out = findsmallest(a)
109   out = find(min(abs(a)) == abs(a));
110   if length(out)>1
111       out = out(1);
112   end
113   end
```

Bibliography

[1] Tokizaki, T. *et al.* Subpicosecond time response of third-order optical nonlinearity of small copper particles in glass. *Applied Physics Letters* **65**, 941–943 (1994).

[2] Smith, D. D., Fischer, G., Boyd, R. W. & Gregory, D. A. Cancellation of photoinduced absorption in metal nanoparticle composites through a counterintuitive consequence of local field effects. *Journal of the Optical Society of America B* **14**, 1625 (1997).

[3] Neeves, A. E. & Birnboim, M. H. Composite structures for the enhancement of nonlinear optical materials. *Optics Letters* **13**, 1087 (1988).

[4] Haglund, R. F. *et al.* Picosecond nonlinear optical response of a Cu:silica nanocluster composite. *Optics Letters* **18**, 373 (1993).

[5] Bennink, R. S., Yoon, Y.-K., Boyd, R. W. & Sipe, J. E. Accessing the optical nonlinearity of metals with metal- dielectric photonic bandgap structures. *Optics Letters* **24**, 1416 (1999).

[6] Scalora, M. *et al.* Transparent, metallo-dielectric, one-dimensional, photonic band-gap structures **2377** (2013).

[7] Lepeshkin, N. N., Schweinsberg, A., Piredda, G., Bennink, R. S. & Boyd, R. W. Enhanced nonlinear optical response of one-dimensional metal-dielectric photonic crystals. *Physical Review Letters* **93**, 1–4 (2004).

[8] Ziolkowski, R. W. Propagation in and scattering from a matched metamaterial having a zero index of refraction. *Physical Review E - Statistical Physics, Plasmas, Fluids, and Related Interdisciplinary Topics* **70**, 12 (2004).

[9] Alam, M. Z., Leon, I. D. & Boyd, R. W. Large optical nonlinearity of indium tin oxide in its epsilon-near-zero region **352**, 0–3 (2016).

[10] Caspani, L. *et al.* Enhanced nonlinear refractive index in epsilon-near-zero materials. *Physical review letters* **116**, 233901 (2016).

[11] Boyd R.W. *Nonlinear Optics*, Elsevier (2003).

[12] Spitzer, W. G., Kleinman, D. & Walsh, D. Infrared properties of hexagonal silicon carbide. *Physical Review* **113**, 127–132 (1959).

[13] Zhong, S., Liu, T., Huang, J. & Ma, Y. Giant power enhancement for quasi-omnidirectional light radiation via ϵ-near-zero materials. *Optics Express* **26**, 2231 (2018).

[14] Caspani, L. *et al.* Enhanced nonlinear refractive index in epsilon-near-zero materials. *Physical review letters* **116(23)**, 233901 (2016).

[15] Adams, D. C. *et al.* Funneling Light through a Subwavelength Aperture with Epsilon-Near-Zero Materials **133901**, 1–5 (2011).

[16] Shea, J. Electromagnetic mixing formulas and applications [Book Review]. *IEEE Electrical Insulation Magazine* **16**, 36–37 (2005).

[17] Pendry, J., Holden, A. J., Stewart, W. J. & Youngs, I. Extremely Low Frequency Plasmons. *Physical Review Letters* **76**, 4773–6 (1996).

[18] Silveirinha, M. & Engheta, N. Tunneling of electromagnetic energy through subwavelength channels and bends using ϵ-near-zero materials. *Physical Review Letters* **97** (2006).

[19] Alù, A., Silveirinha, M. G., Salandrino, A. & Engheta, N. Epsilon-near-zero metamaterials and electromagnetic sources : Tailoring the radiation phase pattern 1–13 (2007).

[20] Ziolkowski, R. W. Propagation in and scattering from a matched metamaterial having a zero index of refraction. *Physical Review E - Statistical Physics, Plasmas, Fluids, and Related Interdisciplinary Topics* **70**, 12 (2004).

[21] Silveirinha, M. & Engheta, N. Design of matched zero-index metamaterials using nonmagnetic inclusions in epsilon-near-zero media. *Physical Review B - Condensed Matter and Materials Physics* **75**, 1–10 (2007).

[22] Alù, A. & Engheta, N. Achieving transparency with plasmonic and metamaterial coatings. *Physical Review E - Statistical, Nonlinear, and Soft Matter Physics* **72**, 1–9 (2005).

[23] Silveirinha, M. G., Alù, A. & Engheta, N. Parallel-plate metamaterials for cloaking structures. *Physical Review E - Statistical, Nonlinear, and Soft Matter Physics* **75**, 1–16 (2007).

[24] Reshef, O., De Leon, I., Alam, M. Z. & Boyd, R. W. Nonlinear optical effects in epsilon-near-zero media. *Nature Reviews Materials* (2019).

[25] Argyropoulos, C., Chen, P. Y., D'Aguanno, G., Engheta, N. & Alù, A. Boosting optical nonlinearities in epsilon-near-zero plasmonic channels. *Physical Review B - Condensed Matter and Materials Physics* (2012).

[26] Neira, A. D. *et al.* with plasmonic metamaterials. *Nature Communications* **6**, 1–8 (2015).

[27] Vesseur, E. J. R., Coenen, T., Caglayan, H., Engheta, N. & Polman, A. Experimental Verification of n=0 Structures for Visible Light. *Physical Review Letters* **110**, 013902 (2013).

[28] Pollard, R. J. *et al.* Optical nonlocalities and additional waves in epsilon-near-zero metamaterials. *Physical Review Letters* **102**, 1–4 (2009).

[29] Alekseyev, L. V. *et al.* Uniaxial epsilon-near-zero metamaterial for angular filtering and polarization control. *Applied Physics Letters* **97**, 1–4 (2010).

[30] Luk, T. S. & Laboratories, S. N. Optical properties of metal-dielectric based epsilon near zero metamaterials 1–6 (2016).

[31] Roberts, M. J. Effective permittivity near zero in nanolaminates of silver and amorphous polycarbonate. *Journal of Nanophotonics* **4**, 043511 (2010).

[32] Roberts, M. J. Effective permittivity near zero in nanolaminates of silver and amorphous polycarbonate. *Journal of Nanophotonics* **4**, 043511 (2010).

[33] Gao, J. *et al.* Experimental realization of epsilon-near-zero metamaterial slabs with metal-dielectric multilayers. *Applied Physics Letters* (2013). 1307.1880.

[34] Maas, R., Parsons, J., Engheta, N. & Polman, A. Experimental realization of an epsilon-nearzero metamaterial at visible wavelengths. *Nature Photonics* **7**, 907–912 (2013).

[35] Ferrari, L., Wu, C. & Lepage, D. Hyperbolic metamaterials and their applications. *Progress in Quantum Electronics* **40**, 1–40 (2015).

[36] Boyd, R. W. & Sipe, J. E. Nonlinear susceptibility of composite optical materials in the Maxwell Garnett model. *Physical Review A* **46**, 1614–1629 (1992).

[37] Papadakis, G. T., Yeh, P. & Atwater, H. A. Retrieval of material parameters for uniaxial metamaterials. *Physical Review B - Condensed Matter and Materials Physics* **91**, 1–12 (2015). 1411.6312.

[38] Forouhi, A. R. & Bloomer, I. Optical properties of crystalline semiconductors and dielectrics. *Physical Review B* **38**, 1865–1874 (1988).

[39] Wenshan, C. & Shalaev, V. *Optical Metamaterials* (2010).

[40] Dyson, F. J. Electron Spin Resonance Absorption in Metals. II. Theory of Electron Diffusion and the Skin Effect.pdf. *Physical Review* **98(2)**, 349 (1955).

[41] Kaipurath, R. M. *et al.* Optically induced metal-to-dielectric transition in Epsilon-Near-Zero metamaterials. *Scientific Reports* **6**, 1–7 (2016).

[42] West, P. R. *et al.* Searching for better plasmonic materials. *Laser and Photonics Reviews* **4**, 795–808 (2010).

[43] J.C Maxwell Garnett. Index slip. *Phil. Trans. R. Soc. Lond, A* **203**, 385–420 (1904).

[44] Bruggeman, D. a. G. Calculation of various physics constants in heterogenous substances I Dielectricity constants and conductivity of mixed bodies from isotropic substances. *Annals of Physics* **416**, 636–664 (1935).

[45] Bergman, D. J. The dielectric constant of a composite material-A problem in classical physics. *Physics Reports* **43**, 377–407 (1978).

[46] Ignaovich, Filip V., V. K. I. Optics of anisotropic media. *Physics-Uspekhi* **55.7**, 709 (2012).

[47] S.M.Rytov. Electromagnetic Properties of a Finely Stratified Medium. *Soviet Physics JEPT* **2**, 466–475 (1956).

[48] Wood, B., Pendry, J. B. & Tsai, D. P. Directed subwavelength imaging using a layered metal-dielectric system. *Physical Review B - Condensed Matter and Materials Physics* **74**, 1–8 (2006).

[49] Menzel, C., Rockstuhl, C., Paul, T., Lederer, F. & Pertsch, T. Retrieving effective parameters for metamaterials at oblique incidence. *Physical Review B - Condensed Matter and Materials Physics* **77**, 1–8 (2008).

[50] P.B. Johnson & R.W.Christy. PhysRevB.6.4370. *Physical Review B* **6**, 1–10 (1972).

[51] Palik, E. D. Handbook of optical constants of solids. *Academic press* **3**, 11–34 (1998).

[52] Poddubny, A., Iorsh, I., Belov, P. & Kivshar, Y. Hyperbolic metamaterials. *Nature Photonics* **7**, 958–967 (2013).

[53] Tumkur, T., Barnakov, Y., Kee, S. T., Noginov, M. A. & Liberman, V. Permittivity evaluation of multilayered hyperbolic metamaterials: Ellipsometry vs. Reflectometry. *Journal of Applied Physics* (2015).

[54] K.M.Ho, C.T.Chan & C.M.Soukoulis. Letters 17 **65**, 3152–3155 (1990).

[55] Systems, L. Directed Sub-Wavelength Imaging Using a Layered Metal-Dielectric System **1**, 1–14 (2008). `0608170v1`.

[56] Yariv, A. & Yeh, P. Yariv, A. - Optical electronics.pdf.

[57] Smith, D. R., Vier, D. C., Koschny, T. & Soukoulis, C. M. Electromagnetic parameter retrieval from inhomogeneous metamaterials. *Physical Review E - Statistical, Nonlinear, and Soft Matter Physics* (2005).

[58] Palik, E. D. *Handbook of optical constants of solids* (1998).

[59] Boyd, R. W. & Sipe, J. E. Nonlinear optical susceptibilities of layered composite materials. *Journal of the Optical Society of America B* **11**, 297 (1994).

[60] Yeh, P., Yariv, A., Cho, A. Y., Yeh, P. & Yariv, A. Optical surface waves in periodic layered media Optical surface waves in periodic layered media a). *New York: Wiley.* **95**, 2012–2014 (1978).

[61] Vassant, S., Hugonin, J.-P. & Greffet, J.-J. Quasi-confined ENZ mode in an anisotropic uniaxial thin slab. *Optics Express* **27**, 12317 (2019).

[62] HORIBA Jobin Yvon - 2008 - Spectroscopic Ellipsometry User Guide. Tech. Rep.

[63] Smith, D., Schultz, S., Markoš, P. & Soukoulis, C. Determination of Negative Permittivity and Permeability of Metamaterials from Reflection and Transmission Coefficients. *Physical Review B* 1–5 (2002).

[64] Sheik-Bahae, M., Said, A. A. A., Wei, T. H., Hagan, D. J. & Van Stryland, E. W. Sensitive measurement of optical nonlinearities using a single beam. *IEEE Journal of Quantum Electronics* **26**, 760–769 (1990).

[65] Neethling, Pieter., . *Determining non-linear optical properties using the Z-scan technique by Pieter Neethling Master of Science.* Ph.D. thesis (2005).

[66] Said, A. A. & Stryland, E. W. V. High-sensitivity, single-beam n 2 measurements **14**, 955–957 (1989).

[67] Owens, D. Linear and nonlinear optical properties of metal-dielectric multilayer structures (2010).

[68] Woollam, J. A. *et al.* Overview of Variable Angle Spectroscopic Ellipsometry (VASE), Part I: Basic Theory and Typical Applications. *International Society for Optics and Photonics.* **10294**, 1029402 (1999).

[69] Collett, E. Field Guide to Polarization. *SPIE Press* (2005).

[70] Mian, S. M., Taheri, B. & Wicksted, J. P. Effects of beam ellipticity on Z-scan measurements **13**, 856–863 (1996).

[71] Holmen, L. G. & Haakestad, M. W. Optical limiting properties of carbon disulfide at 2.05μm wavelength **33**, 97310J (2016).

[72] Ganeev, R. A., Ryasnyanski, A. I. & Kuroda, H. Nonlinear Optical Characteristics of Carbon Disulfide **100**, 108–118 (2006).

[73] Reichert, M. *et al.* Temporal, spectral, and polarization dependence of the nonlinear optical response of carbon disulfide. *Optica* **1**, 436 (2014).

[74] Reichert, M. *et al.* Temporal, spectral, and polarization dependence of the nonlinear optical response of carbon disulfide: supplementary material. *Optica* **1**, 436 (2014).

[75] Liu, X., Guo, S., Wang, H. & Hou, L. Theoretical study on the closed-aperture Z -scan curves in the materials with nonlinear refraction and strong nonlinear absorption. *Optics Communications* **197**, 431–437 (2001).

[76] Qu, S., Zhang, Y., Li, H., Qiu, J. & Zhu, C. Nanosecond nonlinear absorption in Au and Ag nanoparticles precipitated glasses induced by a femtosecond laser. *Optical Materials* **28**, 259–265 (2006).

[77] Fan, G. H., Qu, S. L., Guo, Z. Y., Wang, Q. & Li, Z. G. Size-dependent nonlinear absorption and refraction of Ag nanoparticles excited by femtosecond lasers. *Chinese Physics B* **21** (2012).

[78] Hache, F., Ricard, D., Flytzanis, C. & Kreibig, U. The Optical Kerr Effect in Small Metal Particles and Metal Colloids: the Case of Gold. *Applied Physics A: Materials Science & Processing* **47**, 347–357 (1988).

[79] Gilliot, M. Semi-analytical method for n–k inversion of ellipsometry data. *Applied Optics* **58**, 800 (2019).